DISSERTATION

PROGRESS IN COHERENT LITHOGRAPHY USING TABLE-TOP EXTREME

ULTRAVIOLET LASERS

Submitted by

Wei Li

Department of Electrical and Computer Engineering

In partial fulfillment of the requirements

For the Degree of Doctor of Philosophy

Colorado State University

Fort Collins, Colorado

Spring 2016

Doctoral Committee:

    Advisor: Mario C. Marconi
    Co-Advisor: Carmen S. Menoni

    Mingzhong Wu
    Diego Krapf

ABSTRACT

PROGRESS IN COHERENT LITHOGRAPHY USING TABLE-TOP EXTREME

ULTRAVIOLET LASERS

Nanotechnology has drawn a wide variety of attention as interesting phenomena occurs when the dimension of the structures is in the nanometer scale. The particular characteristics of nanoscale structures had enabled new applications in different fields in science and technology. Our capability to fabricate these nanostructures routinely for sure will impact the advancement of nanoscience. Apart from the high volume manufacturing in semiconductor industry, a small-scale but reliable nanofabrication tool can dramatically help the research in the field of nanotechnology. This dissertation describes alternative extreme ultraviolet (EUV) lithography techniques which combine table-top EUV laser and various cost-effective imaging strategies. For each technique, numerical simulations, system design, experiment result and its analysis will be presented.

In chapter II, a brief review of the main characteristics of table-top EUV lasers will be addressed concentrating on its high power and large coherence radius that enable the lithography application described herein.

The development of a Talbot EUV lithography system which is capable of printing 50nm half pitch nanopatterns will be illustrated in chapter III. A detailed discussion of its resolution limit will be presented followed by the development of X-Y-Z positioning stage, the fabrication protocol for diffractive EUV mask, and the pattern transfer using self- developed ion beam etching, and the dose control unit. In addition, this dissertation demonstrated the capability to

fabricate functional periodic nanostructures using Talbot EUV lithography. After that, resolution enhancement techniques like multiple exposure, displacement Talbot EUV lithography, fractional Talbot EUV lithography, and Talbot lithography using 18.9nm amplified spontaneous emission laser will be demonstrated.

Chapter IV will describe a hybrid EUV lithography which combines the Talbot imaging and interference lithography rendering a high resolution interference pattern whose lattice is modified by a custom designed Talbot mask. In other words, this method enables filling the arbitrary Talbot cell with ultra-fine interference nanofeatures. Detailed optics modeling, system design and experiment results using He-Ne laser and table top EUV laser are included. The last part of chapter IV will analyze its exclusive advantages over traditional Talbot or interference lithography.

ACKNOWLEDGEMENTS

TABLE OF CONTENTS

CHAPTER 1 INTRODUCTION

1.1 NANOTECHNOLOGY OVERVIEW AND ITS APPLICATION

Nanotechnology has drawn a wide range of attention due to the fact that unique properties of nanoscale structures and devices had demonstrated new important applications in science and technology. A new kind of structures like meta-materials, photonic crystals, plasmonics and nano-magnetic structures has been derived from the development of nanotechnology. The fundamental study of phenomena that occur in nanostructures with dimension smaller than 100nm has stimulated a new research field named as "nanoscience".

One of the most successful applications for nanoscience is negative index meta-material [1][2] which offers an entire new route for people to design and utilize creative properties of "artificial" material at will. Researchers are able to engineer the nanostructures so that the permittivity and permeability are both negative rendering a negative index metamaterial. It opens up prospects for studies of reversed Doppler effect, superlenses and optical tunneling[3].

Photonic crystals (PCs) also evolved from the development of nanotechnology. The lattice of PCs is designed and fabricated in a way that a desired optical property is able to be achieved. Components like waveguide, optical cavity [4][5] and optical switch [6] based on PCs have been demonstrated.

In addition, by taking advantages of nanofabrication techniques, solar cells in combination with plasmonics were also designed and fabricated to address the challenges in efficiency and physical thickness [7][8]. Plasmonic light-trapping geometries designed for photovoltaic thin film have been developed to optimize the harvesting of sunlight energy by increasing the effective optical path length.

Nanotechnology has also enabled cost-effective patterned media for hard drive recording industry. Dense nanomagnetics have been patterned in desired lattice using a wide variety of fabrication methods like nanoimprint or directed self-assembly.

Beyond that, by merging photonics and electronics, plasmonic circuit offers an integral solution to the size-compatibility problem [9]. With plasmonic integrated on a chip, the communication capability between components can be dramatically increased comparing with traditional logics circuits.

There are, of course, several other applications where nanoscience helps to break through traditional limits. This introduction provides few examples and is just the "tip of the iceberg". Nanotechnology enabled the realization of devices that are currently used in the fields like biology, cancer therapy, etc.. This is a rich and active research field with important economic and social impact.

1.2 ALTERNATIVE NANOFABRICATION TECHNIQUES

The advancement of nanotechnology depends on the capability to fabricate these nanostructures in a simple and robust manner. Scientist and engineers in semiconductor industry have been dedicating efforts in developing nanopatterning techniques to increase the fabrication resolution and simultaneously lower the cost. Suppliers for semiconductor industry around the world like ASML, Nikon and Lam have ensured the pursuit of Moore's law that predicted the roadmap of nanofabrication by having developed extremely complex and expensive patterning tools. However, these state-of art manufacturing tools are too expensive for a small business or research institute. Other than the high volume manufacturing(HVM) in semiconductor industry that had produced remarkable progress in micro-electronic devices in the last decades, a cost-

effective and small-scale nanofabrication tool with high resolution can positively influence the advancement of the research in the field of nanotechnology. In the following sections, a brief review of the most valuable nanopatterning approaches compatible with small scale nanofabrication has been demonstrated

1.2.1 E-BEAM LITHOGRAPHY

Electron beam lithography is an important nanofabrication technique. Energetic electron beams with small current (10-100keV and pA~nA) are precisely focused onto resist-coated wafer to define the nanopatterns. The part on the positive resist that has been exposed by these energetic electrons will be cleaned out by a development process while the unexposed part on the positive resist will remain on top of wafer firmly. A number of precise electron optics ensures the ebeam is formed into a desired shape (typically around 6nm spot in diameter) which scans an arbitrary pattern on top of the resist coated wafer. Large area fields can be patterned using a state of art interference stitching stage that has a sub 1nm positioning resolution. In this manner, EBL delivers a full field nanofabrication technique which is capable of creating nanostructures with high resolution. As one of the most important fabrication techniques, electron beam lithography (EBL) still holds the record of world's smallest nanofeatures (sub 10nm) ever made[10][11]. However, depending on the pattern design and the substrate underneath the resist, it usually takes a much longer time to define a given nanostructure over a certain surface than optical lithography. Additionally, this tool requires periodic services to maintain the beam quality, increasing the cost of maintenance.

1.2.2 NANOIMPRINT LITHOGRAPHY

Nanoimprint lithography (NIL) is a non-traditional fabrication technique. It defines the nanopattern through direct mechanical deformation of the resist material and circumvent the

diffraction limits set by photo or electron beam lithography [12]. The process relies on a straightforward principle that is depicted in Figure 1.1. A rigid mask is embedded into a polymer with low viscosity under optimized temperature and pressure. The polymer is shaped into the topology of mask and it is cross-linked by a uniform heat or UV exposure creating a stable surface nanofeature. The mask is then released from the cured resist leaving the duplicated nanopatterns on the substrate which are then transferred by reactive ion etch (RIE) to eliminate the residual resist. NIL is a high resolution and cost effective replication technique that has demonstrated a record of 5nm isolated features and 14nm pitch over large areas [13].
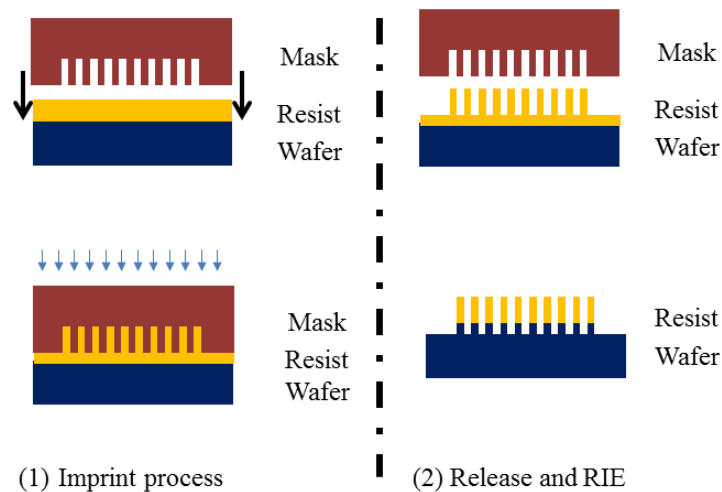
Figure 1.1: Nanoimprint process

With simple setup and high resolution patterning capability, NIL has been used to fabricate solar cells[14], dense magnetic patterns[15] and organic light emitting devices[16].This technique has also been adopted by Canon Inc. to develop a commercial lithography tool with sub 20nm resolution. However, because it is contact lithography, NIL suffers from mask contamination and its yield can be quite unstable. Unlike state of art optical lithography, NIL is a 1:1 printing technique meaning that the size of the feature on mask cannot be further reduced. Thus generating a 3D mask with high resolution is challenging and expensive. It increases the

maintenance cost for NIL process. When the mask is released from the polymer, it can be ruined by resist residual (chemical that remains attached on mask), turning the whole reticle useless[17]. These defect issues (shown in Figure 1.2) need more study and understanding and it has been improved by introducing a release layer and a step flash process[18]. However, the most urgent issue for imprint lithography is from level to level alignment[19]. For instance, in the fabrication of memory chips, the levels of word line and electrical pads need to be aligned within sub 10nm. If NIL is to be used for this kind of product, during the thermal driven process, expansion and drift of alignment mark will affect the alignment accuracy. In conclusion, more examination on this subject is needed to make NIL a reliable tool compatible with production.
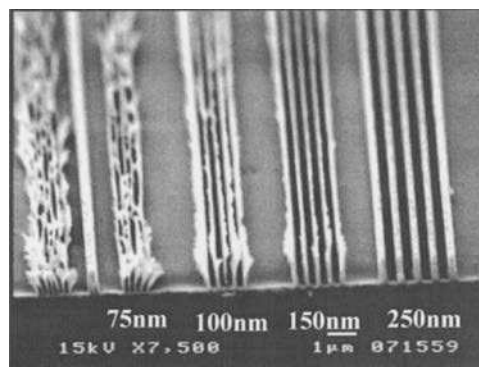
Figure 1.2: Defects of Nanoimprint[17]

1.2.3 DIRECTED SELF-ASSEMBLY

Directed self-assembly (DSA) of block copolymer (BCP) is an alternative fabrication method to generate periodic patterns with high resolution cost-effectively. The process of DSA is depicted in Figure 1.3[20]. In this straight forward process, BCP (PS-b-PMMA) is spin-coated and then annealed on a pre-patterned substrate which already has either a chemical contrast or a topographic contrast. During the bake process, PS and PMMA which have negative affinities got separated automatically by thermal dynamic driving force, creating nanopatterns under the guidance of the pre-patterned substrate. This separated BCP thin film is then etched by O_2 plasma

5

which clears the PMMA part preferentially. An unusual characteristic for this process is that the pattern is defined from bottom-up instead of a popular top-down configuration used in beam lithography or imprint lithography.
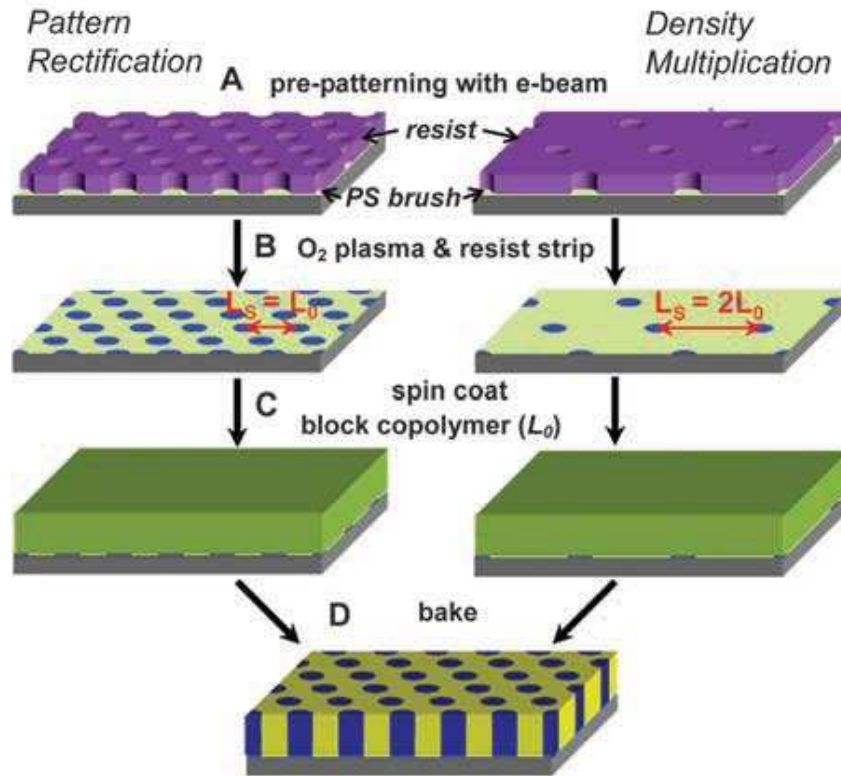
Figure 1.3[20]: Process of DSA using BCP

Using this simple process, DSA is able to generate periodic patterns as small as sub 10nm[21] with a control on the orientation of the self-assembled nanopattern by optimizing different annealing parameters[22][23]. In addition, this technique is not limited to fabricating hexagonal lattice but also can generate rectangular layouts as well[24]. Beyond that, DSA has the capability to rectify the guidance pattern or even duplicate the pitch resolution[20].

Although this research area has drawn a great deal of attention, the most urgent concerns are concentrated on line width roughness (LWR) and local critical dimension uniformity (LCDU) which is shown in Figure 1.4[25]. No matter how high the resolution can be, LWR of this

6

technique is never satisfied[26]. The concern of LCDU, which level to level alignment accuracy relies on, can also be an issue when this technique is integrated to the complete nanopatterning processes.
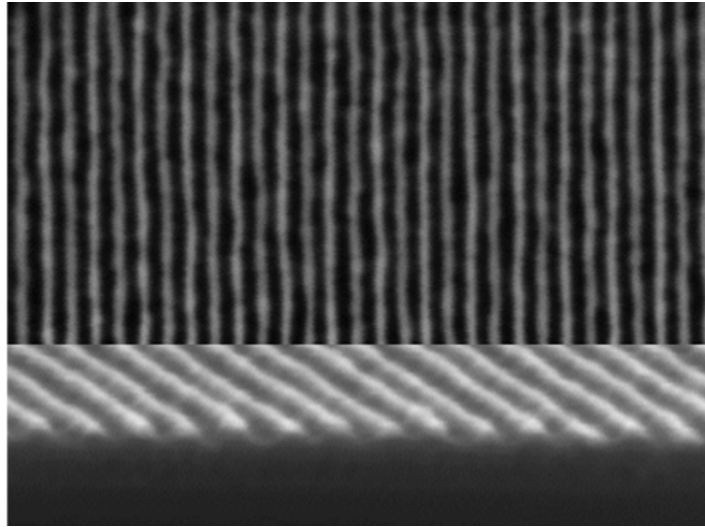
Figure 1.4: Amazing results of dense lines with high resolution fabricated by DSA of BCP, yet the LWR are not satisfactory.[25]

In conclusion, as a scalable process, this bottom-up lithography can be integrated with traditional photolithography techniques creating an economical sub-20nm patterning solution. However, more understanding about how to control its LWR and LCDU is needed before this technique can really be applied to a production line.

1.2.4 HOLOGRAPHIC LITHOGRAPHY

Holographic lithography or interference lithography (IL), which is based on interference between two or more mutually coherent beams, has been widely used in the fabrication of various periodic nanofeatures. All the 5 2D Bravais lattices and the 15 3D Bravais lattice have been fabricated using IL by changing the polarization, angle of incidence or number of interfering beams. In addition, by using IL, extreme resolution for certain wavelength can be achieved

without a forceful demand for complicated and expensive optics with high numerical aperture. For instance, the period of 1D grating generated by IL is defined as $\lambda/[2\sin(\theta)]$. By changing the angle of incidence, the pitch resolution limit of interference imaging is $\lambda/2$ which is as same as state of art optical lithography system utilized in semiconductor industry.

There has been a variety of optical geometries for IL setup which are designed for different periodic nanostructures to be fabricated. For instance, Lloyd mirror shown in Figure 1.5a) is convenient, robust and commonly used to fabricate 1D or 2D periodic nanostructures. It takes advantages of the spatial and temporal coherence of a laser beam which is intercepted by a mirror and separated into two mutually coherent beams. An interference fringe can be generated by directing the coherent beams onto the same imaging plane creating desired periodic nanopatterns with different lattices [27][28][29]. The most important characteristics of Lloyd mirror lithography are its ultra-high resolution and its flexibility. Using this fabrication method, a 38nm pitch gratings have been conveniently achieved using a 13.4nm synchrotron illumination [30].
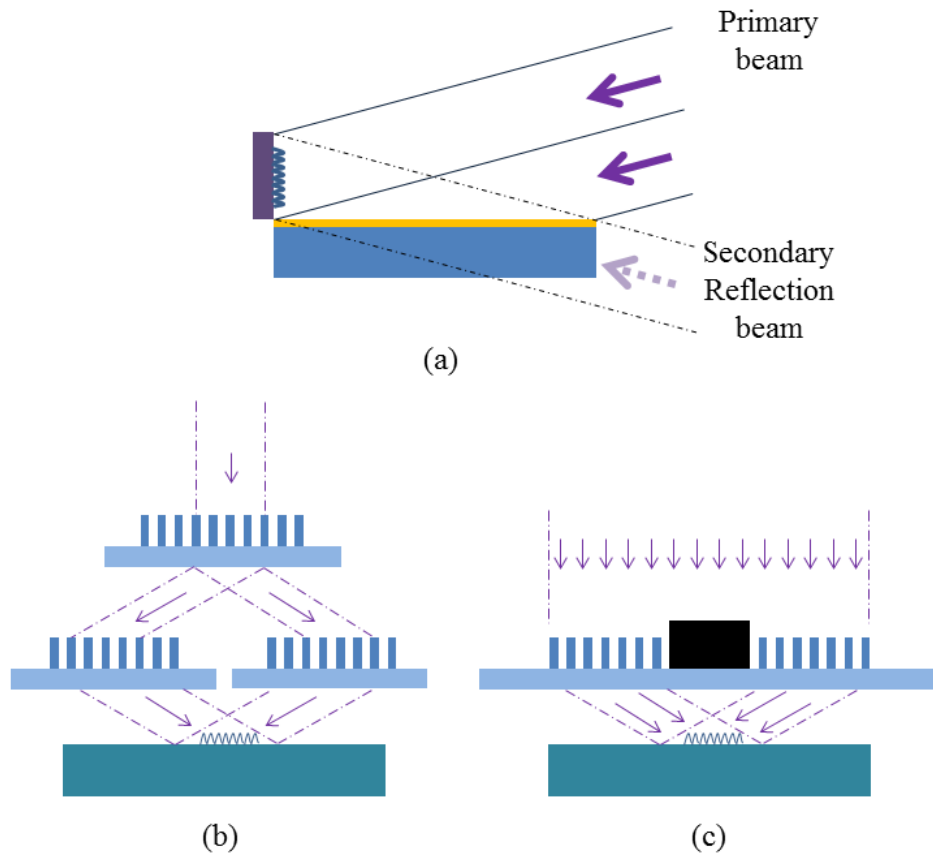
Figure 1.5a): Lloyd's mirror; Figure 1.5b) Achromatic IL system;

Figure 1.5c: IL with single diffraction element

In addition to LM, another optical geometry named as achromatic IL system is illustrated in Figure 1.5 b) [31][32]. In this configuration, first orders of diffracted beams from a 200nm period grating are recombined at resist coated wafer using another pair of identical gratings generating a final pattern on the resist with 100nm period. As the mask fabrication techniques have been evolved, this technique has been simplified into a configuration with only one single diffraction element in which a set of gratings are integrated on one single substrate[33]. The basic experiment scheme is shown in Figure 1.5c). This technique creates another opportunity for IL which is now capable of patterning nanofeatures with critical dimension (CD) as small as 9nm half pitch[34].

IL have also been taking advantages of the polarization of a laser beam generating a 3D helical interference pattern which can be used as chiral metamaterial device with mix electrical and magnetic response[35]. Figure 1.6 demonstrates this experiment results.
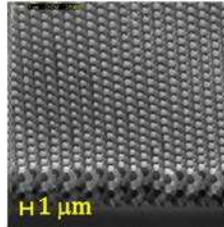
Figure 1.6: Chiral metamaterial fabricated by IL[35]

In conclusion, IL is a straightforward and cost-effective nanofabrication technique with sub-10nm resolution. The CD limit relies on the wavelength and the quality of the laser beam meaning that a coherent monochromatic light source with short wavelength can be quite beneficial to the research in this field. However, IL still suffers from intrinsic drawbacks including difficulty in aligning the image in respect to the pattern on previous level.

1.2.5   *COHERENT DIFFRACTION LITHOGRAPHY (CDL)*

CDL is a mask based self-imaging lithography technique. It depends on a classic Talbot imaging technique[36][37] which is generated by illuminating a mask with periodic pattern with a monochromatic light source. This will reproduce identical periodic structure as the mask repetitively at certain imaging planes named as Talbot planes. The self-assembled image is called Talbot image. CDL is able to accurately replicate periodic patterns from a reticle to the resist coated wafer. With a proper alignment mark, CDL can offer a solution to align the self-assembled image to pre-existing pattern faithfully. The scheme of Talbot image is shown in Figure 1.7[38]. Various functional nanomaterial like photonic crystals with hexagonal lattice in a large area has

been fabricated using this nanofabrication method[37]. However, CDL is limited to fabricate only simple patterns like 1D grating or 2D pillars.
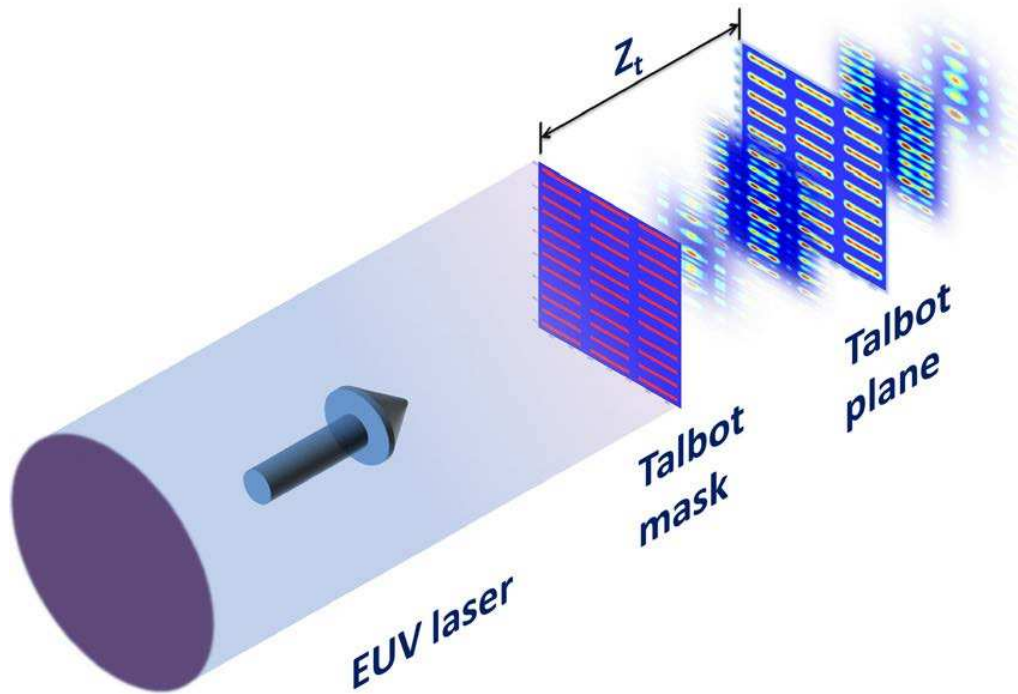
Figure 1.7: Talbot imaging

To make a breakthrough of this limit on pattern design, a generalized Talbot imaging (GTI), which is capable of printing arbitrary periodic pattern, was proposed and studied[39] to obtain an extra degree of freedom. Complex 2D periodic patterns have been fabricated using this method. Details of Talbot effect will be discussed later in chapter 3. Here, as a brief introduction, resolution of Talbot lithography is proportional to the wavelength. The smallest feasible prints or CD limit can be reduced by using a laser with shorter wavelength compared with a 193nm ArF laser commonly used.

1.2.6 COHERENT EXTREME ULTRAVIOLET (EUV) LITHOGRAPHY IN A TABLE-TOP SETUP

A straight forward strategy for IL and GTI to reduce the CD limit is to utilize shorter wavelength, e.g. in the region of EUV or soft X-ray. Synchrotrons sources are able to provide a large photon flux and tunable output with a wavelength in this region. However, the spatial and temporal coherence of the beam are much lower than laser sources usually used in IL or GTI research. To circumvent this problem, a spatial filter is applied to obtain necessary degree of spatial and temporal coherence. Yet, this additional filter immediately reduces the photo flux and increase the exposure time in order to get a reasonable activation of the resist. Moreover, the limit accessibility to these big facilities adds an extra difficulty to the popularization of this lithography technique.

These restrictions have been mitigated by a recent developed compact or table-top EUV lasers which have opened novel possibilities to realize efficient nanopatterning. Classic imaging method like Lloyd mirror[40][41] and Talbot imaging[39][42][43] have been integrated with this novel EUV laser in a table-top setup which is capable of fabricating complex periodic pattern with high resolution cost-effectively.

This dissertation will describe the progress in coherent EUV lithography in a table-top setup. Chapter 2 will focus on the description of 46.9nm capillary discharge EUV laser and 18.9nm amplified spontaneous emission (ASE) laser which were utilized in the nanofabrication setup.

Chapter 3 is fully devoted to a description of EUV Talbot lithography system. The mathematical modelling of Talbot image, experiment setup and etching system for pattern

transfer will be described. In addition, a plasmonic surface sample fabricated by this lithography system is characterized and illustrated. To further scale down the critical dimension (CD) of pattern on the mask, multiple exposure, displacement Talbot lithography and fractional Talbot lithography are examined and demonstrated as well. Part of the results in this chapter are published in [38][44][45].

Chapter 4 will describe a hybrid extreme ultraviolet lithography approach that combines Talbot lithography and interference lithography to render an interference pattern with a lattice determined by a Talbot image. As a result, the method enables filling the arbitrary shaped cells produced by the Talbot image with interference patterns. Detailed modeling, system design and experimental results using a tabletop EUV laser are presented. The work in this chapter has been published in [46].

REFERENCE:

[1]   J. Valentine, S. Zhang, T. Zentgraf, E. Ulin-Avila, D. a Genov, G. Bartal, and X. Zhang, "Three-dimensional optical metamaterial with a negative refractive index.," *Nature*, vol. 455, no. September, pp. 376–379, 2008.

[2]   J. B. Pendry, "A chiral route to negative refraction.," *Science*, vol. 306, no. 5700, pp. 1353–5, Nov. 2004.

[3]   R. Maas, J. Parsons, N. Engheta, and A. Polman, "Experimental realization of an epsilon-near-zero metamaterial at visible wavelengths," *Nat. Photonics*, vol. 7, no. 11, pp. 907–912, 2013.

[4]   Y. Akahane, T. Asano, and B. Song, "High- Q photonic nanocavity in a two-dimensional photonic crystal," *Nature*, vol. 425, pp. 944–946, 2003.

[5]   M. Notomi, A. Shinya, S. Mitsugi, G. Kira, E. Kuramochi, and T. Tanabe, "Optical bistable switching action of Si high-Q photonic-crystal nanocavities.," *Opt. Express*, vol. 13, no. 7, pp. 2678–2687, 2005.

[6]   L. J. Heyderman, H. H. Solak, C. David, D. Atkinson, R. P. Cowburn, and F. Nolting, "Arrays of nanoscale magnetic dots: Fabrication by x-ray interference lithography and characterization," *Appl. Phys. Lett.*, vol. 85, no. 2004, pp. 4989–4991, 2004.

[7]   D. M. Callahan, J. N. Munday, H. A. Atwater, and R. Khanna, "Solar Cell Light Trapping beyond the ray optic limit," vol. 12, pp. 214–218, 2012.

[8]   V. E. Ferry, L. A. Sweatlock, D. Pacifici, and H. A. Atwater, "Plasmonic nanostructure design for efficient light coupling into solar cells," *Nano Lett.*, vol. 8, no. 12, pp. 4391–4397, 2008.

[9]   A. Kriesch, S. P. Burgos, D. Ploss, H. Pfeifer, H. A. Atwater, and U. Peschel, "Functional plasmonic nanocircuits with low insertion and propagation losses," *Nano Lett.*, vol. 13, no. 9, pp. 4539–4545, 2013.

[10]   W. (Walter) Hu, K. Sarveswaran, M. Lieberman, and G. H. Bernstein, "Sub-10 nm electron beam lithography using cold development of poly(methylmethacrylate)," *J. Vac. Sci. Technol. B Microelectron. Nanom. Struct.*, vol. 22, no. 4, p. 1711, 2004.

[11]   H. Duan, D. Winston, J. K. W. Yang, B. M. Cord, V. R. Manfrinato, and K. K. Berggren, "Sub-10-nm half-pitch electron-beam lithography by using poly(methyl methacrylate) as a negative resist," *J. Vac. Sci. Technol. B Microelectron. Nanom. Struct.*, vol. 28, no. 6, p. C6C58, 2010.

[12]   L. J. Guo, "Nanoimprint lithography: Methods and material requirements," *Adv. Mater.*, vol. 19, no. 4, pp. 495–513, 2007.

[13]   M. D. Austin, H. Ge, W. Wu, M. Li, Z. Yu, D. Wasserman, S. A. Lyon, and S. Y. Chou, "Fabrication of 5 nm linewidth and 14 nm pitch features by nanoimprint lithography," *Appl. Phys. Lett.*, vol. 84, no. 26, pp. 5299–5301, 2004.

[14]   V. E. Ferry, M. A. Verschuuren, H. B. T. Li, R. E. I. Schropp, H. A. Atwater, and A. Polman, "Improved red-response in thin film a-Si:H solar cells with soft-imprinted plasmonic back reflectors," *Appl. Phys. Lett.*, vol. 95, no. 18, p. 183503, 2009.

[15] S. Y. Chou, "Patterned magnetic nanostructures and quantized magnetic disks," *Proc. IEEE*, vol. 85, no. 4, pp. 652–671, 1997.

[16] Y. Sun and S. R. Forrest, "Organic light emitting devices with enhanced outcoupling via microlenses fabricated by imprint lithography," *J. Appl. Phys.*, vol. 100, no. 7, pp. 1–6, 2006.

[17] Y. Hirai, S. Yoshida, and N. Takagi, "Defect analysis in thermal nanoimprint lithography," *J. Vac. Sci. Technol. B Microelectron. Nanom. Struct.*, vol. 21, no. 6, p. 2765, 2003.

[18] T. Bailey, B. Smith, B. J. Choi, M. Colburn, M. Meissl, S. V. Sreenivasan, J. G. Ekerdt, and C. G. Willson, "Step and flash imprint lithography: Defect analysis," *J. Vac. Sci. Technol. B Microelectron. Nanom. Struct.*, vol. 19, no. 6, p. 2806, 2001.

[19] C. R. K. Marrian and D. M. Tennant, "Nanofabrication," *J. Vac. Sci. Technol. A Vacuum, Surfaces, Film.*, vol. 21, no. 5, p. S207, 2003.

[20] R. Ruiz, H. Kang, F. a Detcheverry, E. Dobisz, D. S. Kercher, T. R. Albrecht, J. J. de Pablo, and P. F. Nealey, "Density multiplication and improved lithography by directed block copolymer assembly.," *Science*, vol. 321, no. August, pp. 936–939, 2008.

[21] C. Simao, N. Kehagias, D. Borah, B. Kosmala, M. Salaun, M. Zelsmann, M. A. Morris, and C. M. Sotomayor Torres, "Sub-20 nm nanofabrication via nanoimprint directed self-assembly of block copolymers," *Micro- Nano-Engineering Conf. MNE 2012*, no. 11, pp. 8523–8531, 2012.

[22] Y. S. Jung and C. A. Ross, "Orientation-controlled self-assembled nanolithography using a polystyrene - polydimethylsiloxane block copolymer," *Nano Lett.*, vol. 7, no. 7, pp. 2046–2050, 2007.

[23] M. P. Stoykovich, M. Müller, S. O. Kim, H. H. Solak, E. W. Edwards, J. J. de Pablo, and P. F. Nealey, "Directed assembly of block copolymer blends into nonregular device-oriented structures.," *Science*, vol. 308, no. 5727, pp. 1442–1446, 2005.

[24] R. Ruiz, E. Dobisz, and T. R. Albrecht, "Rectangular Patterns Using Block Copolymer Directed Assembly for High Bit Aspect Ratio Patterned Media," *ACS Nano*, vol. 5, no. 1, pp. 79–84, 2011.

[25] J. Cushen, L. Wan, G. Blachut, M. J. Maher, T. R. Albrecht, C. J. Ellison, C. G. Willson, and R. Ruiz, "Double-Patterned Sidewall Directed Self-Assembly and Pattern Transfer of Sub-10 nm PTMSS- *b* -PMOST," *ACS Appl. Mater. Interfaces*, vol. 7, no. 24, pp. 13476–13483, 2015.

[26] L. Wan, R. Ruiz, H. Gao, K. C. Patel, and T. R. Albrecht, "The Limits of Lamellae-Forming PS-b-PMMA Block Copolymers for Lithography," *ACS Nano*, vol. 9, no. 7, pp. 7506–7514, 2015.

[27] J. de Boor, N. Geyer, U. Gösele, and V. Schmidt, "Three-beam interference lithography: upgrading a Lloyd's interferometer for single-exposure hexagonal patterning.," *Opt. Lett.*, vol. 34, no. 12, pp. 1783–1785, 2009.

[28] J. de Boor, D. S. Kim, and V. Schmidt, "Sub-50 nm patterning by immersion interference lithography using a Littrow prism as a Lloyd's interferometer.," *Opt. Lett.*, vol. 35, no. 20, pp. 3450–3452, 2010.

[29] M. Vala and J. Homola, "Flexible method based on four-beam interference lithography for fabrication of large areas of perfectly periodic plasmonic arrays," *Opt. Express*, vol. 22, no. 15, p. 18778, 2014.

[30] H. H. Solak, D. He, W. Li, S. Singh-Gasson, F. Cerrina, B. H. Sohn, X. M. Yang, and P. Nealey, "Exposure of 38 nm period grating patterns with extreme ultraviolet interferometric lithography," *Appl. Phys. Lett.*, vol. 75, no. 15, p. 2328, 1999.

[31] T. A. Savas, M. Farhoud, H. I. Smith, M. Hwang, and C. A. Ross, "Properties of large-area nanomagnet arrays with 100 nm period made by interferometric lithography," *J. Appl. Phys.*, vol. 85, no. 8, p. 6160, 1999.

[32] J. O. Choi, H. S. Jeong, D. G. Pflug, A. I. Akinwande, and H. I. Smith, "Fabrication of 0.1 μm gate aperture Mo-tip field-emitter arrays using interferometric lithography," *Appl. Phys. Lett.*, vol. 74, no. 20, p. 3050, 1999.

[33] I. Divliansky, T. S. Mayer, K. S. Holliday, and V. H. Crespi, "Fabrication of three-dimensional polymer photonic crystal structures using single diffraction element interference lithography," *Appl. Phys. Lett.*, vol. 82, no. 11, p. 1667, 2003.

[34] B. Päivänranta, A. Langner, E. Kirk, C. David, and Y. Ekinci, "Sub-10 nm patterning using EUV interference lithography," *Nanotechnology*, vol. 22, no. 37, p. 375302, 2011.

[35] A. K. Raub and S. R. J. Brueck, "Large area 3D helical photonic crystals," *J. Vac. Sci. Technol. B Microelectron. Nanom. Struct.*, vol. 29, no. 2011, p. 06FF02, 2011.

[36] C. P. Fucetola, A. A. Patel, E. E. Moon, T. B. O'Reilly, and H. I. Smith, "Coherent diffraction lithography: Periodic patterns via mask-based interference lithography," *J. Vac. Sci. Technol. B Microelectron. Nanom. Struct.*, vol. 27, no. 6, pp. 2947–2950, 2009.

[37] C. Zanke, M. Qi, and H. I. Smith, "Large-area patterning for photonic crystals via coherent diffraction lithography," *J. Vac. Sci. Technol. B Microelectron. Nanom. Struct.*, vol. 22, no. 6, pp. 3352–3355, 2004.

[38] W. Li, V. M. Esquiroz, L. Urbanski, D. Patel, C. S. Menoni, M. C. Marconi, A. Stein, W. Chao, and E. H. Anderson, "Defect-free periodic structures using extreme ultraviolet Talbot lithography in a table-top system," *J. Vac. Sci. Technol. B Microelectron. Nanom. Struct.*, vol. 31, no. 6, p. 06F604, 2013.

[39] A. Isoyan, F. Jiang, Y. C. Cheng, F. Cerrina, P. Wachulak, L. Urbanski, J. Rocca, C. Menoni, and M. Marconi, "Talbot lithography: Self-imaging of complex structures," *J. Vac. Sci. Technol. B Microelectron. Nanom. Struct.*, vol. 27, p. 2931, 2009.

[40] P. W. Wachulak, M. G. Capeluto, M. C. Marconi, C. S. Menoni, and J. J. Rocca, "Patterning of nano-scale arrays by table-top extreme ultraviolet laser interferometric lithography.," *Opt. Express*, vol. 15, no. 6, pp. 3465–3469, 2007.

[41] P. W. Wachulak, M. G. Capeluto, M. C. Marconi, D. Patel, C. S. Menoni, and J. J. Rocca, "Nanoscale patterning in high resolution HSQ photoresist by interferometric lithography with tabletop extreme ultraviolet lasers," *J. Vac. Sci. Technol. B Microelectron. Nanom. Struct.*, vol. 25, no. 6, p. 2094, 2007.

[42] L. Urbanski, M. C. Marconi, A. Isoyan, A. Stein, C. S. Menoni, and J. J. Rocca, "Analysis of a scheme for de-magnified Talbot lithography," *J. Vac. Sci. Technol. B Microelectron. Nanom. Struct.*, vol. 29, no. 6, p. 06F504, 2011.

[43] L. Urbanski, A. Isoyan, A. Stein, J. J. Rocca, C. S. Menoni, and M. C. Marconi, "Defect-tolerant extreme ultraviolet nanoscale printing," *Opt. Lett.*, vol. 37, no. 17, pp. 3633–3635, 2012.

[44] H. Kim, W. Li, S. Danylyuk, W. S. Brocklesby, M. C. Marconi, and L. Juschkin, "Fractional Talbot lithography with extreme ultraviolet light," *Opt. Lett.*, vol. 39, no. 24, p. 6969, 2014.

[45] B. A. Reagan, W. Li, L. Urbanski, K. A. Wernsing, C. Salsbury, C. Baumgarten, M. C. Marconi, C. S. Menoni, and J. J. Rocca, "Hour-long continuous operation of a tabletop soft x-ray laser at 50-100 Hz repetition rate," vol. 21, no. 23, pp. 1115–1117, 2013.

[46] W. Li and M. C. Marconi, "Extreme ultraviolet Talbot interference lithography," *Opt. Express*, vol. 23, no. 20, p. 25532, 2015.

CHAPTER 2 EXTREME ULTRAVIOLET TABLE TOP LASERS

This chapter describes the table-top light sources used in the coherent EUV lithography project of this dissertation, namely a capillary discharge laser (CDL) and a compact soft X-ray laser (CSXL), both developed at Colorado State University. The CDL is a Ne-like Ar laser operating at 46.9nm. This source has a high photon flux, and high temporal and spacial coherence. It has been utilized in microscopy[1][2], holographic imaging[3], nanoscale patterning[4][5], mass spectrometry[6] among other applications. The CSXL is a Ni-like amplified spontaneous emission (ASE) laser operating at shorter wavelengths between 7nm and 20nm[7][8]. It also has been used as the light source for microscopy[9] and nanopatterning[10].

The physical principle and main properties of these two lasers will be discussed in this chapter including the relevant characteristics to the lithography method described in this thesis: high photon flux and high spatial and temporal coherence.

2.1   CAPILLARY DISCHARGE LASER

Figure 2.1 (a) demonstrates the Grotrian diagram of the energy levels of the Ar^{+8} ion relevant to the operation of the CDL. The upper laser lever is populated by electron impact excitation producing a population inversion between the 3p and the 3s (J=0 to J=1) levels. The population inversion is achieved by rapid excitation of the upper level and a fast relaxation of the lower level to the ground state. Figure 2.1 (b) shows how the electrical pumping is achieved by a fast current discharge through a capillary which is filled with preionized argon. Electromagnetic force quickly compresses the current carrying plasma axially from ~3mm to ~300μm creating a dense needle-shaped plasma column that favor amplification of λ=46.9nm line.
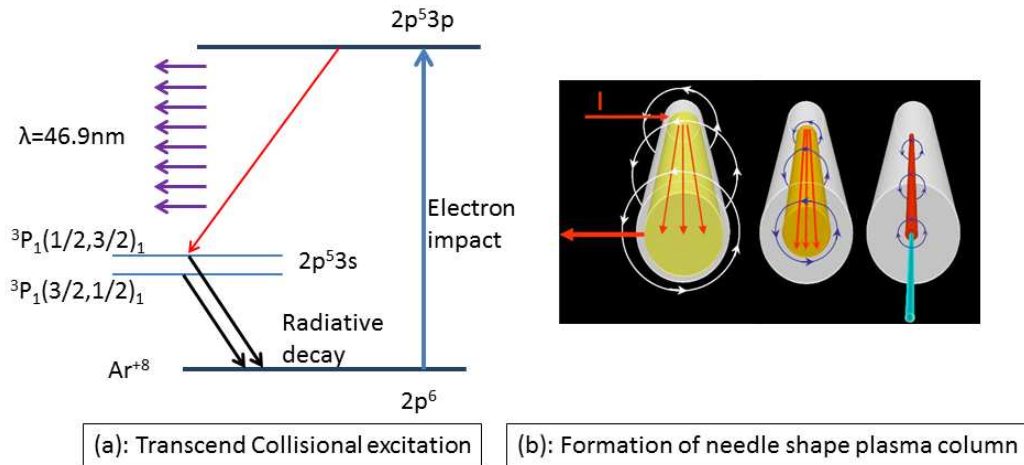
Figure 2.1 Physical model of 46.9nm CDL and plasma column formation in the capillary

2.1.1 HIGH PHOTON FLUX

Figure 2.2 is a schematic of the electrical circuit of the CDL. The fast current pulse is delivered by a RLC circuit consisted of a capacitor, a spark-gap switch and a capillary filled with Ar. The capacitor has a liquid dielectric (deionized water) and can be charged to more than 200kV by a multistage Marx generator. The laser is operated with a continuous argon flow injected from one end of capillary at an optimum pressure of 490mTorr. In this operation conditions, the hot dense plasma column generated by the discharge current pulse achieves an electron temperature around 90eV and an electron density around 1.8×10^{18} cm^{-3}. Population inversion between 3s ^{1}P$_1$-3p ^{1}S$_0$ generates sufficient gain to produce a laser pulse with energies in the range of 0.88mJ at 4Hz repetition rate. This average power is enough to activate photoresists like PMMA or HSQ ([HSiO$_{3/2}$]$_n$) with exposures of about one minute.
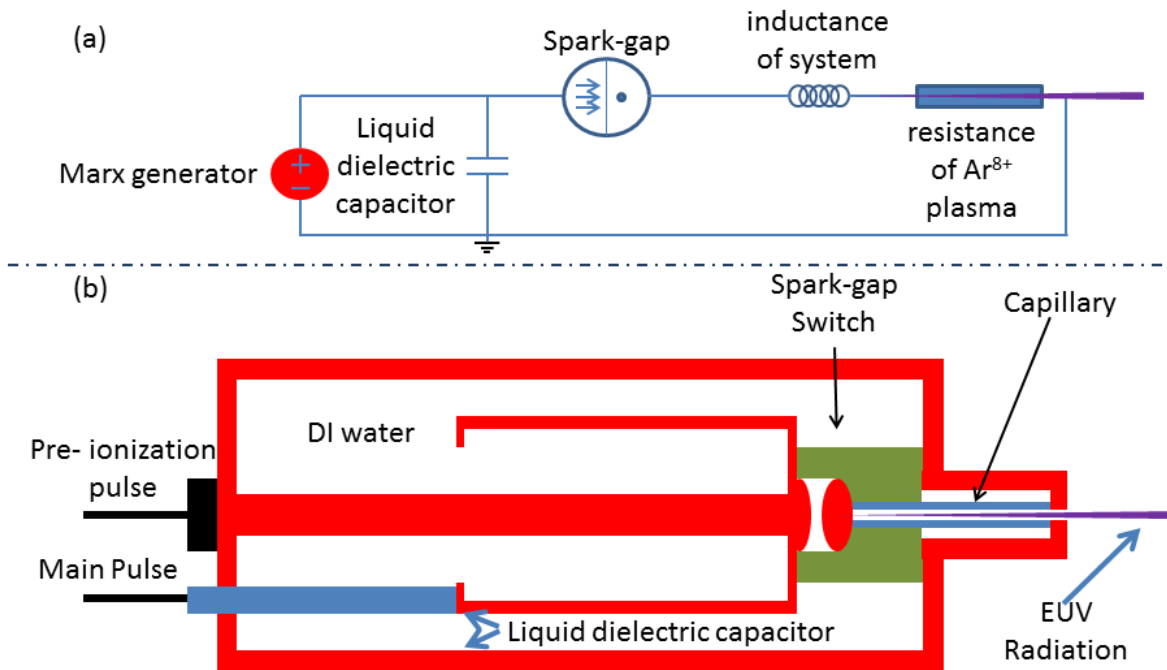
Figure 2.2: Schematic setup for CDL. (a) is the electrical circuit; (b) is the schematic of CDL

2.1.2   SPACIAL COHERENCE OF CDL

The CDL has high degree of spatial coherence which has been measured using a Young's double slit interferometer. The visibility of its interference fringe[11] was measured using an experiment setup which is schematically shown in figure 2.3[11].
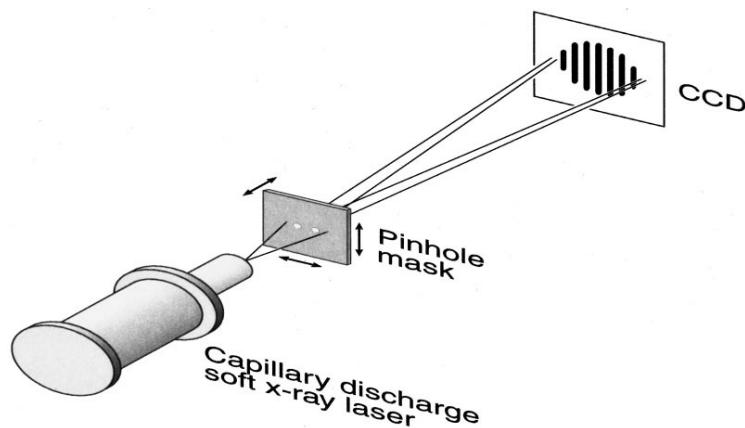
Figure 2.3[11]: Experiment setup for spacial coherence measurement of CDL
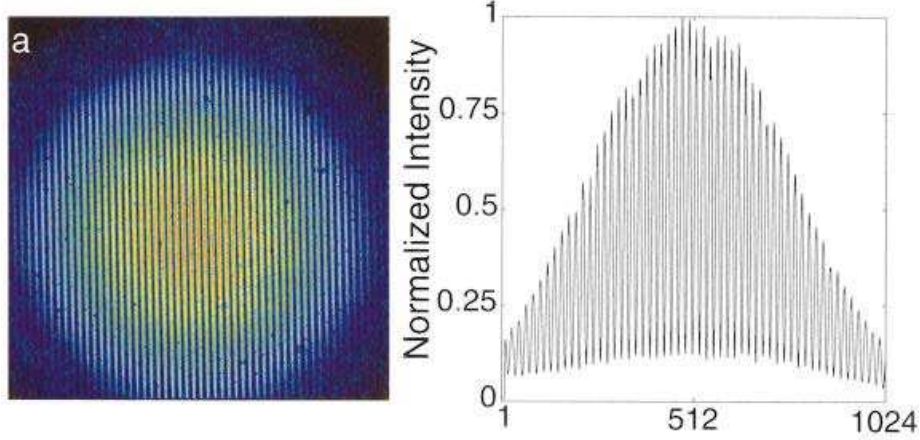
Figure 2.4[11]: Interference fringes for Young's experiment using CDL

A stainless-steel mask with two 10μm diameter pinholes was illuminated by the CDL. The interference pattern produced was recorded 3m away from the mask and is shown in figure 2.4. The intensity maxima and minima are defined as:

$$I_{\min} = I_1 + I_2 - 2\sqrt{I_1 I_2}|\gamma_{12}(\tau)|$$

$$I_{\max} = I_1 + I_2 + 2\sqrt{I_1 I_2}|\gamma_{12}(\tau)|$$

Where, $\gamma_{12}(\tau)$ is the degree of mutual coherence. If we assume that the intensity of the illumination on the two pinholes are equal ($I_1=I_2$, then the visibility of the interference pattern is directly the degree of mutual coherence:

$$V = \frac{I_{max}-I_{min}}{I_{max}+I_{min}} = |\gamma_{12}(\tau)| \tag{2}$$

The visibility was measured at two slit separations ($\tau = 300\mu m$ and $\tau = 680\mu m$). The data were finally fit with a Gaussian function to obtain:

$$|\gamma_{12}(\tau)| = \exp[\frac{\Delta x^2}{2R_c^2}] \tag{3}$$

21

This fit renders a spatial coherence: R_c=550 μm.

2.1.3 TEMPORAL COHERENCE OF CDL

The degree of temporal coherence is also crucial to the lithography method described in this work. A detailed explanation of the importance of the temporal coherence of the source regarding to the quality of Talbot image will be discussed in next chapter.

The measurement of the temporal coherence was conducted using a wavefront division interferometer[12] built with two dihedron mirrors and two flat mirrors designed for EUV light. The beam from the CDL was aligned with the axis of the dihedron mirrors at a 6° incidence angle and then split into two coherent parts which were directed onto a CCD detector creating interference fringes. The scheme of this experiment setup is shown in figure 2.5[12].
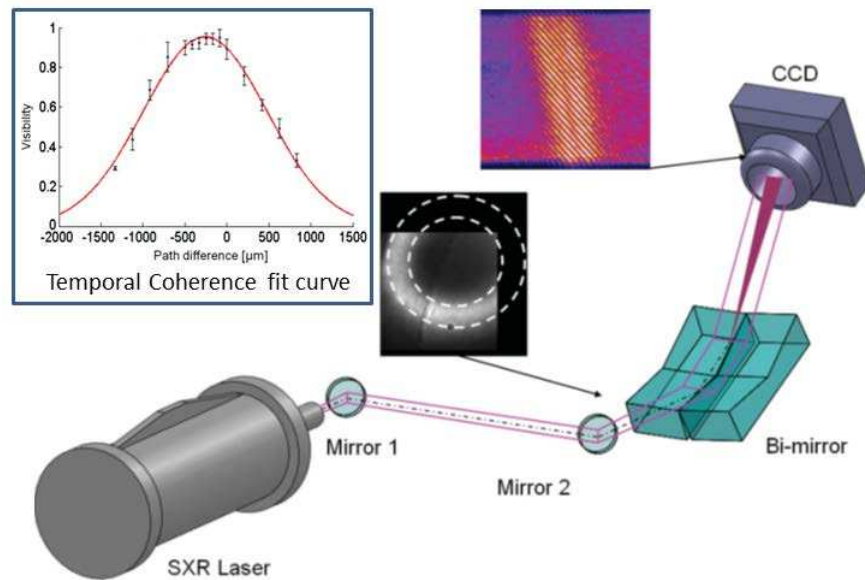
Figure 2.5[12]: experiment setup for measurement of temporal coherence of CDL

By moving one of the dihedron mirrors vertically, the optical path difference (OPD) between the two beams can be controlled. This changing OPD generate interference fringes with various visibilities. Overall, a visibility curve shown in the inset in figure 2.5 can be obtained and

the experiment data fitted into a Gaussian curve shown as red solid line. The temporal coherence length is calculated by the specified OPD where the visibility drops to 1/e of its maximum value. From the experimental data and calculation, the measured linewidth is around $1.66{\times}10^{-3}$ nm or $\frac{\Delta\lambda}{\lambda} = 3.5 \times 10^{-5}$. This leads to a temporal coherence (l_c) around 800µm.

2.2 COMPACT SOFT X-RAY LASER (CSXL)

Besides the 46.9nm CDL, there has always been a permanent need for light source with even shorter wavelength. This demand has motivated the construction of free electron lasers (FEL) which, however, has a quite limited accessibility. Meanwhile, CSXL with a capability to generate coherent laser beams with wavelength in the range of 7nm to 20nm [8][13], has also been demonstrated in Colorado State University.

These table-top CSXLs are created in hot dense plasmas by focusing a sequence of intense laser pulses into slab targets of selected materials. Different targets renders an emission with different wavelength which is illustrated in Figure 2.7[13].
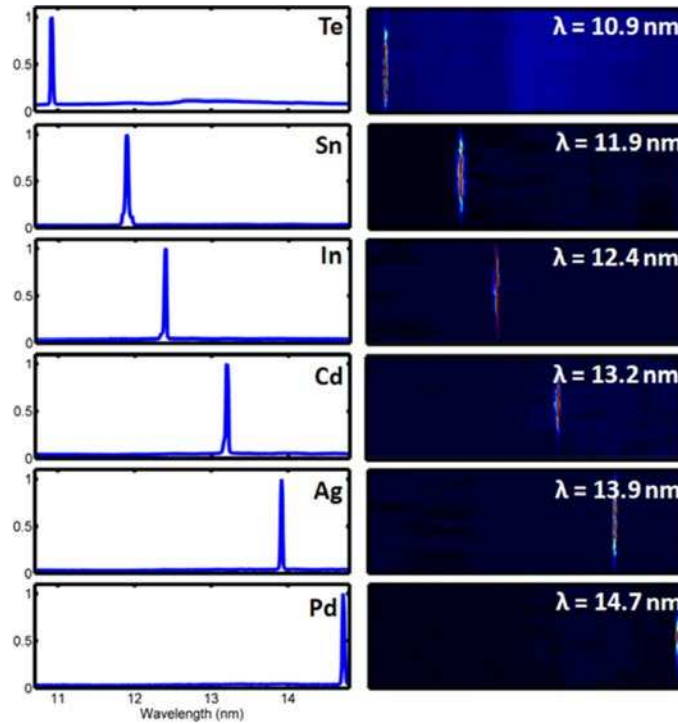
Figure 2.7[13]: Spectrum of CSXL with multiple wavelength using various solid targets

The schematic experimental setup for CSXL is shown in Figure 2.8. The hot dense plasma is generated by a chirped pulse amplifier (CPA) laser. A prepulse is focused on the slab target generating a plasma channel. This is followed by a 5ps full width half maximum (FWHM) main pulse with approximately 1J energy which is used as the pumping mechanism for transient collisional excitation leading to a population inversion between $4d$ $^1S_0$ and $4p$ $^1P_1$. Both the prepulse and the main pulse are focused into a line channel creating the amplifier for this ASE soft X-ray laser.

24
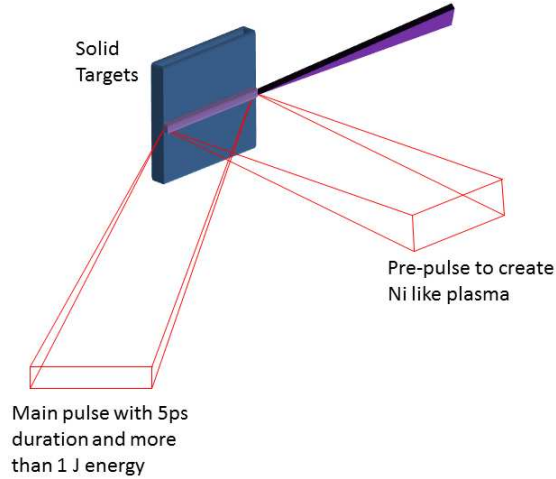
Figure 2.8: Schematic experiment setup for CSXL

The development of diode pump CPA lasers for CSXL has increased the repetition rate of soft X-ray laser up to 100 Hz, with 1.5µJ per pulse. This table-top soft X-ray laser operates at an average power of 0.15mW and it delivers enough flux to be utilized in the demonstration of EUV lithography[10].

To determine the spacial coherence of this CSXL, a Young's double slits interferometer has been set up to measure the visibility of interference fringes (calculation details are the same as the CDL)[14]. It has been calculated that, at 10cm away from the target, the spacial coherence for CSXL is around 150µm.

In addition, the temporal coherence [15] for this CSXL has also been measured using a grating interferometer which indicates a longitudinal coherence length l_c=260µm with $\frac{\Delta\lambda}{\lambda} = 3 \times 10^{-5}$. The experimental data for the linewidth measurement is shown in Figure 2.9[15].
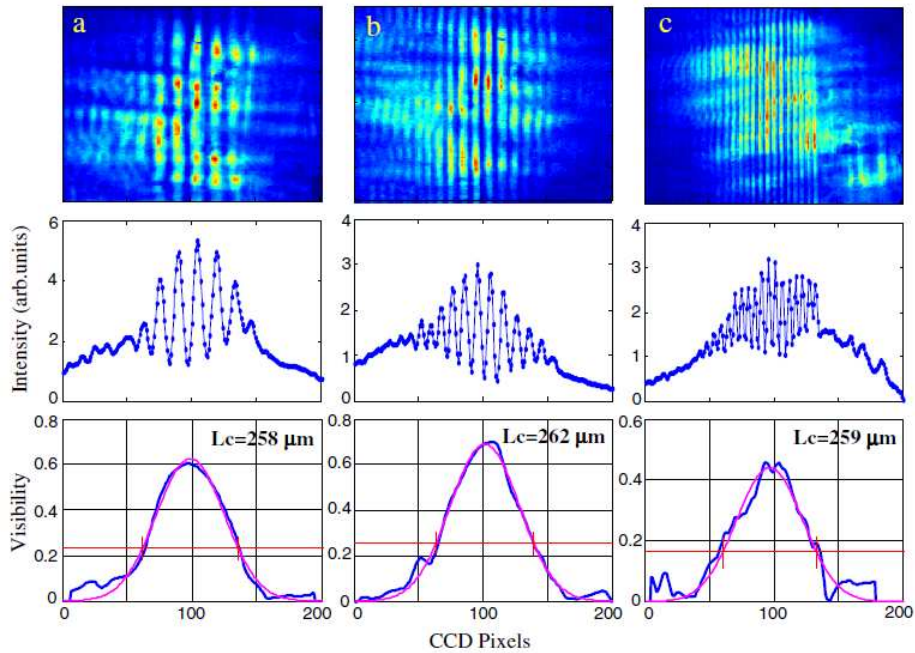
Figure 2.9[15]: temporal coherence of CSXL measured by grating interferometer

2.3 SUMMARY

In this chapter the properties of CDL and CSXL like average power and coherence have been discussed. In the applications described in the following chapters, the influence of these parameters on the resolution, feasibility and exposure time will be discussed for various forms of coherent EUV lithography.

REFERENCE:

[1]   F. Brizuela, I. D. Howlett, S. Carbajo, D. Peterson, A. Sakdinawat, Y. Liu, D. T. Attwood, M. C. Marconi, J. J. Rocca, and C. S. Menoni, "Imaging at the Nanoscale With Practical Table-Top EUV Laser-Based Full-Field Microscopes," *IEEE JOURNAL OF SELECTED TOPICS IN QUANTUM ELECTRONICS*, vol. 18, no. 1, pp. 434–442, 2012.

[2]   S. Carbajo, I. D. Howlett, F. Brizuela, K. S. Buchanan, M. C. Marconi, W. Chao, E. H. Anderson, I. Artioukov, a Vinogradov, J. J. Rocca, and C. S. Menoni, "Sequential single-shot imaging of nanoscale dynamic interactions with a table-top soft x-ray laser.," *Opt. Lett.*, vol. 37, no. 14, pp. 2994–6, 2012.

[3]   P. W. Wachulak, M. C. Marconi, S. Member, R. a Bartels, C. S. Menoni, and J. J. Rocca, "Volume Extreme Ultraviolet Holographic Imaging With Numerical Optical Sectioning," *Opt. Express*, vol. 15, no. 17, pp. 10622–10628, 2007.

[4]   H. Bravo, B. T. Szapiro, P. W. Wachulak, M. C. Marconi, W. L. Chao, E. H. Anderson, C. S. Menoni, and J. J. Rocca, "Demonstration of Nanomachining with Focused Extreme Ultraviolet Laser Beams," *IEEE J. Sel. Top. Quantum Electron.*, vol. 18, no. 1, pp. 443–448, 2011.

[5]   A. Isoyan, F. Jiang, Y. C. Cheng, F. Cerrina, P. Wachulak, L. Urbanski, J. Rocca, C. Menoni, and M. Marconi, "Talbot lithography: Self-imaging of complex structures," *J. Vac. Sci. Technol. B Microelectron. Nanom. Struct.*, vol. 27, p. 2931, 2009.

[6]   I. Kuznetsov, J. Filevich, F. Dong, M. Woolston, W. Chao, E. H. Anderson, E. R. Bernstein, D. C. Crick, J. J. Rocca, and C. S. Menoni, "Three-dimensional nanoscale molecular imaging by extreme ultraviolet laser ablation mass spectrometry.," *Nat. Commun.*, vol. 6, p. 6944, 2015.

[7]   D. Alessi, Y. Wang, B. M. Luther, L. Yin, D. H. Martz, M. R. Woolston, Y. Liu, M. Berrill, and J. J. Rocca, "Efficient Excitation of Gain-Saturated Sub-9-nm-Wavelength Tabletop Soft-X-Ray Lasers and Lasing Down to 7.36 nm," *Phys. Rev. X*, vol. 1, no. 2, pp. 1–6, 2011.

[8]   B. Reagan, K. Wernsing, A. H. Curtis, F. J. Furch, B. M. Luther, D. Patel, C. S. Menoni, and J. J. Rocca, "Demonstration of a 100 Hz repetition rate gain-saturated diode-pumped table-top soft x-ray laser.," *Opt. Lett.*, vol. 37, no. 17, pp. 3624–3626, 2012.

[9]   C. Brewer, G. Vaschenko, F. Brizuela, Y. Wang, M. Larotonda, B. M. Luther, M. C. Marconi, J. J. Rocca, C. S. Menoni, W. Chao, J. Liddle, Y. Liu, E. H. Anderson, and D. T. Attwood, "Sub-38 nm resolution microscopy with a tabletop 13 nm wavelength laser," *Opt. Lett.*, vol. 31, no. 9, pp. 1214–1216, 2006.

[10] B. Reagan, W. Li, L. Urbanski, K. A. Wernsing, C. Salsbury, C. Baumgarten, M. C. Marconi, C. S. Menoni, and J. J. Rocca, "Hour-long continuous operation of a tabletop soft x-ray laser at 50-100 Hz repetition rate," vol. 21, no. 23, pp. 1115–1117, 2013.

[11] Y. Liu, M. Seminario, F. Tomasel, C. Chang, J. Rocca, and D. Attwood, "Achievement of essentially full spatial coherence in a high-average-power soft-x-ray laser," *Phys. Rev. A*, vol. 63, no. 3, p. 033802, Feb. 2001.

[12] L. Urbanski, M. C. Marconi, L. M. Meng, M. Berrill, O. Guilbaud, A. Klisnick, and J. J.

Rocca, "Spectral linewidth of a Ne-like Ar capillary discharge soft-x-ray laser and its dependence on amplification beyond gain saturation," *Phys. Rev. A*, vol. 85, no. 3, p. 033837, Mar. 2012.

[13]   B. Reagan, M. Berrill, K. Wernsing, C. Baumgarten, M. Woolston, and J. J. Rocca, "High-average-power, 100-Hz-repetition-rate, tabletop soft-x-ray lasers at sub-15-nm wavelengths," *Phys. Rev. A*, vol. 89, no. 5, p. 053820, 2014.

[14]   Y. Wang, E. Granados, M. Larotonda, M. Berrill, B. Luther, D. Patel, C. Menoni, and J. Rocca, "High-Brightness Injection-Seeded Soft-X-Ray-Laser Amplifier Using a Solid Target," *Phys. Rev. Lett.*, vol. 97, no. 12, p. 123901, 2006.

[15]   Y. Wang, L. Yin, S. Wang, M. C. Marconi, J. Dunn, E. Gullikson, and J. J. Rocca, "Single-shot soft x-ray laser linewidth measurement using a grating interferometer.," *Opt. Lett.*, vol. 38, no. 23, pp. 5004–7, 2013.

CHAPTER 3 EUV TALBOT LITHOGRAPHY

3.1 INTRODUCTION

This chapter will describe the capabilities of EUV Talbot lithography. Modelling of the imaging technique will be presented followed by the analysis of its resolution and depth of focus (DOF). The experimental setup will be described including the fabrication of the diffractive EUV reticle (Talbot mask) and the design of a dose control unit. After that, the etching system used to transfer the resist pattern into metal thin film will be described.

Additional techniques to further scale down the critical dimension (CD) of the patterns in the mask like multiple exposures, displacement Talbot lithography and fractional Talbot lithography are also examined and discussed.

3.2 MATHEMATICAL MODELLING AND ANALYSIS OF THE RESOLUTION FOR GENERALIZED TALBOT IMAGING (GTI)

EUV Talbot lithography is based on a self-imaging effect named the Talbot effect. When a periodic mask is illuminated with a coherent light source, an identical self-assembled image of the mask appears periodically at certain distances along the direction of illumination. This lens-less imaging phenomenon is called Talbot image and was discovered by H. F. Talbot in 1836[1]. This imaging technique was used for the fabrication of simple periodic patterns like 1D grating or 2D holes/pillars[2]. Isoyan et al. expanded this concept to complex periodic patterns in what was defined as generalized Talbot image (GTI). This section will first prove the GTI mathematically and then will analyze its optical properties like resolution and depth of focus.

The experiment set up of the GTI is shown schematically in Figure 3.1. A periodic semitransparent mask (or Talbot mask shown as a back square with yellow elbows) is

illuminated by the EUV laser. The self-imaging Talbot effect renders a 1:1 replica of the intensity distribution at the mask in the different Talbot planes located at multiples of the Talbot distance Z_t which is defined as $Z_t = \frac{2p^2}{\lambda}$, where p is the period of the structure in the mask and λ is the wavelength of illumination. The Talbot image generated by the mask is used to activate a photoresist coated substrate to complete the lithography process. This technique is defined as Talbot lithography. Figure 3.1 also depicts a "Talbot carpet". It is a 2D pseudo-color map for the intensity of the diffracted light from the periodic reticle. The graph depicted in Figure 3.1 represents a X-Z plane slice of the light intensity passing through a periodic grating whose transmission is represented by $T(\xi)$. In the map, the coherent illumination propagates from top to bottom along Z-axis.
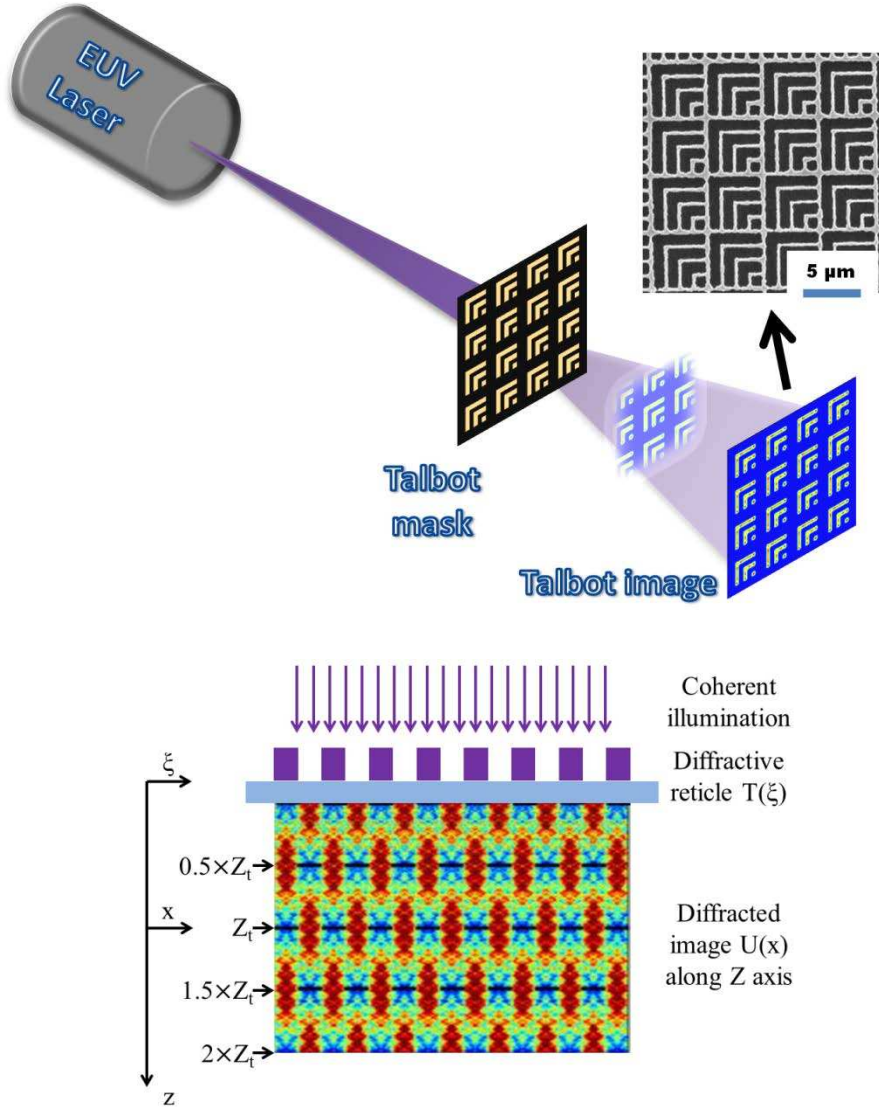
Figure 3.1: Scheme of Fresnel diffraction and carpet of Talbot images

To calculate the Talbot image, the Kirchhoff propagation integral in the Fresnel approximation was used [3]. For simplicity, a one-dimensional arbitrary periodic pattern is used in this calculation, but the conclusions are completely general and the formalism can be extended to two dimensional structures. The function $T(\xi) = T(\xi + P)$ is defined as the intensity transmission function for the diffractive reticle shown in Figure 3.1. It can be expressed as a Fourier series:

$$T(\xi) = \sum_m C_m * \exp\left(j2\pi \frac{m\xi}{P}\right) \qquad\qquad 3\text{-}1$$

Where, m is an integer number, C_m are the Fourier coefficients and P is the period of the reticle.

The diffracted wave [3] in the regime of the Fresnel approximation can be expressed as:

$$U(x) = U(\xi) \otimes h(x) \qquad\qquad 3\text{-}2$$

Where $U(\xi) = T(\xi)$ and $h(x) = \frac{\exp(jkz)}{j\lambda z}\exp\left(\frac{jk}{2z}x^2\right)$

Replacing $k = \frac{2\pi}{\lambda}$, $U(\xi)$ and $h(x)$ into the Fresnel equation, now:

$$U(x) = T(\xi) \otimes h(x) = \mathcal{F}^{-1}\{\mathcal{F}[T(\xi)] * \mathcal{F}[h(x)]\}$$

$$= \mathcal{F}^{-1}\left\{\mathcal{F}\left[\sum_m C_m \times \exp\left(j2\pi\frac{m\xi}{P}\right)\right] * \mathcal{F}\left[\frac{\exp(jkz)}{j\lambda z}\exp\left(\frac{jk}{2z}x^2\right)\right]\right\}$$

$$= \frac{\exp(jkz)}{j\lambda z}\mathcal{F}^{-1}\left\{\sum_m C_m * \mathcal{F}\left[\exp\left(j2\pi\frac{m\xi}{P}\right)\right] * \mathcal{F}\left[\exp\left(\frac{jk}{2z}x^2\right)\right]\right\}$$

$$= \frac{\exp(jkz)}{j\lambda z}\mathcal{F}^{-1}\left\{\sum_m C_m * \delta\left(f_\xi - \frac{m}{P}\right) * \left[\frac{j}{\sqrt{z\lambda}} * \exp(-j\pi * z\lambda * f_x^2)\right]\right\}$$

$$U(x) = \frac{\exp(jkz)}{(\lambda z)^{1.5}}\sum_m C_m * \mathcal{F}^{-1}\left\{\delta\left(f_\xi - \frac{m}{P}\right) * \left[\exp\left(-j\pi * z\lambda * \frac{m^2}{P^2}\right)\right]\right\} \qquad 3\text{-}3$$

Here, if $z = n * \frac{2P^2}{\lambda}$, where n is an integer,

$$\exp\left(-j\pi * z\lambda \frac{m^2}{P^2}\right) = \exp(-j2N\pi) = \cos(-2N\pi) + j\sin(-2N\pi) = 1$$

Where, $N = n*m^2$ is also an integer number

Then $U(x) = \frac{\exp(jkz)}{(\lambda z)^{1.5}} \sum_m C_m * \mathcal{F}^{-1}\left\{ \delta\left(f_\xi - \frac{m}{P} \right) \right\}$

$$= \frac{\exp(jkz)}{(\lambda z)^{1.5}} * \sum_m C_m * \exp\left(j2\pi \frac{m\xi}{P} \right)$$

This makes $U(x) = K * T(\xi)$, where K is a constant, rendering a self-assembled periodic image

when $z = n \times z_t = n\frac{2p^2}{\lambda}$ (so called the Talbot distance). With equation 3-3, the GTI concept is

mathematically proved.

The numerical simulation was performed using Matlab. Appendix I includes a complete

Matlab script for the code that calculates the GTI. Figure 3.2 shows an example of the

calculation. The periodic mask is defined as transparent stars in an opaque background with a

period of 5×5µm² in both X and Y directions. In this calculation there are 50×50 cells on the

mask all together. Figure 3.2 (a) shows a section of the binary mask used in the simulation.

Figure 3.2 (b) is the simulated Talbot image at $Z=1 \times Z_t$ using the mask shown in Figure 3.2 (a)

and a coherent illumination with λ=46.9nm.
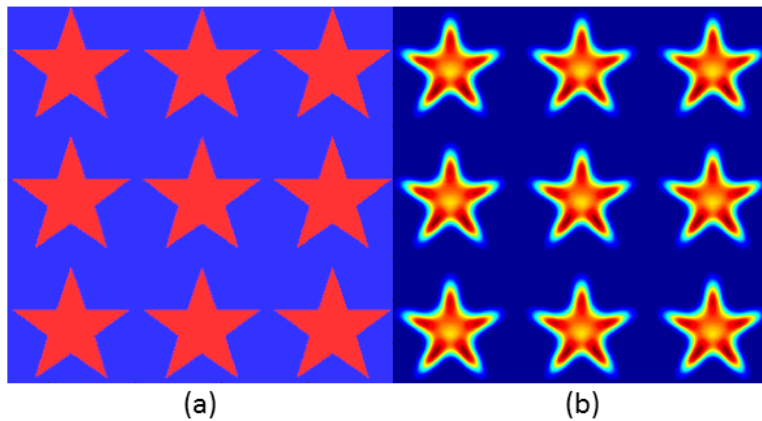

(a)   (b)

Figure 3.2: Simulation results of Talbot image. (a) is the binary Talbot mask, (b) is the simulated Talbot image at

$Z=1 \times Z_t$

The calculated image clearly shows a replica of the periodic Talbot mask, however, the self-assembled reconstruction has a resolution limitation that is clearly noticeable by the blurry tips of the stars in the image shown in Figure 3.2 (b). Conceptually, we can analyze the resolution referring to equation 3-1 which is valid only when the mask is periodic and infinite. However, the mask has a finite size and the source has a finite spacial coherence. This leads to a limited resolution for the Talbot lithography technique.

This resolution limit can be estimated quantitatively analyzing the numerical aperture of the exposure. The numerical aperture (NA) characterizes the range of incidence angles that an optical system can propagate. However, for GTI, only a virtual NA can be defined since there is no optics used in this imaging system. The schematic of the definition for this virtual NA is shown in Figure 3.3. With the lateral size of the Talbot pattern equals to 2W, the NA of Talbot imaging system can be defined as: $NA = \sin^{-1}[\frac{W}{\sqrt{W^2+(nZ_t)^2}}]$. This NA is equivalent to the one for a standard optical system. Note that this NA is changing with the different mask-wafer gaps ($n{\times}Z_t$) which can be different multiples of Talbot distances (Z_t).
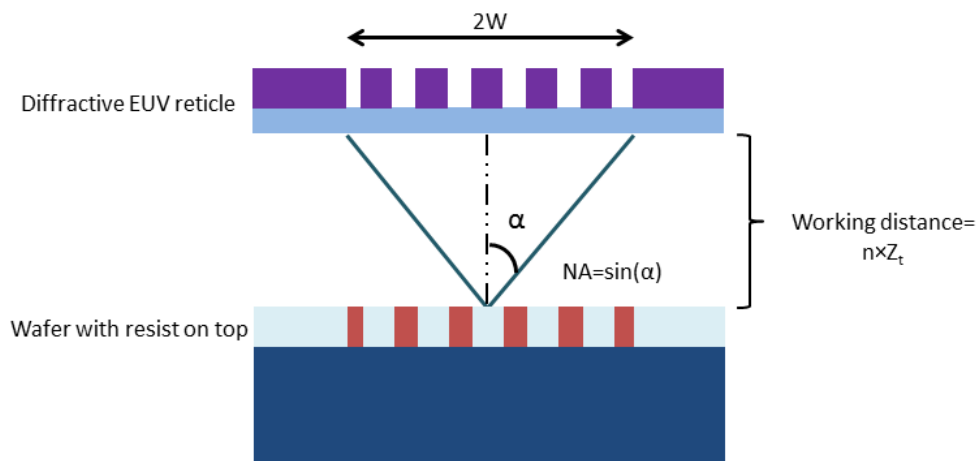
Figure 3.3: NA definition

Larger NA for the GTI will lead to higher resolutions. As an analogy to classic optical system, the resolution for the GTI can be estimated as: $s = \dfrac{\lambda}{NA}$. The pitch resolution is the smallest period of the nanofeatures printable by an imaging system.

To prove the validity of the equation for s, simulations for Talbot images using different masks with different periods were conducted. The simulation results are shown in Figure 3.4. Each data point represents a simulated Talbot image. The size of all the different masks are identical (W=20μm) and they are illuminated by the same coherent light source (λ=46.9nm). To evaluate only the influence of the period of the grating, the same NA was used for all the simulation.

Figure 3.4: pitch resolution regarding to contrast of Talbot image

35

To guarantee the same NA for all the simulations, all the data points are calculated at almost the same wafer-mask gap ($Z=n\times Z_t$). As discussed before, the Talbot distance Z_t depends on the masks' periods. However, the value of n (the order of Talbot plane) can be adjusted at will because the Talbot image periodically appears along the direction of illumination. This means the mask-wafer gap can be controlled w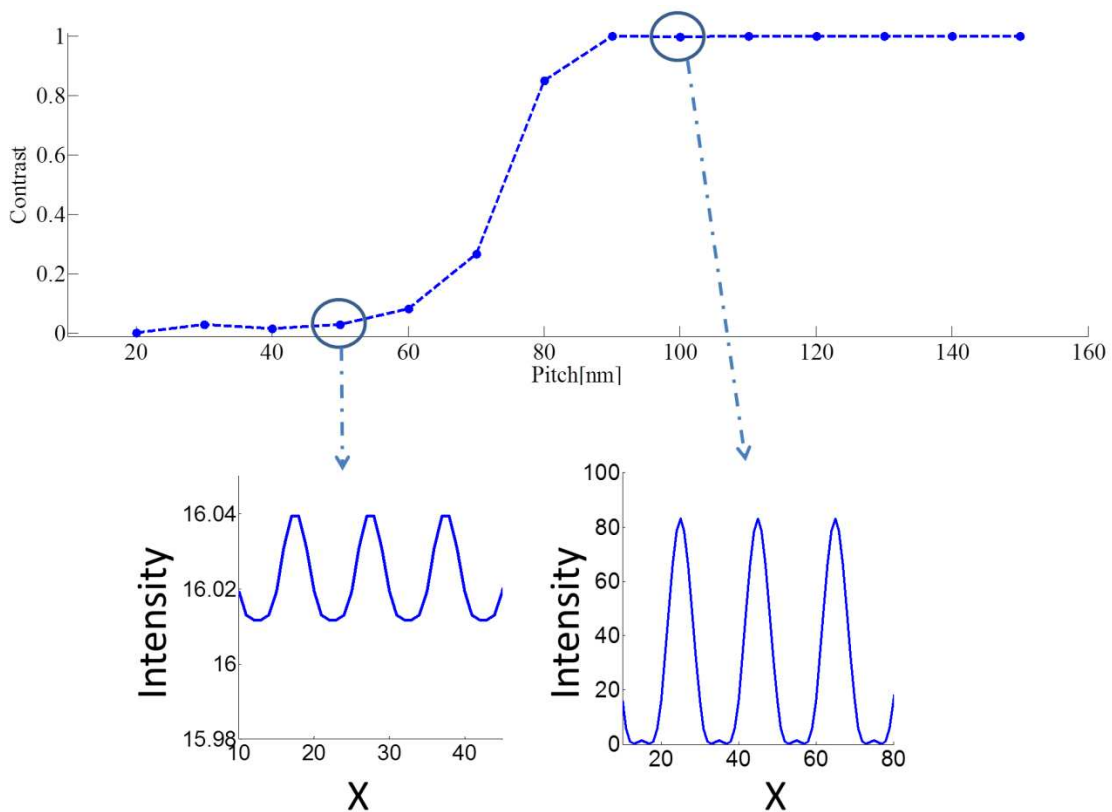ithin an error of one Talbot distance (Z_t). For example, if P=150nm (the largest pitch in Figure 3.4), the Talbot distance is Z_t=0.96 µm using a 46.9nm laser as light source. This means the mask-wafer gap for this particular Talbot lithography setting can be n×0.96 µm. In this way, the mask-wafer gap can be controlled within an error of 0.96µm. By choosing different Talbot planes for the different masks, the NA can be adjusted to be the same in all simulations. Each simulation is one data point in Figure 3.4.

The resolution limit is evaluated by the visibility or contrast of the Talbot image, which is defined as: $v = \frac{I_{max}-I_{min}}{I_{max}+I_{min}}$. Where I_{max} and I_{min} are the maximum and minimum intensities in the Talbot image. Each data point in Figure 3.4 is calculated using this definition from a simulated Talbot image. All the simulated Talbot images are calculated and plotted in Figure 3.4. For instance, the simulation results for one-dimensional gratings with 50nm and 100nm period are shown at the bottom part of Figure 3.4. A high contrast Talbot image can be obtained if the grating has a period larger than 75nm. If the period is smaller than 75nm, as shown in the figure, the contrast of the Talbot image is smaller than 0.5.

The other aspect that has to be considered in the lithography process is the non-linear response of the photoresist. To simulate the effect of the photo resist, a sigmoid function was applied to the calculated Talbot image. A sigmoid function is defined as:

$$\text{sig}(u) = \frac{1}{1+\exp[-a\times(u-t_r)]}$$

36

If the threshold (t_r) of the sigmoid function is 0.5, the contrast of the optical image has to be larger than 0.5 in order to get a desired resist profile after development. Judging from the simulation results, the pitch resolution of the Talbot lithography is around 75nm when NA=0.5 and λ=46.9nm. The threshold of the sigmoid function varies with different photoresists and the number used here is a reasonable estimation for photoresist commonly used like PMMA or HSQ.

In conclusion, this simulation results shows that Talbot the lithography has a pitch resolution *s*=75nm which is in the same order with the estimation using equation *s*=*λ*/*NA*=94nm.

Another parameter that has to be evaluated is the depth of focus (DOF), which limits the thickness of photoresist and the planarity of the sample. The depth of focus or depth of field in a classic optical system with lenses is defined as the amount of defocus that introduces a ±0.25*λ* wavefront error. Mathematically, it can be calculated by: $DOF = \frac{\lambda}{NA^2}$ [5][6].
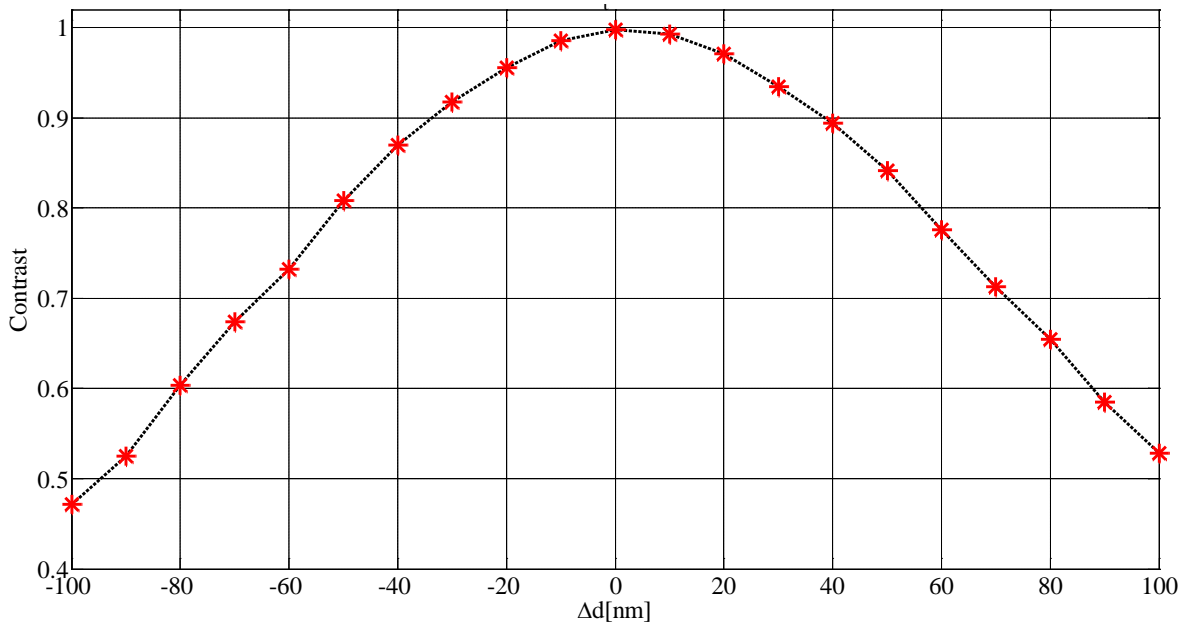

Figure 3.5: Depth of focus for GTI with a 100nm half pitch grating and 46.9nm illumination

As an analogy to the classic optical imaging system, the DOF of the GTI is the permitted displacement, away from the Talbot distances, for which the image contrast is higher than the threshold (t_r). As explained previously, this threshold is photoresist dependent and it can be estimated as 0.5 if common photoresists like PMMA or HSQ are used to record the Talbot image.

Similarly the DOF of the GTI can be approximated with the same expression as a classic optical system. To prove this analogy, another simulation experiment was conducted. The results are shown in Figure 3.5. This numerical simulation was performed using a fixed illumination (λ=46.9nm) and a mask consisting in a grating with 100nm half pitch. The image was calculated at different distances Z around the Talbot distance Z_t. In the plot in Figure 3.5, Δd is the difference between Z and Z_t. For all the calculated images NA is around 0.5. From Figure 3.5, the DOF can be estimated to be approximately 200nm (assuming a contrast of 0.5). This estimation relates very well with the classical expression $DOF = \frac{\lambda}{NA^2} = 188nm$.

As a brief summary, in this section the imaging theory for GTI was mathematically illustrated. The resolution and DOF of the GTI can be estimated using an analogy to classic optical system with a definition of a "virtual" NA $= \frac{1}{\sqrt{1+\left(\frac{n\times Z_t}{W}\right)^2}}$. The pitch resolution and DOF can be estimated as $s = \frac{\lambda}{NA}$ and $DOF = \frac{\lambda}{NA^2}$ respectively.

3.3   EXPERIMENT SETUP FOR THE EUV TALBOT LITHOGRAPHY

Figure 3.6 shows the typical process flow for optical lithography: wafer preparation, exposure, development and pattern transfer. The photoresist that is a photon sensitive material is first spin-coated on top of the substrate (for example a silicon wafer). It is then exposed by

Talbot lithography creating the desired chemical contrast in the photoresist. The development process washes away either the exposed part or unexposed parts (depending on the positive or negative tone of the product). This resist profile serves as a sacrificial mask to transfer the surface pattern from resist to functional layer underneath by etching.
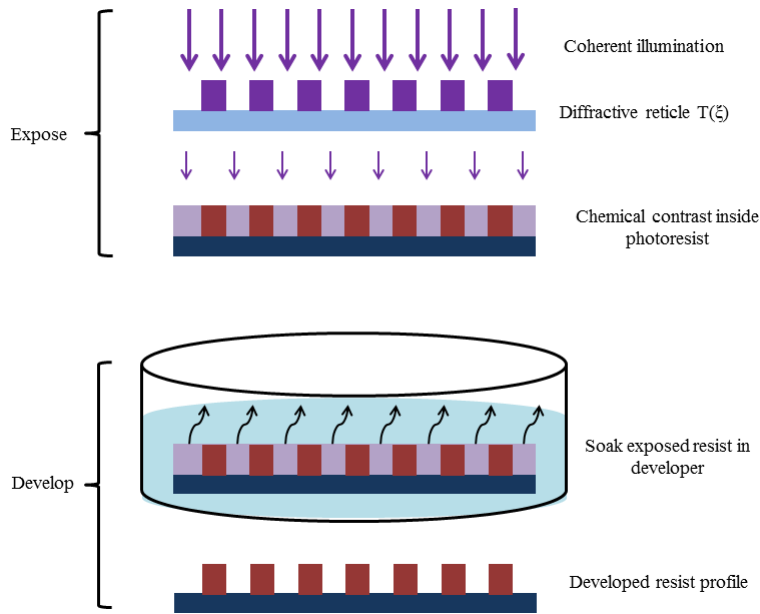

Figure 3.6: Main process flow of optical lithography

Figure 3.7 illustrates the EUV Talbot lithography system developed in this work. It consists of the coherent light source (EUV laser), a membrane supported mask, positioning system and the photoresist coated wafer. The coherent light source has been described in chapter II.
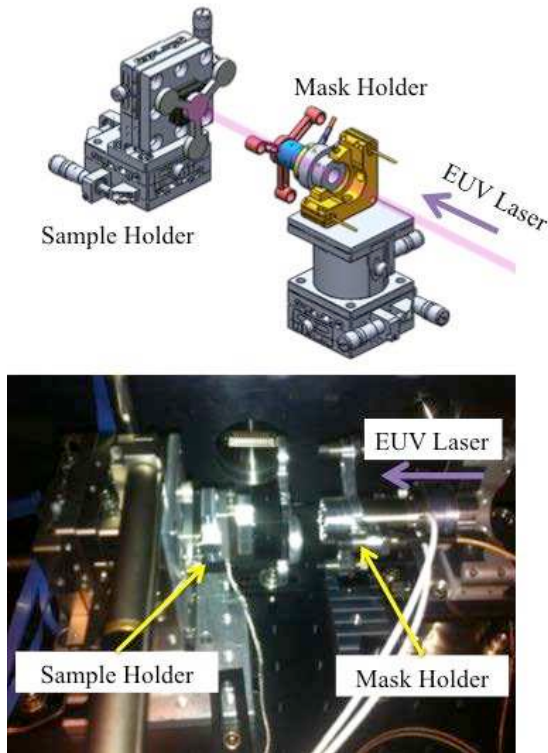
Figure 3.7: scheme and photograph of the exposure setup. A XYZ translation unit holds the sample that can be adjusted parallel to the Talbot mask with a tilt unit. The distances between mask and sample are controlled with three eddy current gauges with an accuracy of 50nm that allows control of parallelism within 10^{-4} rad.

The function of the positioning system is to accurately set the working distance (Z) between the mask and the wafer (Z is also called mask-wafer gap) at the Talbot distance within the DOF across the whole field of the mask. The diffractive Talbot mask was placed in the mask holder that allowed accurate longitudinal displacement and tilt in order to precisely adjust the distance and the parallelism between the mask and the sample. The sample is placed in the sample holder which is attached to a XY translation stage that displaces the sample in the plane parallel to the mask. It is actuated by stepper motors with 1µm accuracy from Thorlabs Inc. (Z812). Between the translation stage and the sample holder, linear positioners (SLC-2430) from SmaAct Gmbh were used for the fine control of the relative position between mask and sample. These positioners offer a positioning resolution as small as 1nm using a closed-loop control. The

lateral positioning stage allows stitching several fields to generate patterns with larger area, printing several fields in the same substrate or alternatively implementing double exposure to effectively reduce the minimum feature size or critical dimension (CD) as will be explained in section 3.8.

The tilt unit in the mask holder was implemented with three individual piezo actuators from Physik Instrument (S316) capable of adjusting the parallelism and the working distance (Z) with sub-10nm resolution using a closed loop control.

Three eddy gauges measure the mask-wafer gap (Z) with an accuracy of 50nm that assures a parallelism between the two surfaces within 10^{-4} rad. This multi-axis station provides a precise alignment to generate adequate prints in the samples. The required accuracy in the distance between the mask and the sample is determined by the DOF defined in the previous section and is determined by the mask design. The required parallelism accuracy or tilt precision Δ is defined by the DOF and the size of the mask (2W) and can be estimated as $\Delta = \sin^{-1}\left(\frac{\text{DOF}}{2\text{W}}\right)$.

3.4 FABRICATION OF DIFFRACTIVE EUV RETICLE

Because of the strong resonant absorptions in the EUV region for all materials, EUV lithography has been limited to use only transmission or reflective reticles schematically shown in Figure 3.8.

The semiconductor industry has adopted reflective reticles based on multilayers interference coatings. However, for GTI that has a working distance in the region of millimeters, reflective reticles are not adequate. This is why transmission EUV masks which are cheaper and more compatible for Talbot lithography were adopted in this work.
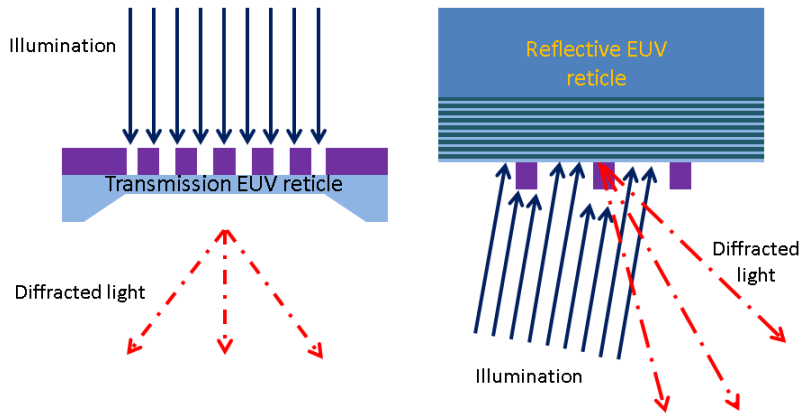
Figure 3.8: Transmission and reflective EUV reticle

This section is focused on describing the mask fabrication protocol for EUV Talbot lithography. Two different types of masks, silicon membrane supported and free-standing masks were utilized in this work and they are shown in Figure 3.9 (a) and (b) correspondingly. The nanofeatures on the masks were defined by electron beam lithography (EBL) that has been discussed previously in Chapter I.
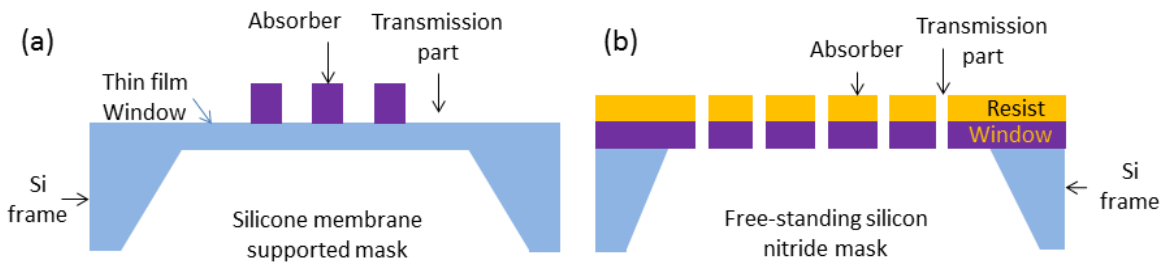
Figure 3.9: Silicon membrane supported masks and free standing silicon nitride masks

Transmission diffractive reticles can be implemented with phase reticles or amplitude (or intensity) binary reticles. Phase reticles have higher throughput but are more difficult to fabricate. All the diffractive EUV reticles used in this work were binary amplitude reticles. The reticle (or Talbot mask) was formed by transparent regions and absorbing regions with a sufficient contrast to assure an efficient diffraction. Two kinds of diffractive EUV reticles have

been designed and are schematically shown in Figure 3.9. Both types of reticles are fabricated on a thin transparent silicon nitride or silicon membrane defined in a silicon frame. The membrane needs to be thin enough to be transparent to EUV light yet it has to be sturdy to withstand the fabrication process that includes spin coating of the photoresist, development and plasma etching. Typically, the membrane used for diffractive EUV mask has a thickness from 50nm to 200nm depending on the design and material.

For silicon membrane supported masks, the transmissive regions are 100nm silicon thin film (shown as blue surface in Figure 3.9(a)). This thickness of Si assures 61% transmission for 46.9nm illumination[7]. The absorbing regions (shown as purple block in Figure 3.9(a)) are 100nm thick Hydrogen silsesquioxane (HSQ). This photoresist, when activated, becomes a material that has similar optical properties as silicon dioxide, providing a 10^{-3} transmission at the wavelength of 46.9nm [7].

For free-standing silicon nitride masks, the supporting structure is a 50nm silicon nitride membrane (shown in purple in Figure 3.9(b)). The binary mask is defined by etching through the membrane using a CF_4 plasma etcher. The transparent part is an opening through the membrane that provides 100% transmission to EUV light. The absorber for the free-standing silicon nitride mask, shown in yellow blocks in Figure 3.9 (b), is carbon a based photoresist ZEP520 (around 100nm in thickness after etching process) which has a transmission in order of 10^{-3}.

Figure 3.10 shows the scheme of the fabrication protocol. The membrane is first attached to a silicon wafer using strips of thermal release wafer dicing tape (Nitto-Denko 3195M). The dicing tape has a strong adhesive strength at room temperature (3N/20mm). After being heated up to 100°C, the adhesive strength goes to near zero and the sample can be easily detached.

E-beam resist is then spin coated on top of the membrane which is attached to a silicon wafer by two strips of dicing tape. The membrane is then released from the silicon wafer after the spin-coating. The membrane with resist coated on top is then exposed using the e-beam writer tool to define the designed pattern. In this process the electron dose has to be precisely determined. Before the e-beam lithography step, it is necessary to perform a calibration experiment to optimize the electron dose. One of the typical experiments is presented in the Appendix II. After the lithography step the exposed sample is developed. For the silicon membrane supported masks, the fabrication is completed with this step. For free-standing silicon nitride masks, there is an additional step of reactive ion etching (RIE) to etch through the silicon nitride membrane and generate the through openings that are the transparent regions of the mask. High energy (around 500eV) ions are produced in vacuum by applying a strong RF (radio frequency) electromagnetic field to the electrode at around 13 MHz. The RF is applied to create plasma by oscillating the electric field and ionizing the gas molecules by stripping their electrons. These high energy ions are then used to bombard the surface of the target and react with it.

Part of the silicon nitride window (shown as purple blocks in Figure 3.9 (b)) that was not protected by the resist (shown as yellow blocks in Figure 3.9 (b)) is then etched through to complete the mask fabrication process.
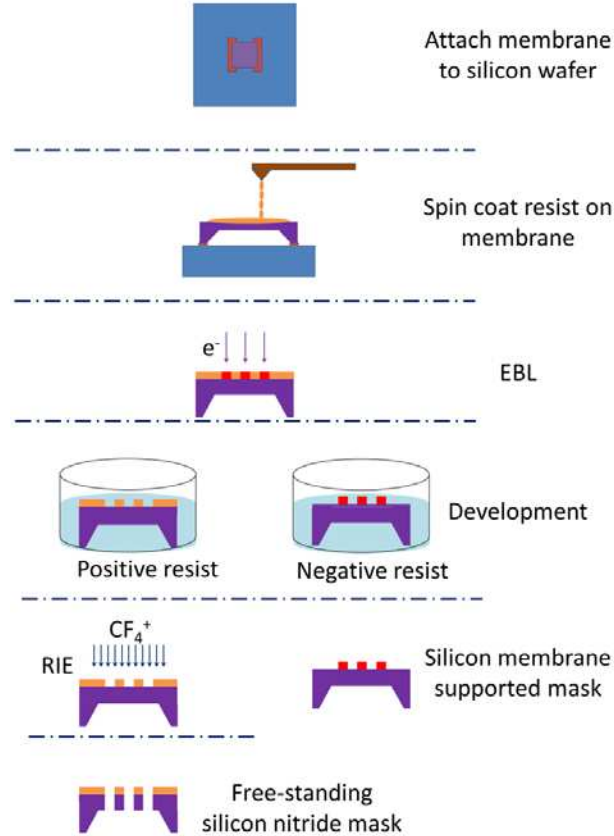
Figure 3.10: Scheme of fabrication protocol for diffractive EUV reticle

Selected scanning electron microscope (SEM) images of the fabricated EUV reticles are shown in Figure 3.11. Figures 3.11 (a) to (d) are free-standing EUV masks; (e) to (h) corresponds to silicon membrane supported masks. The specific parameters of each mask are indicated in the figure caption.

The characteristics of both types of reticles are summarized in Table 3.1. The contrast is defined as: $v = \frac{T_t - T_a}{T_t + T_a}$, where T_t and T_a are transmission of transparent part and absorbing parts. The efficiency (E) is defined as the transmission of transparent part. The advantage of free-standing silicon nitride mask is its 100% efficiency. However, since the free-standing nanostructure has no support underneath at all, it is intrinsically very fragile. The reticles can develop defects and those shown in Figure 3.11 (a) in the form of broken bridges. Self-standing

45

reticles are also limited to certain designs that can make the whole membrane still being connected. For example designs like pillars or annular rings cannot utilize this approach. On the other hand, silicon membrane supported masks have a 60% efficiency, but they are more versatile allowing any form of binary design within the limitations of the fabrication resolution.

Table 3.1: comparison between free-standing silicon nitride mask and silicon membrane supported mask

	Free-standing mask	Membrane supported mask
v	>99%	>99%
E	100%	61%
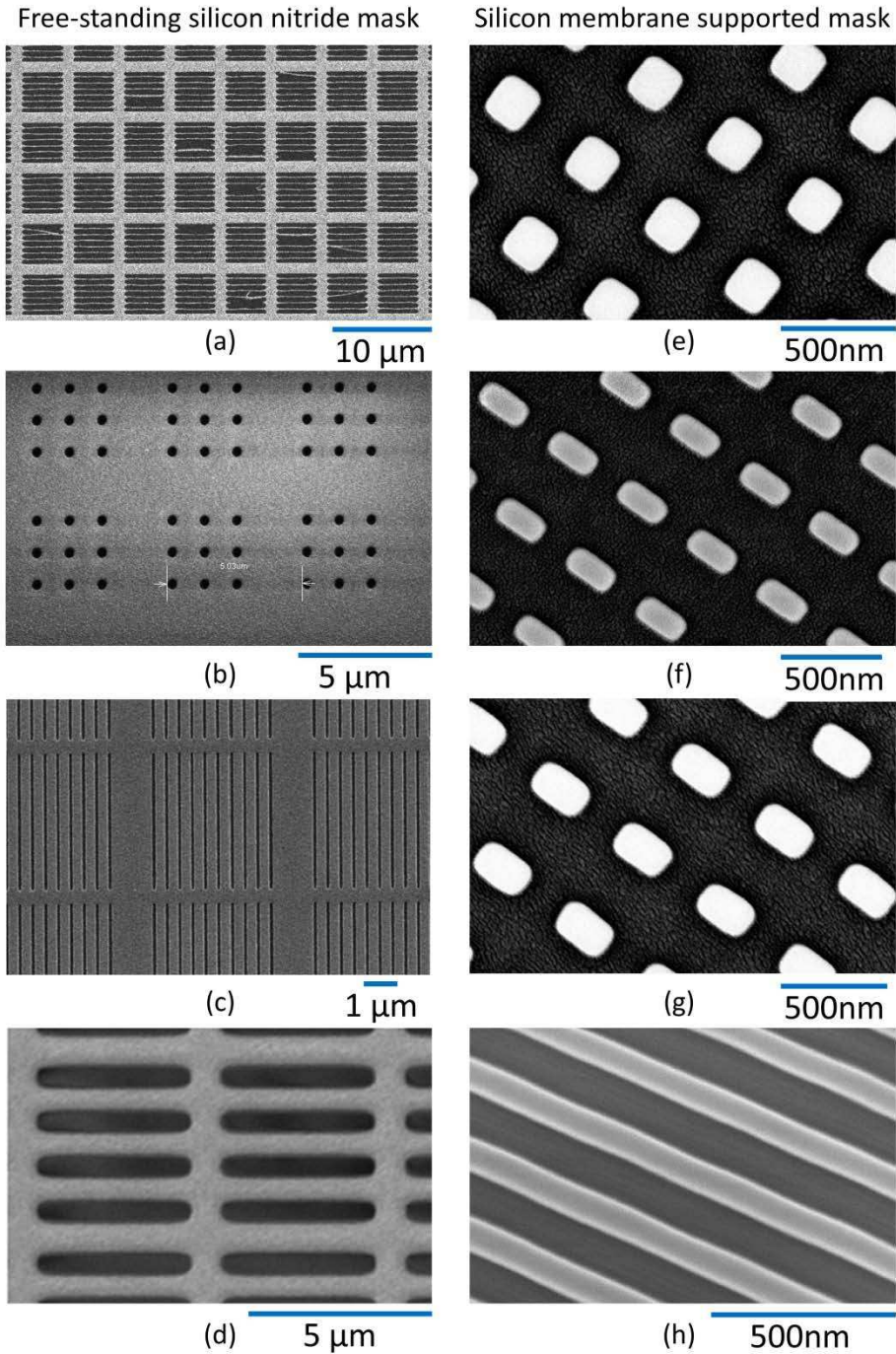
Figure 3.11: Fabricated diffractive EUV mask. (a) – (d) are free-standing EUV masks; (e) – (h) are silicon membrane supported masks. (a) is 500nm opening in 600nm pitch, the cell period is $5{\times}5\mu m^2$; (b) is 300nm holes with 1.2 μm pitch, the cell period is $5{\times}5\mu m^2$; (c) is 50 nm opening with 400nm pitch, the cell period is $5{\times}5\mu m^2$; (d) is 600nm half pitch gratings, the cell period is $5{\times}5\mu m^2$; (e) – (g) are metasurfaces designs which have $410{\times}410nm^2$ cell period; (h) is 100nm half pitch gratings

3.5   ION BEAM ETCHING (IBE) SYSTEM

The IBE system used in this project was developed and upgraded at Colorado State University[8] and is schematically shown in Figure 3.12. Ar plasma is created by flowing argon gas through a hollow cathode which is heated up to 1000°C using a 3kW current source. A directional argon ion beam is produced by accelerating Ar ions through a pair of accelerating grids. The ion beam is used to etch the target located on a sample holder. This system is capable to control the energy of the argon ion beam by changing the accelerating voltage up to 1000V. Also, as the ion beam is directional, the etching has a defined direction.   This is called anisotropic etching as opposed to isotropic etching like wet etching or RIE, which produces a noticeable undercut underneath the resist and reduces the accuracy of the pattern transfer.
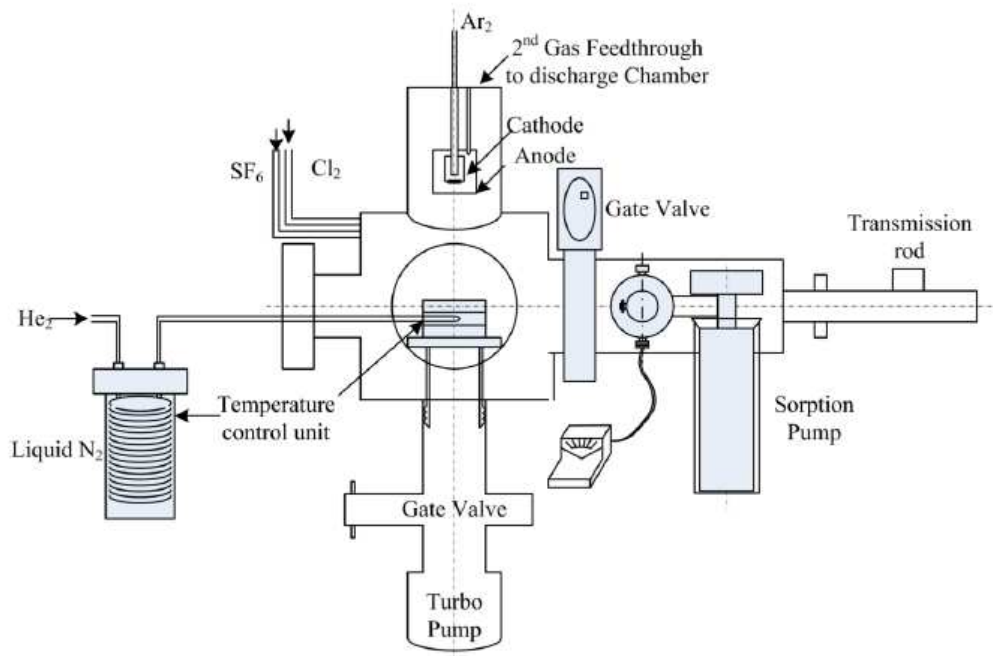

Figure 3.12[8]: Schematic of IBE system developed and upgraded in Colorado State University

IBE is a pattern transfer technique shown in Figure 3.13, which schematically describes this anisotropic etching process. Energetic argon ions bombard the sample surface which has a

48

sacrificial photoresist layer where the nanopatterns are defined. The homogeneous ion bombardment etches both the exposed areas of the target and the regions covered by the resist with different etching rates. The simultaneous etching process of both regions has the final effect to transfer the pattern from photoresist film into target metal film. Different materials have different etching rates. For instance, the etching rate for gold is 1nm/s when the discharge voltage is around 250 V. However, at the same etching conditions, the etching rate for exposed and developed HSQ is around 0.3nm/s. This relationship is what defines the aspect ratio (width/height) of the features that can be achieved with the process. For this particular example the aspect ratio of the nanopatterns generated in photoresist can be enlarged 3 times if HSQ is used as the hard sacrificial mask for the gold film.

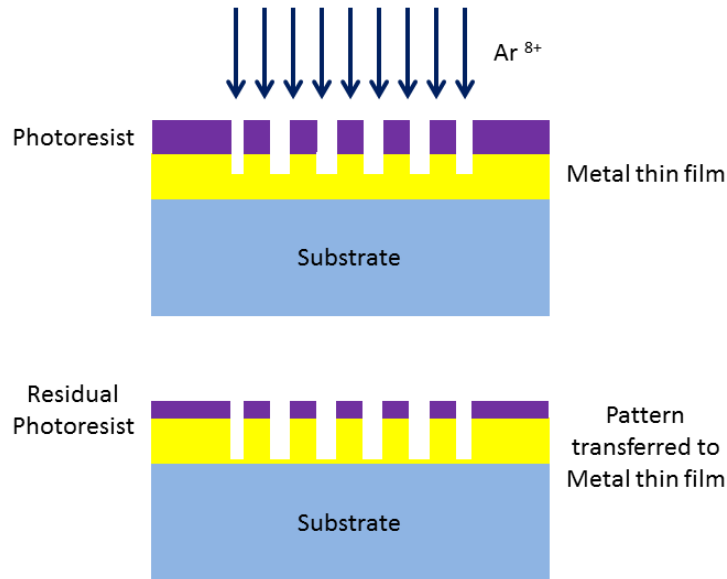Figure 3.13: Schematic of IBE process

However, while the target metal thin film is etched by the IBE process, it also increases the temperature of the sample's surface and might degrade the profile of the nanopatterns in the photoresist layer. In addition to this risk, the sputtering rate of the IBE is also temperature dependent. A fluctuating surface temperature will disturb the etching rate making the IBE

49

process unstable or unpredictable. A cryo cooling unit was introduced to address the problem of temperature fluctuation. By circulating helium through liquid nitrogen, the helium gas with low temperature and large heat conductivity flows underneath the sample holder which is maintained to a constant temperature of -100°C. The sputtering rate for photoresist decreases much faster with lower temperature than metals like silver or gold. Thus, the cryo cooling system increases the final aspect ratio of nanopatterns and stabilizes the etching rate to make the process more repeatable and reliable.

Another feature of the etching system is that the experiment chamber (10^{-7} torr) and the load-lock chamber (10^{-4} torr) are separated by a gate valve in order to maintain high vacuum in the chamber where the hollow cathode is located, preserving it from degradation due to the presence of oxygen. The load-lock system also ensures that the etching is performed using the same part of the ion beam for all the samples, increasing the repeatability of the process. A detailed operation list of the etching system is in Appendix III.

With the load-lock feature and the cryo cooling system, this upgraded IBE system has been able to transfer various nanopatterns faithfully from the resist layer to the metal films underneath. Selected nanofeatures etched into silver or gold thin films are shown in Figure 3.14 which are tilted SEM image. Figure 3.14 (a) is 500nm periodic or isolated lines etched into 100nm silver thin film. Figure 3.14 (b) are pillars (300nm in diameter) etched into 100nm gold thin film.
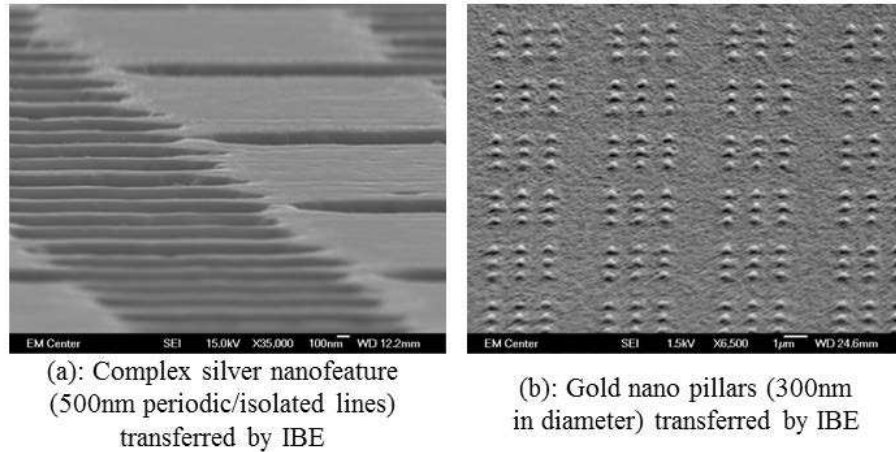
(a): Complex silver nanofeature
(500nm periodic/isolated lines)
transferred by IBE

(b): Gold nano pillars (300nm
in diameter) transferred by IBE

Figure 3.14 [9]: Pattern transfer by IBE. (a) is silver gratings and (b) is gold nano pillars.

3.6 DOSE CONTROL FOR EUV LITHOGRAPHY

The dose control is another essential aspect of the optical lithography system to control the size of the printed nanofeatures. Different doses will lead to different activation levels in the photoresist that will produce different pattern sizes even when the same reticle and imaging system have been used.

To address the issue of the variability with the dose, an in-line detector shown in Figure 3.15 was utilized to register the intensity of each EUV laser pulse. Figure 3.15(a) shows the in-line detector actually manufactured. It is constructed by two concentric metal tubes mounted inside the aluminum grounded case as depicted in Figure 3.15(b), which schematically illustrates the design and arrangement. The red cube is the aluminum ground case and the green tubes are the in-line detector. The inner tube is attached to a BNC cable which has a 1000V bias. The two cases are separated and supported by a Teflon piece visible as the white ring in Figure 3.15(a). The details of the two concentric tubes are illustrated in Figure 3.15 (d) which is the cross-section of the two tubes, BNC cable and the Teflon case which holds two tubes together. A hole is drilled on the grounded tube to let the BNC cable reach inside the inner tube and bias it at high

51

voltage. The Teflon pieces shown as the purple blocks in Figure 3.15(d) are design according to the inner diameter of the grounded tube and the outer diameter of the inner tube, so that both tubes are held tightly by the Teflon case and the aluminum ground case.

Figure 3.15 (c) depicts the external circuit used to detect the signal generated from in-line detector. A capacitor C=220pF is used to isolate the DC bias and protected the oscilloscope. The a set of resistors R_1=R_3 =40.1 Ω and R_2=10.1 Ω complete the circuit. R_1 and R_2 are used to convert the current signal from the in-line detector into a voltage signal which can be read by the oscilloscope. R_3 is used to limit the current in the oscilloscope.
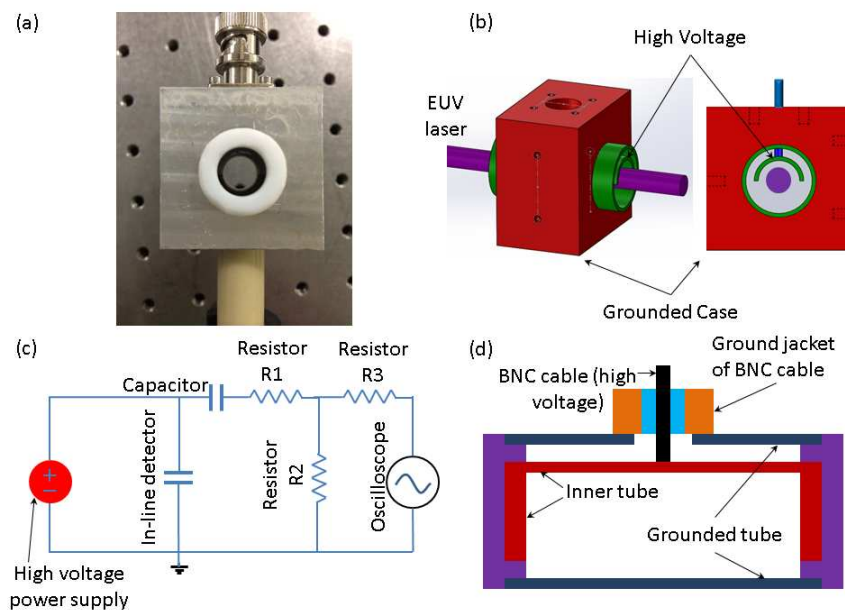
Figure 3.15: in-line detector for EUV laser intensity. (a) is the manufactured in-line detector; (b) is the schematic diagram for this in-line detector; (c) is the diagram for electric circuit to detect the signal from in-line detector

As schematically shown in Figure 3.15(c), the inner tube of the in-line detector is biased up to 1000V compared with the grounding case. When the EUV laser pulse (shown as purple cylinder in Figure 3.15(b)) passes through the detector, the background gas between the two concentric tubes absorbs the EUV light and the residual Ar gas is photoionized. The

photoionization produces ions and electrons and the electrons are accelerated towards the inner tube biased by 1000V. The created charges generated the in-line detector effectively acts as a current source which generated a pulsed signal. This current pulse creates a voltage difference in R_2 that is detected by the oscilloscope. The peak of this signal is representative of the intensity of the EUV laser.

A signal for a single shot EUV laser from this in-line detector is shown in Figure 3.16. Different intensities of the laser beam will lead to signals with different peak values. The internal capacitance and inductance of the in-line detector and the external circuit determines the sensitivity and the time response of the device.
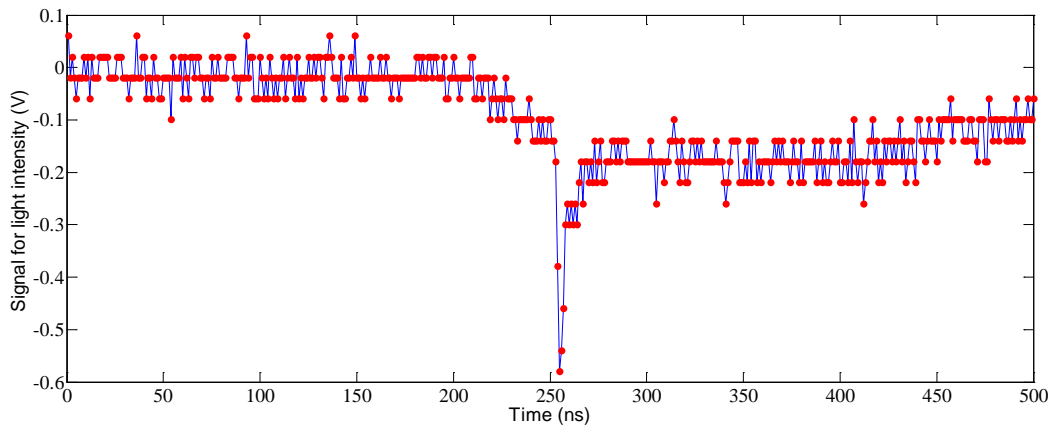
Figure 3.16: signal for laser intensity from the in-line detector

Along the beam path from the laser to the mask, 0.3% of the photons are absorbed by the background gas which has a 10^{-5} Torr pressure. The in-line detector does not introduce any additional absorption. It was only sampling the photoionization for each laser pulse which represents the pulse intensity given a stable background gas pressure.

The range of the voltage read from the oscilloscope (V_d) can be estimated by $\int \frac{V_d(t)}{R_2} dt = Q$. Where Q is the charges collected by the in-line detector from the photoionization process. The

53

charge Q can be estimated by the absorption rate (A=0.003% [7]) and the laser pulse energy (W=0.8mJ). Q=N×e, where N is the number of photon absorbed and e is the charge of the electron. N=A×W/p, where W is the laser pulse energy and p is the energy per photon (p=26.4eV).

Substitute all together, Q≈10^{-9}C. Assuming that the shape of the signal pulse is a triangle and the FWHM of the pulse is around 10ns (as shown in Figure 3.16), The peak value of $V_d(t)$ should be around -1V. Since the laser pulse energy is varying, the detected peak value of $V_d(t)$ shall be in the range of -0.1 to -1 Volt. This corresponds to the signal collected and shown in Figure 3.16.

However, the in-line detector can also saturate. The saturation level is determined by the capacitance of the in-line detector and the external circuit. The photoionization process might create too many charges if the laser intensity is too large and the background gas pressure is even higher than 10^{-5} Torr. The in-line detector with limited capacitance won't be able to discharge all the electrons into the external circuit. This will lead to a saturated signal which cannot represent the laser intensity accurately.

To analyze this issue, the in-line detector was calibrated against a photodiode previously calibrated and the calibration results were obtained and indicated in Figure 3.17. The laser is guided through the in-line detector and then impinging on the calibrated photodiode. Each data point is obtained by comparing signals from the in-line detector and the photodiode, both of which shall respond linearly to the variation of laser pulse intensity. As shown in the figure, the in-line detector is accurate compared with the calibrated photo diode and it is not saturated if the reading is in the range of -0.1V to -1V.
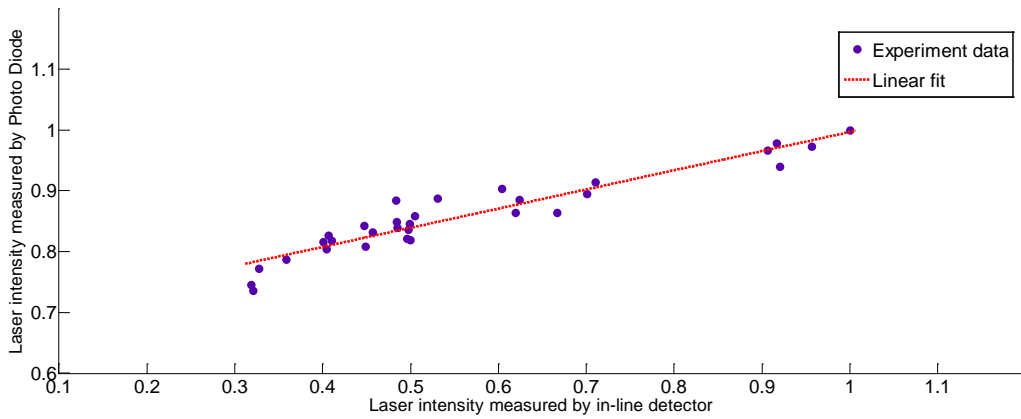
Figure 3.17: calibration for in-line detector using photo diode

By using the in-line detector as a dose control unit, the error for exposure dose can be limited to 1 shot. If a typical exposure for PMMA is 100 shots, in-line detector is able to control dose error within 1%.

3.7 FABRICATION OF METASURFACES USING UPGRADED TALBOT EUV LITHOGRAPHY.

This section will describe the fabrication protocol for metasurfaces using the Talbot lithography method presented previously. As engineered materials, metasurfaces have unique optical properties like negative index of refraction [10] and it can be widely applied to different area of research. For Talbot lithography, the challenging requirement to fabricate these nanofeatures is to achieve high resolution over large areas without defects. Figure 3.18 shows the design and fabrication protocol of a metasurfaces that is composed by periodic rectangular holes in gold thin film on top of a quartz substrate. The period of the rectangular holes is $410\times410\mu m^2$. The size of the rectangle is 180nm×190nm. The most challenging parts defining this structure are the corners which need to be as sharp as possible. The chamfer radius of the corner is required to be smaller than 50nm. Figure 3.19 (b) is the SEM micrograph of a diffractive mask with rectangular pillars fabricated by ebeam lithography. The mask was used in the Talbot lithography

55

setup using a negative tone photoresist rendering an array of rectangular holes in the photoresist. The photoresist pattern was then used as the hard sacrificial mask for the IBE process which transferred the nanopatterns onto the gold thin film underneath to complete the fabrication process.
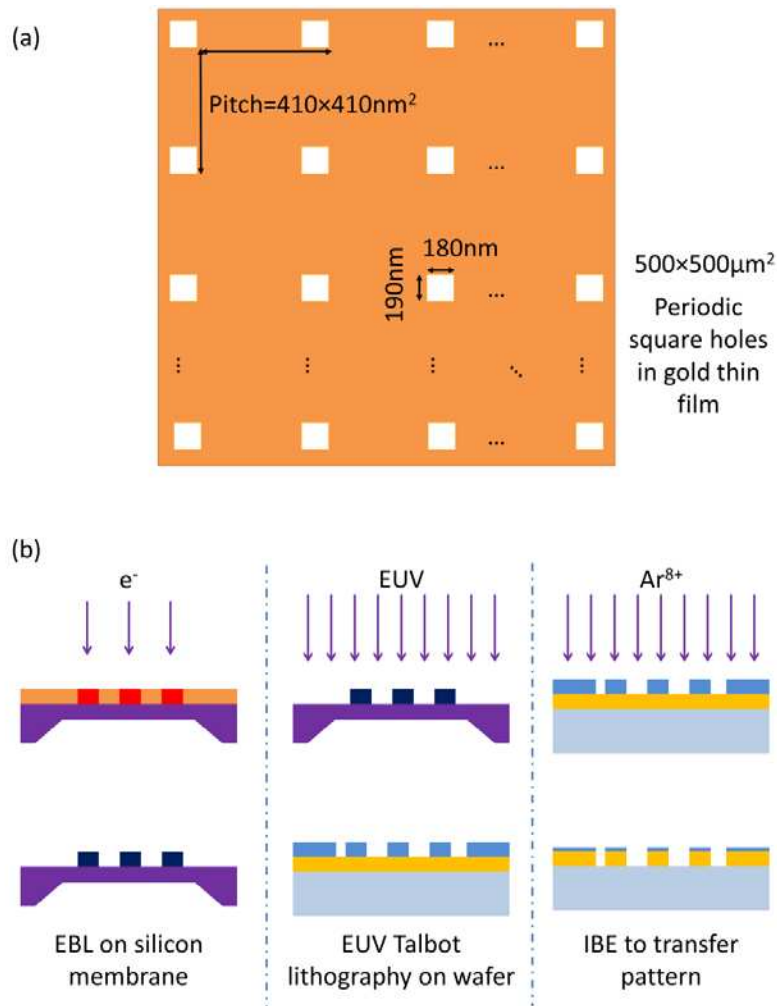
Figure 3.18: (a) is the schematic design of metasurfaces; (b) is the fabrication protocol

The patterns on the mask are defined by ebeam lithography. The state of art ebeam writer has a resolution as high as 6nm. However, the actual resolution of the ebeam lithography step is also limited by the electron scattering in the resist and substrate underneath which leads to a proximity effect. As shown in Figure 3.19[11], though the electrons are focused and confined

into one single point as indicated by the purple arrow, the directional electron beam can be scattered into much larger area after penetrating into the resist and the silicon wafer. The moving path of electrons after penetrating into the resist is shown as the black lines in Figure 3.19. This phenomenon which degrades the effective electron beam resolution is called proximity effect. The developed resist profile suffers significant variation from the original design. Typically a design of sharp corners will come out to be rounded up as shown in Figure 3.20.
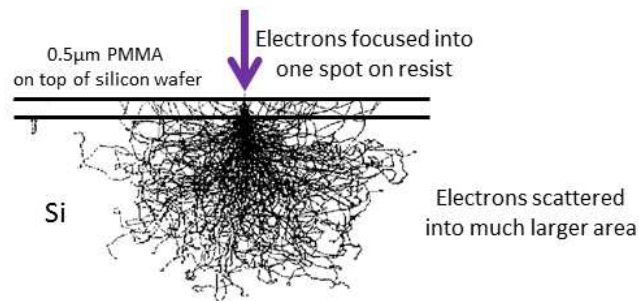
Figure 3.19[11]: proximity effect from electron back scattering in ebeam lithography

To correct the proximity effect, a point spread function (PSF), which simulates the electron moving path after penetrating into the resist, is used to address the issue of back scattering. This process is schematically shown in Figure 3.20. It first divided the whole exposure field in pixels. The size of each pixel depends on the pattern design. Then a Monte Carlo simulation is adopted. Monte Carlo simulation enumerative adjusts the dose on each "pixel" until the effective dose, which has taken back scattering into account using the PSF, is close enough to the original design. In this way, the dose map is changed from a uniform "single" dose everywhere to a modified "colorful" dose as schematically shown in Figure 3.20. Using this method which is also called proximity effect correction (PEC), the resolution at the corner of rectangular pillars is enhanced.
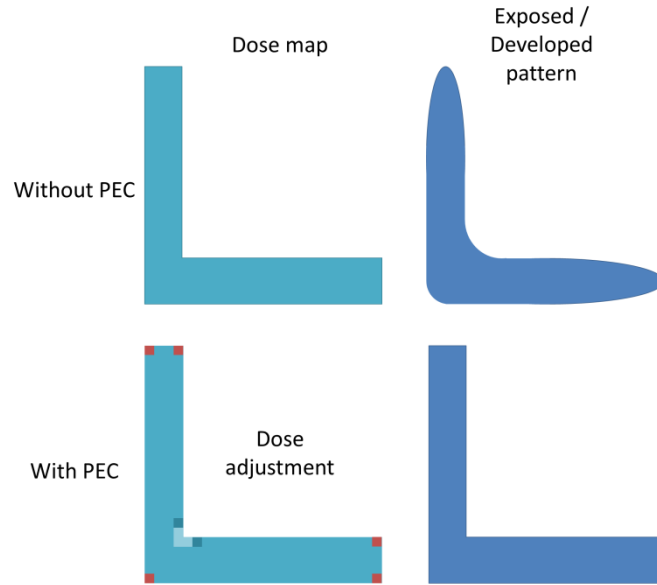
Figure 3.20: Schematic of proximity effect correction for ebeam lithography using point spread function.

With PSF enhancing the mask resolution, the chamfer radius of the rectangular pillars is limited to 20nm after development. A high resolution negative ebeam resist (MaN2401), was utilized to define the pattern on the mask. During the EBL process, $975\mu C/cm^2$ electrons are used to expose the resist under 200pA current. The exposed membrane was developed in Ma-D 532 for 10 seconds to form the designed nanopatterns.

In the EUV Talbot lithography step, high resolution EUV resist (HSQ) was used to define the rectangular holes. 40 shots of the EUV laser corresponding to a dose of $17.6mJ/cm^2$ was delivered to the HSQ layer, which is finally developed in tetramethyl-ammonium hydroxide (TMAH) for 10 seconds to complete the lithography process.

The comparison between the mask fabricated by EBL and the metasurfaces fabricated by EUV Talbot lithography was characterized by SEM inspection and is shown in Figure 3.21. Figure 3.21(a) shows the mask based on a silicon membrane which has $180\times190nm^2$ pillars (white rectangle). The pillars are arranged into $410\times410nm^2$ square lattice. Figure 3.21(b) shows

58

the lithography results that have been transferred into a gold thin film. From these SEM images, the resolution requirement was met both in the mask fabrication and the EUV Talbot lithography across the whole field.
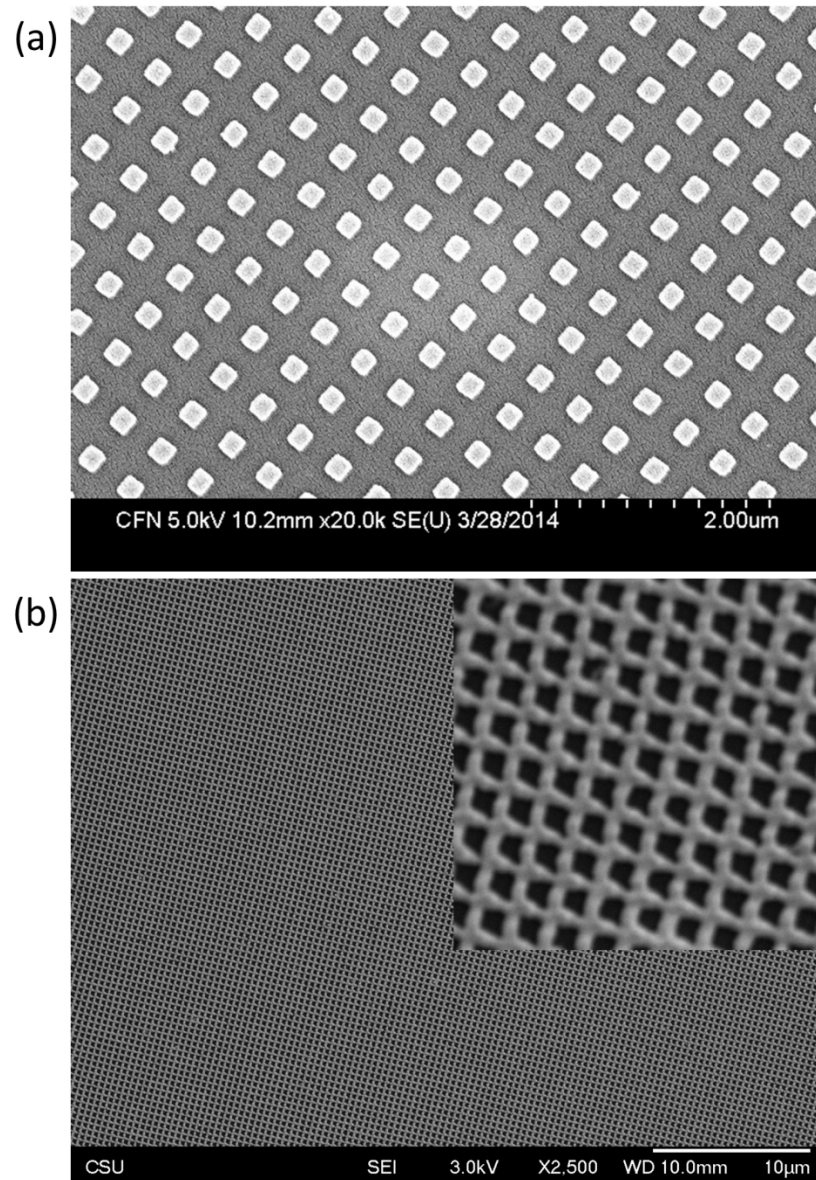

Figure 3.21: SEM results of EBL and EUV Talbot lithography for metasurfaces. (a) is the mask with rectangular pillars on silicon membrane; (b) is the lithography results using negative resist, the black part is the rectangular hole $(180 \times 190 nm^2)$ in gold thin film.

3.8 REDUCTION OF THE CRITICAL DIMENSION BY MULTIPLE EXPOSURES

Multiple exposures can be used to shrink the critical dimension (CD) of the printed pattern compared with the one on the mask. The process of multiple exposures is shown in Figure 3.22. The wafer is first exposed with half of the necessary dose to fully activate the photoresist using EUV Talbot lithography setup. After this first exposure with half of the dose, the sample is moved along a desired direction and exposed again with the other half of the dose. In the case shown in Figure 3.22, the wafer is moved a distance Δd along the X axis or in the direction perpendicular to the printed lines. The combined image between these two exposures will render a smaller CD using an optimized exposure dose. On the right part of Figure 3.22, the 1D profile represents the cut of the 2D Talbot images with pseudo color on the left. Compared the combined image with the original one, by adopting multiple exposures, the full width half maximal (FWHM) of the final image is reduced. Thus the processing window for dose control is larger.
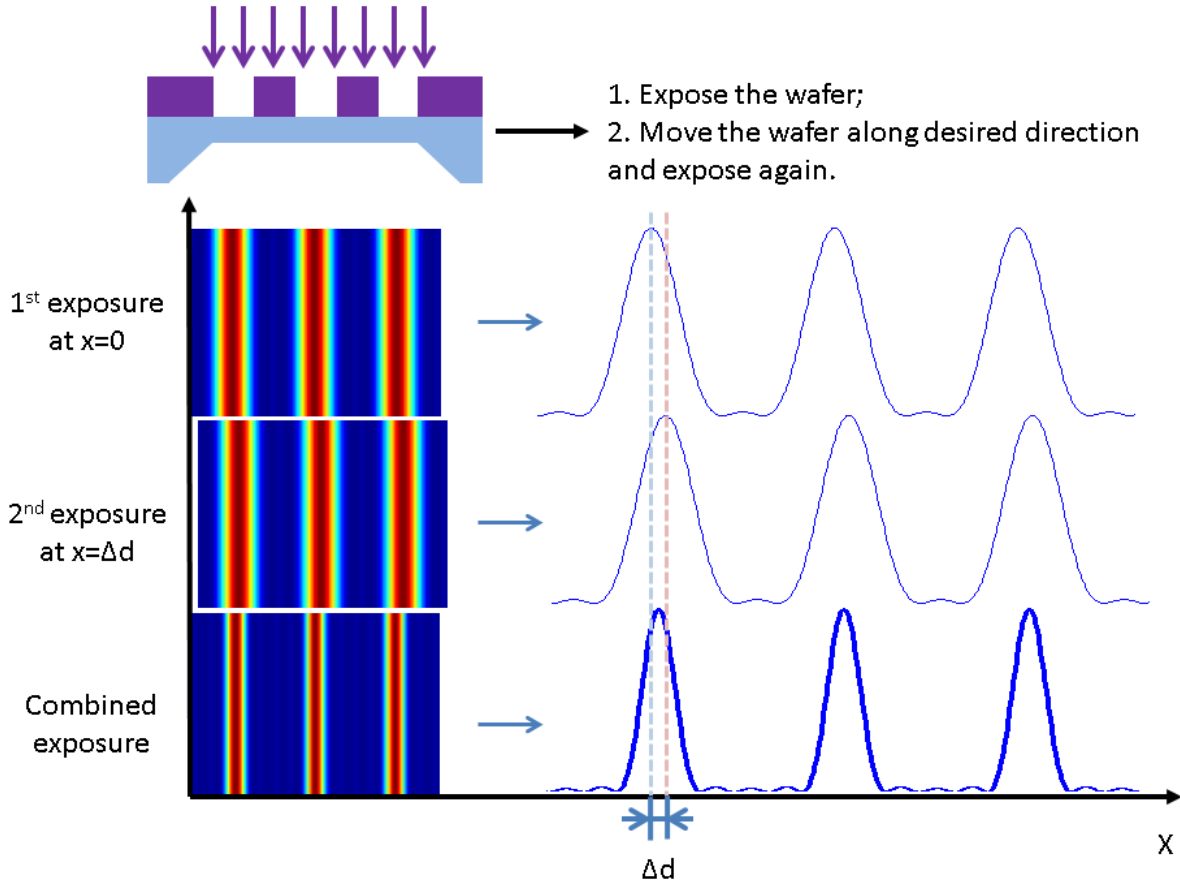
Figure 3.22: schematic of multiple exposures

This method has been published [12] and the results are shown in Figure 3.23. Figure 3.23 (a) and (b) are free-standing EUV masks which have 180×180 cells with a period of 2.85×2.85µm2. Inside each cell, Figure 3.23(a) has 100nm opening slits with 200nm pitch and Figure 3.23(b) has 75nm opening slits with 150nm pitch. The tiles have 40nm supporting bridges along the direction of the slits to strengthen the free-standing structure. Since the resolution calculated is 39nm, these supporting bridges won't be printed with Talbot lithography. Figure 3.23(c) and (d) are the lithography results obtained using the masks Figure 3.23(a) and (b) correspondingly. After a first exposure with half the dose (30 laser shots), the wafer was displaced in the direction perpendicular to the slits and another 30 shots exposure was delivered.

The offset between two exposures is Δd=50nm. Multiple exposures effectively decrease the CD on the wafer comparing with the mask.
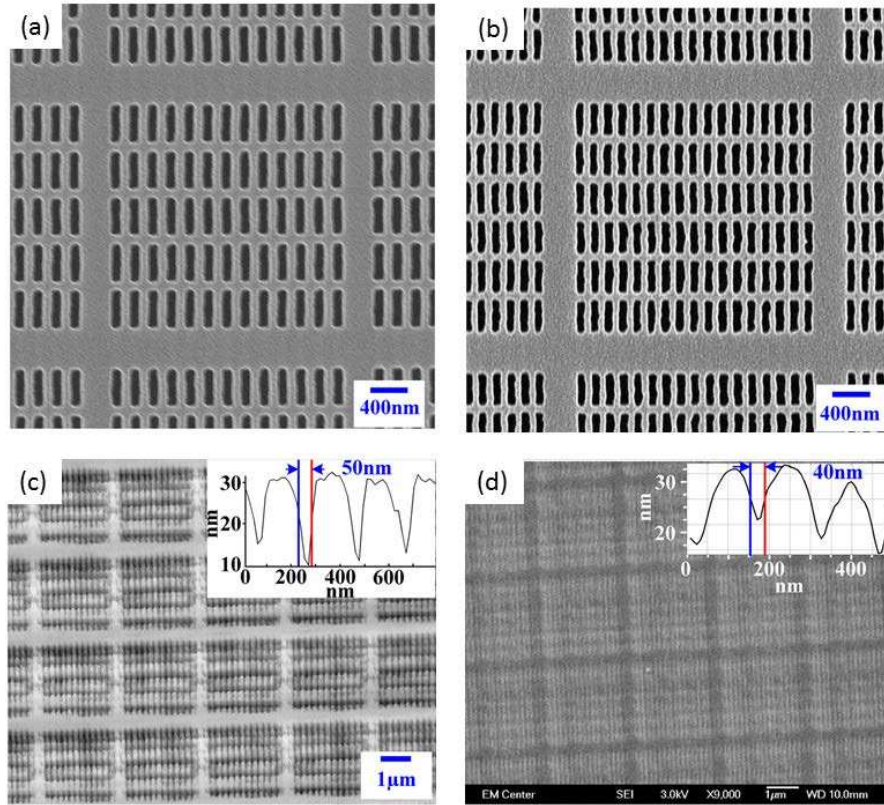
Figure 3.23[12]: experiment results for multiple exposures. (a) and (b) are the EUV masks with 100nm half pitch lines and 75nm half pitch lines; (c) and (d) are the lithography results based on multiple exposures using (a) and (b) accordingly. Δd=50nm in both cases

3.9   DISPLACEMENT TALBOT LITHOGRAPHY (DTL)

A scheme of the general idea of the DTL technique is shown in Figure 3.24. Instead of exposing the wafer maintaining a constant distance between the sample and the mask, DTL expose the wafer dynamically. The wafer is continuously moved along the normal direction of the mask, rendering a combined image which is the integration of the diffracted light over the whole Talbot distance Z_t. As can be seen in the Talbot carpet shown in Figure 3.24, the diffracted

light is periodic along the direction of illumination (defined as Z axis). By continuously exposing the wafer from d to $d+Z_t$ along Z axis, DTL integrates a periodic light distribution in depth (Z axis). This means that the DOF for DTL is infinite as it can start from anywhere (d) along the Z axis. This exposure method relaxes the demands on absolute mask-wafer gap control and enables high-resolution lithography using positioning system with relative low cost.

Regarding to the resolution of DTL, the combined image catches not only the original self-assembled image generated at the even Talbot planes ($Z=n{\times}Z_t$), but also the π shifted self-image generated at the odd Talbot plane ($Z = \frac{2n-1}{2} \times Z_t$). In this way, the spatial frequency of the final image is double the frequency of the pattern on the mask that has been utilized. This method has been introduced by H. Solak [13] and the work presented here is the demonstration in the EUV region.
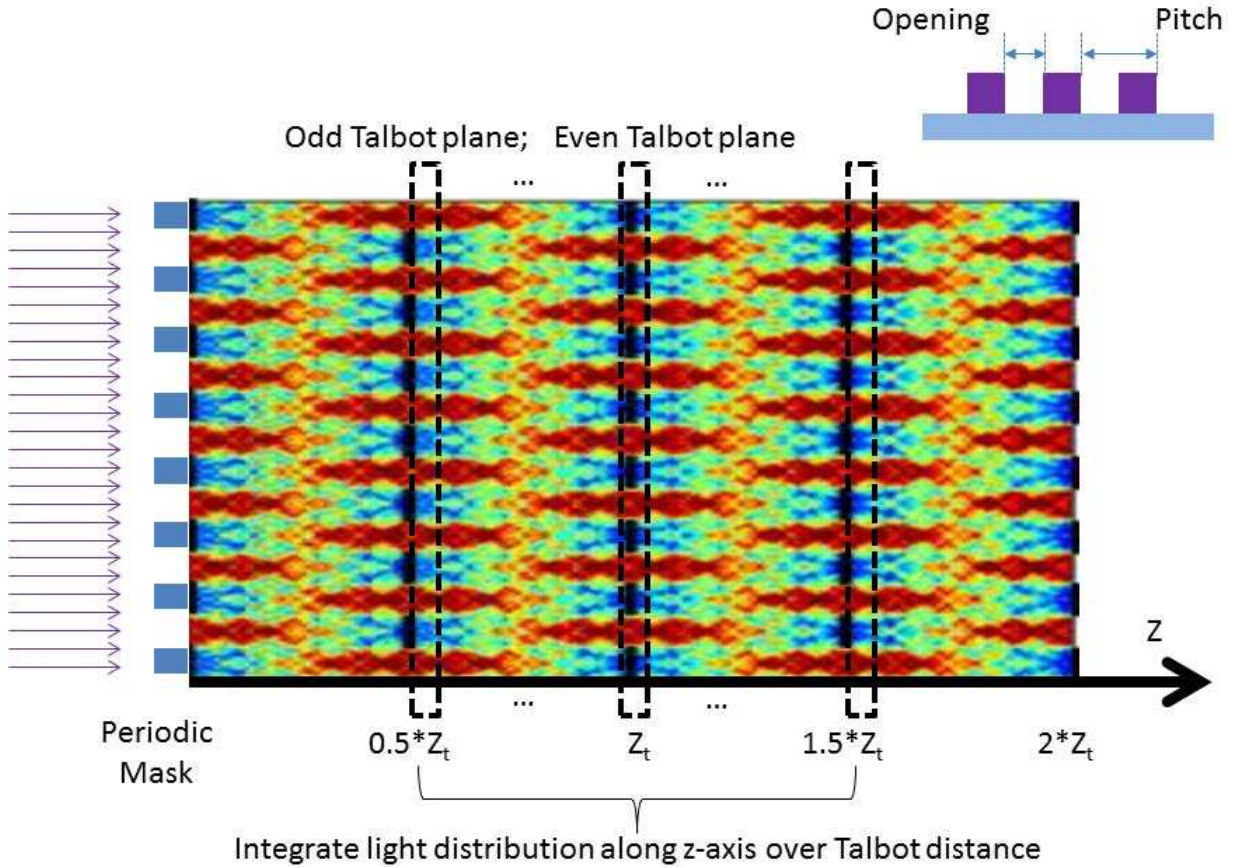
Figure 3.24: Schematic of DTL. To illustrate the effect of doubling spacial frequency, this diagram starts from 0.5 Zt to 1.5 Zt. But it is not limited to this starting point. As long as the displacement is Talbot distance, the integrated light will be the same.

Figure 3.25 shows results of a grating fabricated with this approach using the capillary discharge EUV laser. Figure 3.25 (a) is a SEM micrograph of the mask. It consists of lines with a period 200nm and a duty cycle of 50%. Where duty cycle is defined by opening/pitch. Figure 3.25 (b) is an AFM scan of the print produced by displacing the sample along the propagation axis over one Talbot distance while exposing. The photoresist used in this experiment is a positive photoresist from JSR Corp.[14]. The dose used in total is 100 shots that have been distributed evenly along with the displacement. The grating generated has a period that is half the period of the mask. The lineout section of the sample across the printed lines is depicted in

Figure 3.25 (c). The period of the structure is 100nm, from a 200nm grating shown in Figure 3.25 (a).
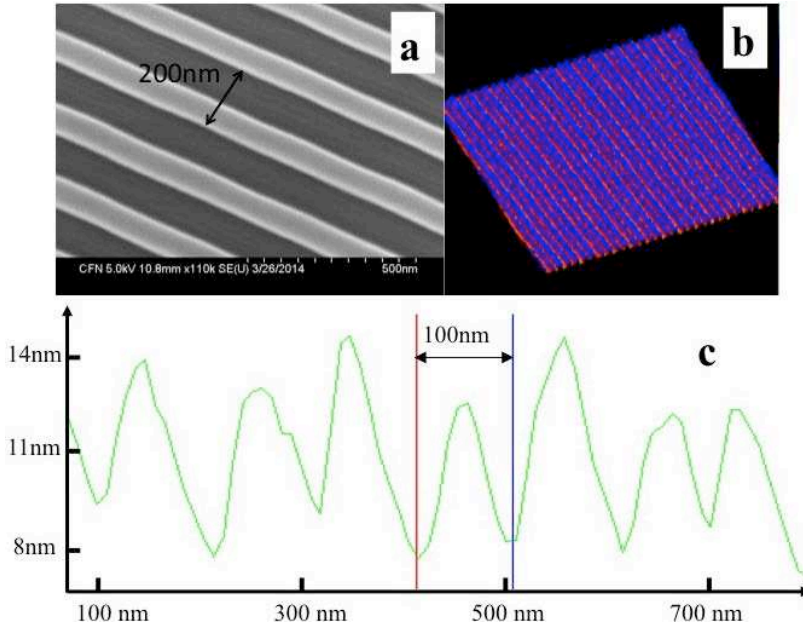
Figure 3.25: Experiment results for DTL. (a) is the 100nm half pitch grating fabricated using EBL as mask for DTL. (b) and (c) are the atomic force microscope (AFM) images for gratings fabricated on wafer by DTL. (b) is a 3D illustration and (c) is the cross-section.

However, DTL is criticized for the low contrast of the integrated image [15] which typically is around 0.3~0.5. By integrating the light distribution in depth, DTL adds too much light intensity to the region where shouldn't be exposed at all. This will reduce the resolution of the pattern in the developed photoresist.

As a conclusion, DTL is able to increase the spatial frequency compared to the mask without restrictions in the DOF. Using this technique, high resolution dense gratings can be fabricated without a demanding translation stage for mask-wafer gap control. However, the process window for dose control using DTL is very narrow in order to obtain a high contrast image. Also, DTL is limited to simple patterns like gratings and two-dimensional holes/pillars.

3.10 FRACTIONAL TALBOT LITHOGRAPHY (FTL)

In this section, fractional Talbot lithography (FTL) is investigated. FTL is a scalable Talbot lithography technique capable of increasing the spatial frequency of the print on the wafer relative to the frequency of the Talbot mask. This fabrication method is schematically shown in Figure 3.27[16]. Figure 3.27(a) is the Talbot carpet of a mask with 500nm opening and 3µm period. Figure 3.27(b) is the one-dimensional profile of diffracted light at so-called fractional Talbot distances, passing through the mask shown in Figure 3.27(a). Not only at integer multiples of Talbot distance (Z_t), diffraction pattern at fractional Talbot distance (Z_{sf}) also renders an image of the mask with high contrast which is called fractional Talbot image. Fractional Talbot distance is defined as: $Z_{sf} = (N + \frac{p}{q}) \times \frac{Z_t}{2}$. Where, p and q are co-prime numbers, $p<q$ and N is an integer. In addition, the spacial frequency of the image at the fractional Talbot distances is scaled by a factor of $M_{sf} = q$.

Scaling factor M_{sf} is illustrated as follows:

M_{sf}= 1 when p=1, q=1;

M_{sf}= 2 when p=1, q=2;

M_{sf}= 3 when p=1 or 2, q=3;

M_{sf}= 4 when p=1 or 3, q=4;

M_{sf}= 5 when p=1, 2, 3 or 4, q=5;

…
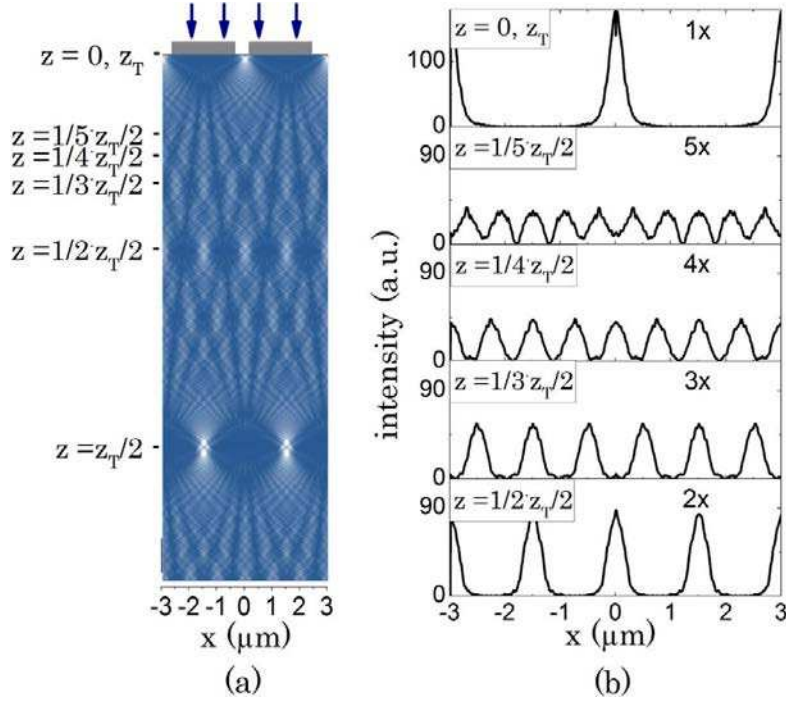
Figure 3.26[16]: Schematic of FTL. (a) is the Talbot carpet of a Talbot mask with 500nm opening and 3µm period; (b) is the one-dimensional cross section of the diffracted light at fractions of Talbot distance.

However, FTL with the spatial frequency multiplication effect has sacrificed the contrast and the DOF of the fractional Talbot image in comparison with the original and π shift Talbot image. The reduction of contrast is shown in Figure 3.27(b) which has illustrated that higher M_{sf} leads to smaller contrast.

The DOF of FTL is estimated as: $DOF = \frac{p^2}{2\lambda(M_{sf}^2 - 1)}$ [16]. Where p is the pitch of gratings. From this equation, the DOF of FTL is decreasing with higher scaling factors. This negative relation can also be estimated virtually from the Talbot carpet shown in Figure 3.27(a).
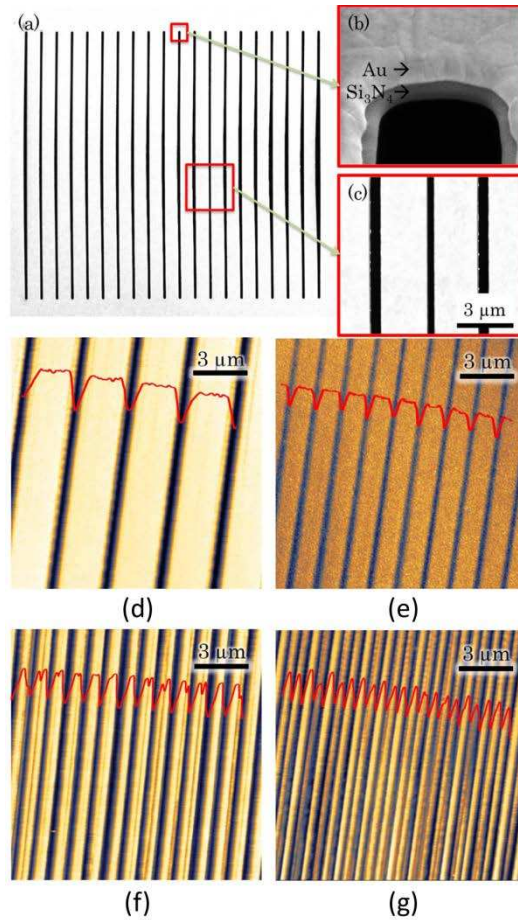
Figure 3.27[16]: Experiment results of FTL using 46.9nm EUV laser. (a)-(c) are the free standing Talbot masks made by focused ion beams. (b) and (c) are zooming SEM figures of (a); (d) –(g) are FTL results with M_{sf} = 1, 2, 3 and 5.

To illustrate the feasibility of this idea, gratings fabricated for FTL were examined. Figure 3.28 depicts the SEM images of the printed gratings at the different fractional Talbot planes [16] . Figure 3.28 (a)-(c) are free standing gratings with 500nm opening and 3µm period. The free standing mask was made by focused ion beam milling on top of gold thin film and silicon nitride membrane. They are manufactured by H. Kim from Aachen University in Germany. The photoresist used in this test was polymethyl methacrylate (PMMA). FTL was conducted and the results are shown from Figure 3.28 (d)-(g) that has an M_{sf} equals to 1, 2, 3 and 5 correspondingly.

In conclusion, using EUV FTL, spatial frequency multiplications up to 5× were achieved with pitches of 3μm, 1.5μm, 1μm, and 600nm, from the master grating with 3μm pitch.

3.11 18.9NM EUV TALBOT LITHOGRAPHY

This section describes the demonstration of Talbot lithography using a 18.9nm EUV laser [17]. The achievable resolution of EUV Talbot lithography will be enhanced by using an illumination with smaller wavelength as the pitch resolution is linear with the wavelength of the light source used (s=λ/NA).

The schematic of EUV Talbot lithography using 18.9nm laser is shown in Figure 3.29. The 18.9nm ASE laser was presented in Chapter II. This laser beam was first filtered by a 100nm aluminum filter which blocks out the UV and visible background light[18]. Then the filtered EUV light is reflected and guided by a multilayer mirror (Mo/Si) towards the free standing Talbot mask. The multilayer mirror keeps filtering out background light due to the narrow bandwidth of its reflectivity curve which is centered at 18.9nm with bandwidth equals to $\frac{\Delta\lambda}{\lambda} \approx 0.06$ [19]. Note that the bandwidth of the reflectivity curve also depends on the incidence angle which is 45° in this experiment. At normal incidence angle, this value shall be even smaller. At a distance corresponding to Zt/2 behind the mask, a substrate coated with AZPN photoresist was placed to record the generated Talbot image. The print was obtained with an exposure of 30 s operating the laser at 50 Hz repetition rate. The dose is around 22.5mJ/cm^2. The exposed wafer was then developed in TMAH for 10 seconds.

The mask and the lithography results are shown in Figure 3.29 (b) and (c). The mask was composed of 10,000 unit cells arranged in a square matrix with a period p=5μm. Each cell consisted of 4 slits 500 nm width and 1.2 μm period. A scanning electron microscope (SEM)

69

scan of the mask is shown in Figure 3.29 (b). The overall size of the mask is $0.5 \times 0.5 \text{ mm}^2$, with a calculated first Talbot distance $Z_t = 2.65$ mm. The AFM image of the printed nanofeatures shown in Figure 3.29(c) is an accurate replica of the patterns on the Talbot mask.
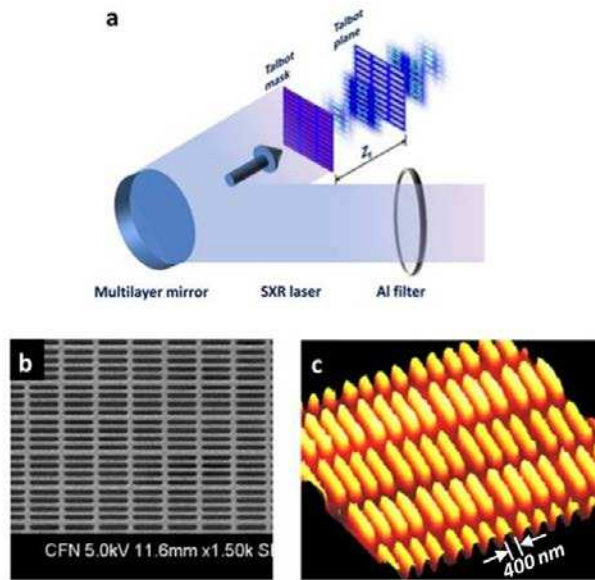
Figure 3.28[17]: experiment set up and results of Talbot lithography using 18.9nm laser. (a) is the experiment setup; (b) is the free standing Talbot mask used; (c) is the AFM image of the nanopatterns on the wafer printed by 18.9nm laser and mask shown in (b).

In conclusion, Talbot lithography using sub-20nm illumination was demonstrated in this section. The high photon flux EUV lasers have expanded the application of Talbot lithography to a new stage that sub 20nm features might be possibly printed using a table-top set up in the future.

3.12 SUMMARY

This chapter presented the Talbot lithography method that was utilized to fabricate a series of complex periodic structures like gratings and plasmonic surfaces over large areas in a consistent manner.

Multiple exposures, DTL and FTL have been studied and characterized to keep pushing the resolution limit even beyond the scaling limitation of the wavelength. High resolution nanopatterns like 50nm half pitch gratings have been fabricated and demonstrated by combining EUV Talbot lithography and these resolution enhancement techniques. Finally, by adopting 18.9nm ASE laser, the potential to make sub-20nm features using Talbot lithography has been illustrated.

REFERENCE:

[1]   H. Talbot, "Facts relating to optical science," *Philos. Mag.*, vol. 9, p. 403, 1836.

[2]   C. Zanke, M. Qi, and H. I. Smith, "Large-area patterning for photonic crystals via coherent diffraction lithography," *J. Vac. Sci. Technol. B Microelectron. Nanom. Struct.*, vol. 22, no. 6, pp. 3352–3355, 2004.

[3]   J. W. Goodman, *Introduction to Fourier Optics*. 2005.

[4]   A. Poonawala and P. Milanfar, "Mask Design for Optical Microlithography a Inverse imaging problem," *IEEE Trans. image Process.*, vol. 16, no. 3, pp. 774–788, 2007.

[5]   D. Attwood, *Soft X-Rays and Extreme Ultraviolet Radiation*. Cambridge University Press.

[6]   S. Lipson and A. Lipson, *Optical Physics*, 4th ed. Cambridge University Press, 2010.

[7]   http://henke.lbl.gov/optical_constants/gastrn2.html.

[8]   Wei Li, "PERIODIC METALLIC NANOSTRUCTURES FABRICATED BY COHERENT TALBOT LITHOGRAPHY IN A TABLE TOP SYSTEM" , 2013.

[9]   R. Maas, J. Parsons, N. Engheta, and A. Polman, "Experimental realization of an epsilon-near-zero metamaterial at visible wavelengths," *Nat. Photonics*, vol. 7, no. 11, pp. 907–912, 2013.

[10]   L. Ren and B. Chen, "Proximity effect in electron beam lithography," in *Solid-State and Integrated Circuits Technology, 2004.*, 2004, pp. 579–582.

[11]   W. Li, V. M. Esquiroz, L. Urbanski, D. Patel, C. S. Menoni, M. C. Marconi, A. Stein, W. Chao, and E. H. Anderson, "Defect-free periodic structures using extreme ultraviolet Talbot lithography in a table-top system," *J. Vac. Sci. Technol. B Microelectron. Nanom. Struct.*, vol. 31, no. 6, p. 06F604, 2013.

[12]   H. H. Solak, C. Dais, and F. Clube, "Displacement Talbot lithography: a new method for high-resolution patterning of large areas.," *Opt. Express*, vol. 19, no. 11, pp. 10686–10691, 2011.

[13]   http://www.jsr.co.jp/jsr_e/pdf/pd/ec/next-g.pdf.

[14]   L. Stuerzebecher, F. Fuchs, U. D. Zeitner, and A. Tuennermann, "High-resolution proximity lithography for nano-optical components," *Microelectron. Eng.*, vol. 132, pp. 120–134, 2015.

[15]   H. Kim, W. Li, S. Danylyuk, W. S. Brocklesby, M. C. Marconi, and L. Juschkin, "Fractional Talbot lithography with extreme ultraviolet light," *Opt. Lett.*, vol. 39, no. 24, p. 6969, 2014.

[16]   B. A. Reagan, W. Li, L. Urbanski, K. A. Wernsing, C. Salsbury, C. Baumgarten, M. C. Marconi, C. S. Menoni, and J. J. Rocca, "Hour-long continuous operation of a tabletop soft x-ray laser at 50-100 Hz repetition rate," vol. 21, no. 23, pp. 1115–1117, 2013.

[17]   http://refractiveindex.info/?shelf=main&book=Al.

[18]   Y. C. Lim, T. Westerwalbesloh, A. Aschentrup, O. Wehmeyer, G. Haindl, and U. Heinzmann, "Fabrication and characterization of EUV multilayer mirrors optimized for small spectral reflection bandwidth," *Appl. Phys. A*, vol. 72, pp. 121–124, 2001.

CHAPTER 4 EXTREME ULTRAVIOLET TALBOT INTERFERENCE LITHOGRAPHY

4.1 INTRODUCTION TO A HYBRID LITHOGRAPHY TECHNIQUE

Restricted only by the wavelength of the illumination, Interference lithography (IL) has the advantages to print nanopatterns with high resolution using a relative unlimited DOF (restrained by beam size and spacial coherence). However, only simple periodic patterns like gratings and 2D arrays can be generated using this technique. To make functional nanopatterns like photonic crystal waveguide using IL, additional lithography process with high alignment accuracy is requested to modify the lattice.

Talbot lithography as has been discussed in Chapter III, is capable to fabricate arbitrary periodic patterns in a large area, liberating the lattice design so that complex periodic nanofeatures can be fabricated with this technique. However, the resolution of Talbot image is limited by the NA of imaging system and the accessibility of the high resolution mask with enough contrast. In addition, Talbot lithography suffers from a restricted DOF when patterns with high resolution is required, making the process unreliable.

This chapter describes a hybrid lithography technique which combines interference lithography and Talbot lithography. It is named as Talbot interference lithography (TIL). TIL is able to print complex structures in a single lithography step by modifying the lattice of interference patterns with custom designed Talbot masks. Two identical Talbot images generated from a single Talbot mask illuminated by two coherent EUV laser beams are superposed in a common Talbot plane. In this plane, interference between the two images generates a hybrid pattern from the combination of the interference and the Talbot image. TIL is able to fill

arbitrary shaped periodic cells produced by Talbot imaging with fine interference pattern. This technique relaxes the fabrication constrains on the mask and enlarges the DOF for the imaging system. Using a simple experiment setup, TIL is able to generate unique patterns with a combination of Talbot imaging and interference that results in a hybrid approach that has the advantages of both IL and TL methods. This chapter will present a description of the imaging system, a detailed mathematical modelling and experiment results. At the end of this chapter, a comprehensive analysis of the exclusive advantages using TIL will be presented.

4.2 MODELLING OF TIL

A schematic of TIL is depicted in Figure 4.1[1] where two mutually coherent beams impinges the semi-transparent Talbot mask with incidence angles $\pm$ θ. Each beam produces a Talbot image of the mask at the Nth Talbot plane with a mask-wafer gap $z=N*Z_t=N \times 2p^2/\lambda$, where Z_t is the Talbot distance, p is the period of the structure in the Talbot mask, N is the order of Talbot plane and λ is the wavelength of the illumination. At the common Talbot plane, the images produced by each one of the coherent beams coincide generating a modified interference pattern. This interference pattern is printed onto a photoresist coated wafer located at the image plane $z=N*Z_t$. For simplicity, let's define (ξ, η) as the mask plane, (x, y) as the image plane. Z is the axis normal to the mask plane. The wavevectors $\overrightarrow{k_{1,2}}$ are two coherent beams with incidence angle $\pm$ θ on (x, z) plane.

74
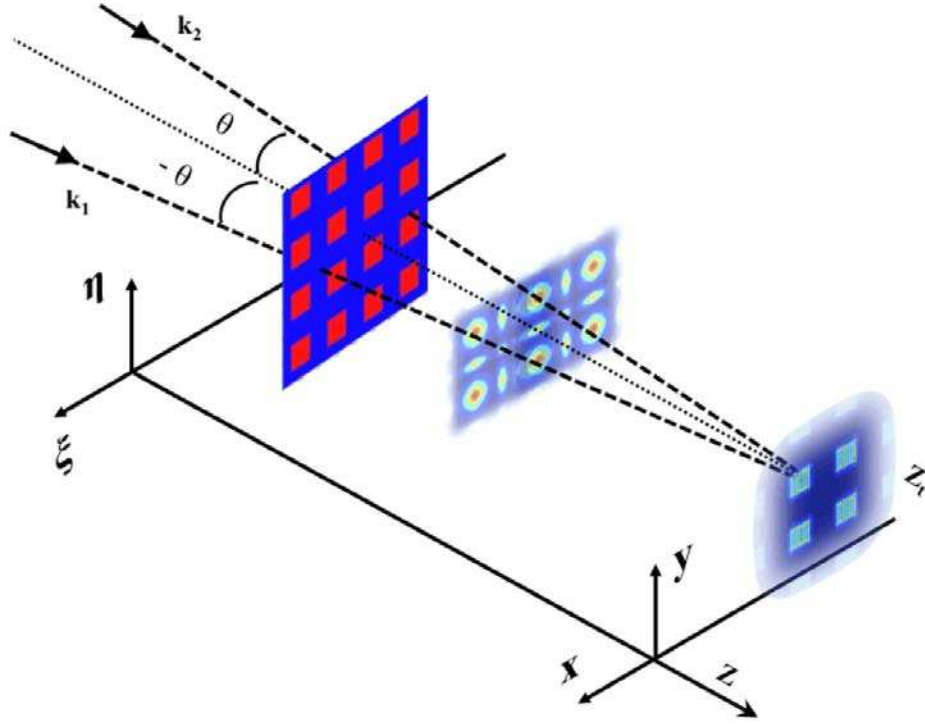
Figure 4.29[1]: Schematic of TIL

The electric field at the (x, y) plane can be calculated by diffraction theory[2]. Assuming a Talbot mask located at the (ξ, η) plane at $Z=0$ with a transmission defined by $t_A(\xi, \eta)$ is illuminated by two plane waves with incidence angle $\pm \theta$, each beam will generate an image at image the plane (x, y) at $Z=z$. This diffraction image can be computed by the Fresnel propagator as:

$$E_i(x, y) = \frac{e^{jkz}}{j\lambda z} \iint_{-\infty}^{+\infty} T_i(\xi, \eta) \exp\left\{\left[\frac{jk_i}{2z}(x - \xi)^2 + (y - \eta)^2)\right]\right\} d\xi d\eta \qquad 4\text{-}1$$

Where, $E_i(x, y)$ is the electric filed amplitude at the Talbot plane. The function $T_i(\xi, \eta)$ is defined as

$$T_i(\xi, \eta) = t_A(\xi, \eta) \cdot XPhase \cdot YPhase$$

where XPhase and YPhase are phase changes across the mask plane (ξ, η). They can be defined as,

$$XPhase = e^{-\{\frac{2\pi i}{\lambda}[\xi \cdot \cos(\theta_\xi)]\}}$$

$$YPhase = e^{-\{\frac{2\pi i}{\lambda}[\eta \cdot \cos(\theta_\eta)]\}}$$

If the propagation distance is equal to Talbot distance ($z=N \times Z_t$), the Talbot images are formed and coincide at the image plane (x, y). The superposition of the two Talbot images generated from two coherent beams will render a modified interference image which can be defined as:

$$I(x,y) = E_1^2(x,y,z) + E_2^2(x,y,z) + 2 \times U_{12} \times \cos((\vec{k_1} - \vec{k_2}) \cdot \vec{r}) \qquad \text{4-2}$$

Where $I(x,y)$ is the modified interference image. E_i is the electric field amplitude of each beam at the Talbot plane. U_{12} is the interference coefficient defined as $U_{12} = E_1 * E_2 * (\hat{e_1} \cdot \hat{e_2})$, where $\hat{e_1}$ and $\hat{e_2}$ are unit vectors that define the electric field directions in the Talbot plane. $\vec{k_{1,2}}$ are the wave vectors of the illumination.

To verify this theory and predict the Talbot interference image, a simulation based on equation 4-2 was performed using Matlab. A complete script of the code is attached in Appendix I. The simulation result is shown in Figure 4.2.[1]
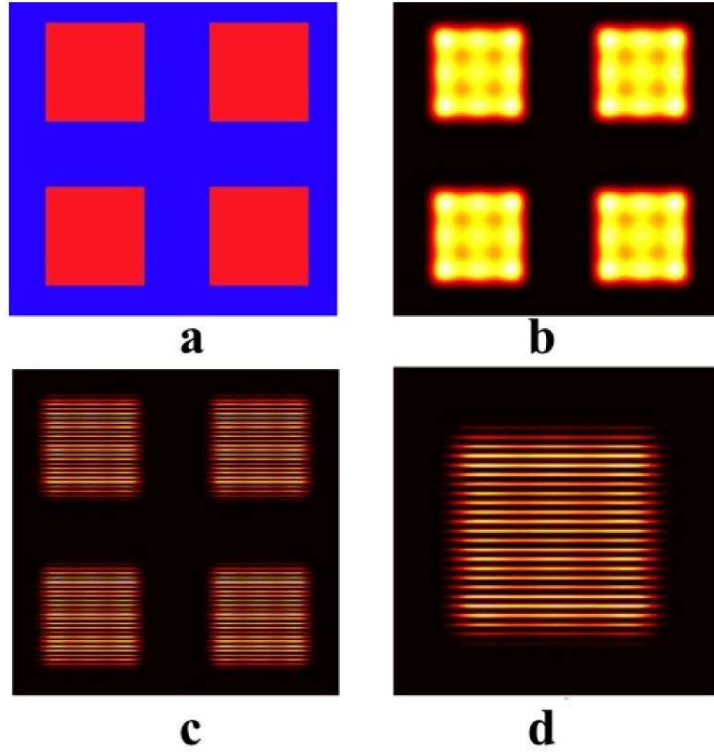
Figure 4.30[1]: Simulation results based on equation 4-2. (a) is the binary mask with 20×20 cells of 7.5×7.5µm^2 square holes in square lattice, the cell period is 12.5×12.5µm^2; (b) is the traditional Talbot image generated by one beam at normal incidence; (c) is the TIL image generated by superposing two coherent Talbot images using 46.9nm illumination with incidence angel equal to ±4°; (d) is a zoom of one cell in (c).

Figure 4.2(a) shows the Talbot mask which has 20×20 cells of square holes arranged in a square lattice. The size of the holes is 7.5×7.5µm^2 and the period 12.5×12.5µm^2. This array of square holes constitutes a binary mask with a transmission $t_A(\xi, \eta)$. The periodic mask is illuminated by two coherent plane waves (λ=46.9nm) with incidence angle θ_1=4° and θ_2=-4°. At the common image plane (2nd Talbot plane Z=2×Z$_t$), two identical Talbot images interfere with each other creating a Talbot interference image defined by equation 4-2. The original Talbot image of the mask (t_A) at 2nd Talbot plane is shown in Figure 4.2(b) which is calculated using equation 4-1. The simulated hybrid image is shown in Figure 4.2(c). Figure 4.2 (d) is a zoomed

77

in image of Figure 4.2(c). The contrast v of the calculated hybrid image is more than 0.99 which is enough to ensure the quality of the photoresist profile after development.

This simulation shows that Talbot interference lithography is able to generate a hybrid interference image with its lattice modified by a defined Talbot mask with the sufficient contrast to be used in a lithography step.

4.3   EXPERIMENT OF TIL USING 46.9NM TABLE-TOP EUV LASER

To prove the simulation, a TIL experiment based on a capillary discharge EUV laser is implemented. This light source which emits a highly spatially and temporal coherent beam at $\lambda = 46.9$nm has been discussed in Chapter II.

The experiment setup based on Lloyd's mirror is shown in Figure 4.3. Figure 4.3 (a) is the schematic diagram and Figure 4.3 (b) is a photograph of the actual experiment setup. The mask used in this experiment is a TEM grid commercially available[3]. This free-standing Nickle grid has square openings arranged in square lattice. The opening size is $7.5 \times 7.5 \mu m^2$ and the period is $12.5 \times 12.5 \mu m^2$. As the thickness of Nickle is more than 200μm which has near 0 transmission for the illumination with λ=46.9nm, the TEM grid can be treated as binary mask for this EUV lithography experiment.
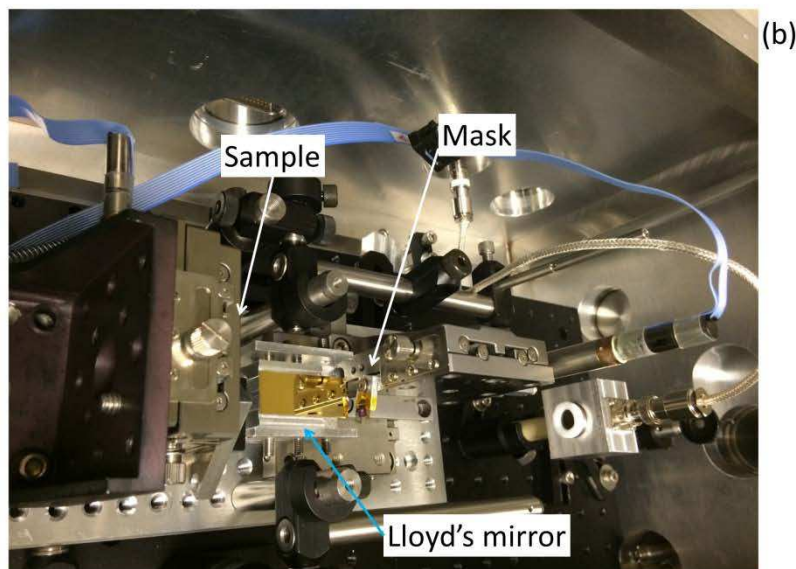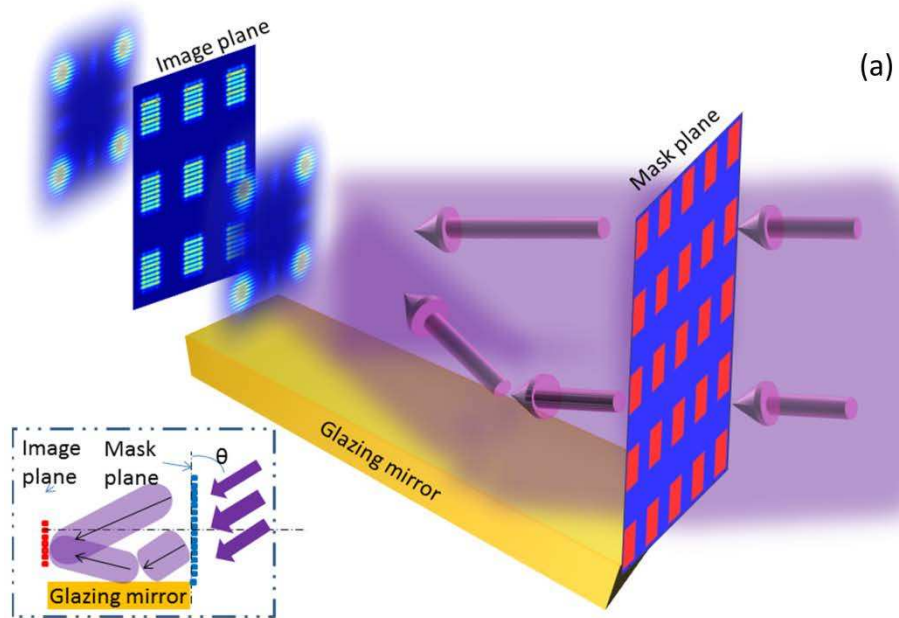
Figure 4.31: Experiment setup for TIL

The two beams illumination is achieved using a Lloyd's mirror configuration schematically shown in the inset in Figure 4.3. After the mask, a flat silicon mirror coated with 100nm gold thin layer is aligned at a 4° incidence angle relative to the incoming beam. The reflectivity of 46.9nm light at this incidence angle is around 0.8[4]. The EUV beam which has been diffracted by the TEM grid is then split by the mirror into two mutually coherent wavefront.

The reflectivity of the Lloyd's mirror determines the contrast of the interference pattern: v. The contrast for this setup is $v = \frac{2\sqrt{I_1 I_2}}{I_1 + I_2} = 0.99$, where I_1 and I_2 are the primary and reflected beams intensities.

Giving the pitch of binary mask equals 12.5µm, the Talbot distance is 6663.2 µm. A Si wafer spin-coated with HSQ was placed at the 5th Talbot plane (z=33316 µm). In this location, two Talbot images produced by the two coherent beams are superposed together. The sample is place in the sample holder which is attached to a XYZ translation stage that displaces the sample in the plane parallel to the mask and adjusts the mask-wafer gap according to the Talbot distance calculated. It is actuated by stepper motors with 1µm accuracy from Thorlabs Inc. (Z812). The sample was exposed with 12 shots of the EUV laser that approximately provides an exposure dose of 21.1mJ/cm² in the sample.

The experimental results are shown in Figure 4.4. The optical microscope image of the Talbot mask is shown in Figure 4.4(a). The scale bar is 10µm. The Talbot interference pattern printed in the photoresist is shown in Figure 4.4(b) which is zoomed in Figure 4.4(c). Both 4.4(b) and 4.4(c) are SEM images showing the lattice generated by the Talbot image superimposed with fringes generated by the interference. This hybrid image proved our previous calculation and simulation. The pitch of the interference fringes inside the cell defined by the Talbot mask is 340nm which is consistent with the angle of incidence of Lloyd's mirror and the wavelength of the illumination used. The pitch of an interference fringes created from a Lloyd's mirror is $p=0.5\lambda/\sin(\theta)$. In this case p=336nm given θ=4° and λ=46.9nm.

Figure 4.4 (d) is a plot of the cross section of one cell in the direction perpendicular to the interference fringes (in dashed blue) superimposed with the expected print in the photoresist (in

solid red) calculated using Eq. 4-2. The simulation adopted the parameters used in the experiment to make a comparison between experimental and theoretical results. An optimized sigmoid function was applied to the calculated Talbot interference image to predict the photoresist response. The theory of Talbot interference lithography is proved by this satisfactory agreement between the simulation and the experimental results.
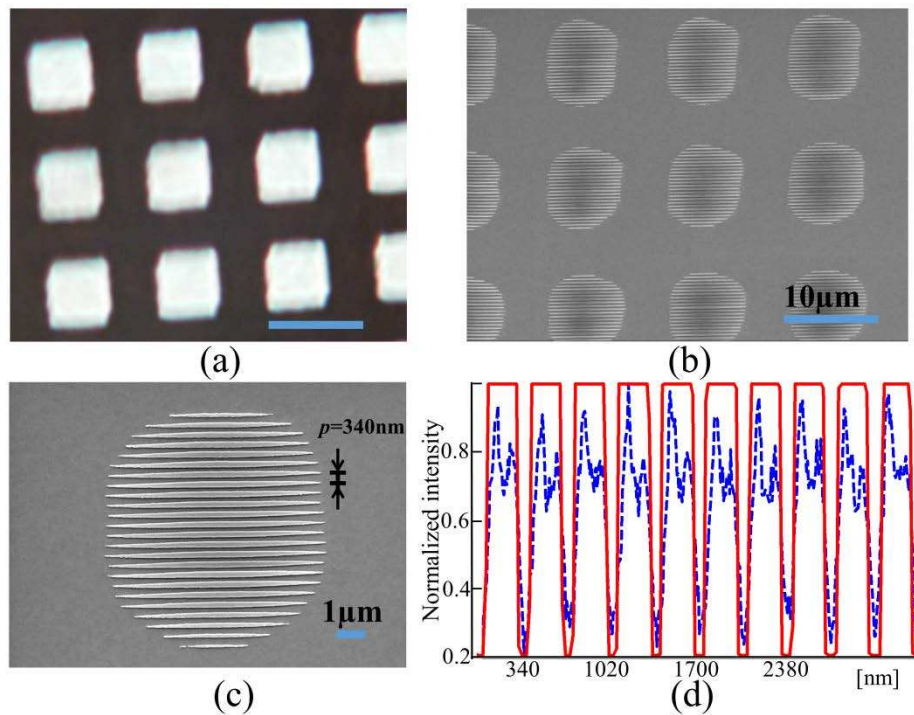
Figure 4.32 : Experiment results of TIL. (a) is the optical microscope image of the Talbot mask, the scale bar is 10μm; (b) (c) are the SEM images for TIL results, (c) is the zoomed in version of (b); (d) is the cross-section of (c) and the prediction of simulation results, blue dash line is the experiment result and red solid line is the simulation result

4.4 ANALYSIS OF THE ADVANTAGES OF TIL OVER TALBOT LITHOGRAPHY AND INTERFERENCE LITHOGRAPHY

The advantages of this hybrid imaging technique reside in the combination of unique characteristic from both imaging methods. The CD in the nanopatterns printed by TIL is no

longer determined by the Talbot mask, but depends on the wavelength of illumination as occurs in IL. As has been discussed in Chapter III section 3.2, the pitch resolution for classic Talbot image can be estimated as: $s = \frac{\lambda}{NA} > \lambda$. However, the pitch resolution for interference lithography is $s = \frac{\lambda}{2\sin(\theta)} > 0.5\lambda$ given the optics configuration is based on two beams interference. Clearly, using TIL, the pitch resolution limit has a potential to be pushed to a higher level than Talbot lithography. In addition, the extended DOF inherited from IL facilitates the implementation of the TIL. The DOF for classic Talbot image can be estimated by $= \frac{\lambda}{NA^2}$, while the DOF for TIL is much larger because nanopatterns with high resolution can be printed at lower NA using TIL.

To exemplify the potential of TIL which is able to print nanopatterns with higher resolution and larger DOF compared with traditional Talbot lithography, a simulation experiment was performed to compare the standard Talbot lithography and TIL. The light source utilized are the same with λ=13.9nm[5]. The two techniques are analyzed and compared regarding the capability to print a periodic structure $T(\xi)$ which is composed of an array of squares sections 65×65nm^2, with a periodicity of 100×100nm^2. The size of the whole field is $w=6\times6\mu$m^2. Inside each square, it is filled by 5 stripes of 6.5nm half pitch.

To print $T(\xi)$ using traditional Talbot lithography, the mask is requested to have the same resolution as the original design because Talbot image is a 1:1 replica to the mask. Needless to say, there is a technical difficulty to fabricate a Talbot mask with a pitch s=13nm and enough contrast for 13.9nm illumination. Even though the mask can be successfully fabricated, to print the 6.5nm half pitch lines onto the wafer with traditional Talbot lithography, the NA needs to be high enough to achieve such resolution. According to the simulation as shown in Figure 4.5, such

nanopatterns can be achieved at the 2nd Talbot plane using Talbot lithography. Figure 4.5 (e) is the Talbot mask with a transmission defined by $T(\xi)$. The resolution of Talbot image is degrading with larger mask-wafer gap as shown from Figure 4.5 (a) to (d) which represents the Talbot images at different Talbot planes ($z=1.5Z_t$, $2Z_t$, $2.5Z_t$, $3Z_t$ respectively).

Even though it fulfills the requirement for resolution, at 2nd Talbot plane, assuming an illumination with a 13.9nm laser and a mask size $w=6\times6\mu m^2$ yields a Talbot distance of $Z_t=1439$ nm with a DOF of 27 nm[1] which is too small for a lithography system requiring an extreme control of the mask-wafer gap. Note that such resolution can also be achieved at 1st Talbot plane as well, but the DOF is even smaller (DOF=17nm at 1st Talbot plane).
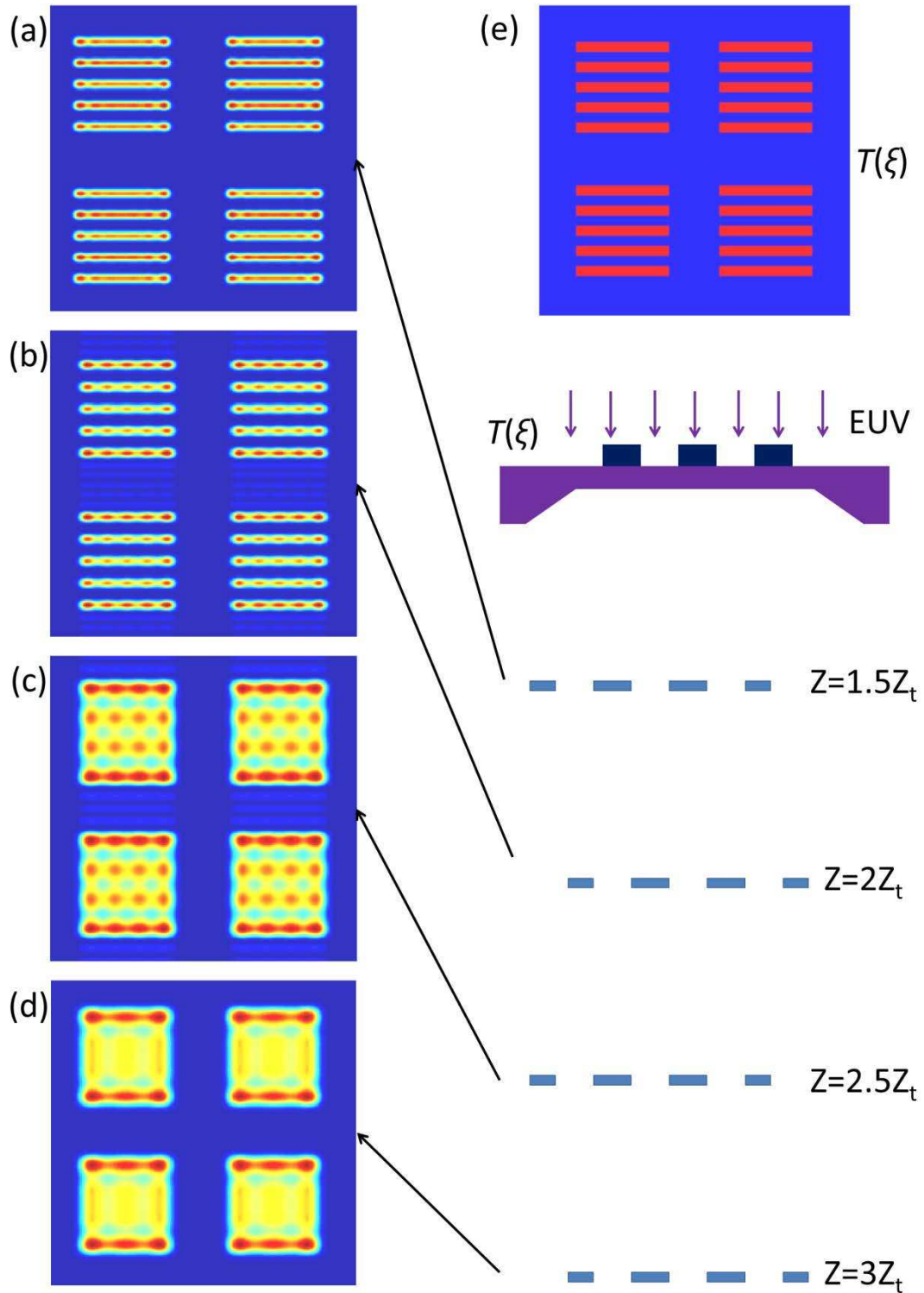
Figure 4.33: Different resolution at different Talbot planes. (a)-(d) are Talbot images of (e) at different Talbot planes.

(a)-(d) have mask-wafer gap as z=1.5Z_t, 2Z_t, 2.5Z_t, 3Z_t accordingly.

However, to print $T(\xi)$ using TIL, satisfactory results can be obtained by much more relaxed parameters. Using TIL, the Talbot mask (defined by $T'(\xi)$) needed to create patterns for $T(\xi)$ is just an array of square holes 65×65 nm^2 with 100×100 nm^2 pitch. The size of $T'(\xi)$ is $w=6 \times 6$ μm^2 as well. The 6.5nm half pitch gratings inside the squares are obtained by the interference of two Talbot images and this resolution is not limited by the NA. The DOF can be enlarged choosing a higher order Talbot plane (N) as shown in Figure 4.6. Simulation results of TIL are shown in Figure 4.6 (a) to (d) which have different mask-wafer gaps as indicated in the figure. Two coherent EUV beams ($\lambda=13.9$nm) with incidence angle $\theta=\pm32.32°$ impinged on the mask shown in Figure 4.6(e), generating two identical Talbot images which are superposed at different Talbot planes creating Talbot interference image.

In the same way as Talbot lithography, the resolution of TIL is also degrading with larger mask-wafer gaps as shown from Figure 4.6 (a) to (d) which represents the Talbot interference images at different Talbot planes ($Z=5Z_t$, $5.5Z_t$, $6Z_t$, $6.5Z_t$ respectively). However, satisfactory results can still be printed at higher order Talbot planes (N=6) compared with the requirements of TL shown in Figure 4.5 (N=2).
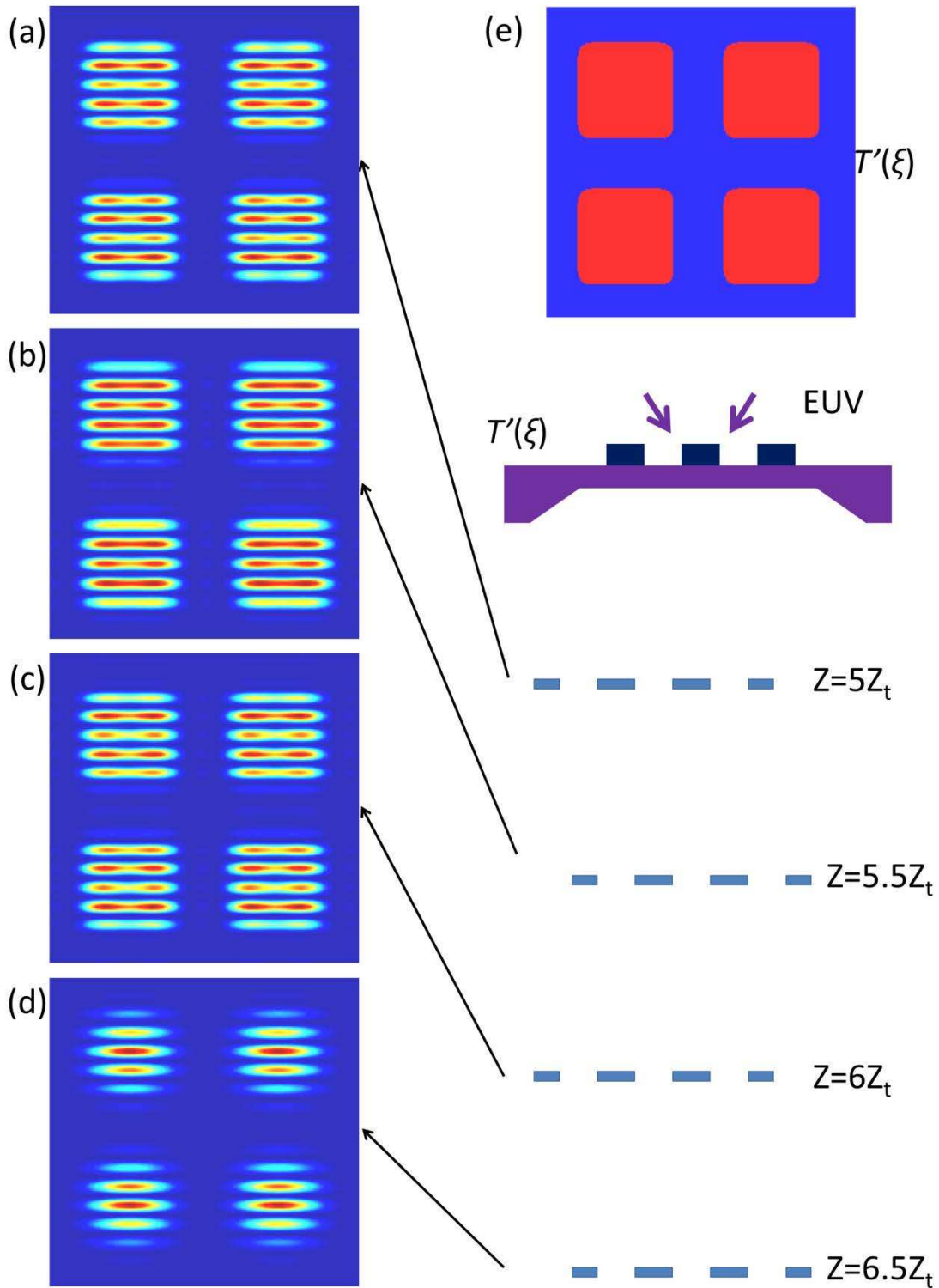
Figure 4.34: Simulation of TIL to print $T(\xi)$. (e) is the mask for TIL simulation, the transmission is represented as $T'(\xi)$; (a)-(d) are Talbot interference images of (e) at different Talbot planes. (a)-(d) have mask-wafer gap as $z=5Z_t$, $5.5Z_t$, $6Z_t$, $6.5Z_t$ accordingly.

86

The resolution of TIL is limited by the interference part ($s = \frac{\lambda}{2\sin(\theta)}$) but the DOF of TIL is limited by the Talbot imaging component. Mathematically as has been discussed in section 3.2, the depth of focus can be defined as $DOF = \frac{\lambda}{NA^2}$ for Talbot lithography. $NA = \sin(\alpha)$ where $\alpha = \tan^{-1}(\frac{0.5 \times w}{2Np^2/\lambda})$. w is the size of the mask, N is the order of Talbot plane, p is the period of the patterns on the mask and λ is the wavelength of illumination. A comparison is made between Figure 4.5(b) (2nd Talbot plane for Talbot lithography) with Figure 4.6 (c) (6th Talbot plane for TIL), both of which have enough contrast and resolution for 6.5nm half pitch grating. With the same resolution, DOF for TIL is 135nm, which is 5 times as the DOF for traditional Talbot lithography (27nm).

A calculation of this alternative design confirms the advantages of the Talbot interference lithography: higher resolution with larger DOF using a mask with relaxed fabrication requirements.

4.5   CONCLUSION

A hybrid lithography technique that combines Talbot lithography and interference lithography was analyzed in this Chapter. In a single lithography step, TIL is able to print custom defined periodic patterns which neither the Talbot nor interference lithography techniques can accomplish by itself. It inherits the resolution limit from IL together with the flexibility of lattice design from Talbot imaging. The arbitrary shaped cells produced by the Talbot image can be filled with fine interference patterns (lines or dots) generated by interference of two or more coherent wavefronts. In addition, TIL relaxes the constrain in the mask fabrication and simultaneously expands the DOF by reprinting nanopatterns in higher resolution with lower NA.

REFERENCE:

[1]   W. Li and M. C. Marconi, "Extreme ultraviolet Talbot interference lithography," *Opt. Express*, vol. 23, no. 20, p. 25532, 2015.

[2]   J. W. Goodman, *Introduction to Fourier Optics*. Roberts & company publisher, 2005.

[3]   https://www.tedpella.com/grids_html/Pelco-TEM-Grids.htm.

[4]   http://www.rxollc.com/idl/.

[5]   B. A Reagan, K. A Wernsing, A. H. Curtis, F. J. Furch, B. M. Luther, D. Patel, C. S. Menoni, and J. J. Rocca, "Demonstration of a 100 Hz repetition rate gain-saturated diode-pumped table-top soft x-ray laser.," *Opt. Lett.*, vol. 37, no. 17, pp. 3624–3626, 2012.

APPENDIX I: MATLAB CODE FOR TALBOT LITHOGRAPHY AND TALBOT

INTERFERENCE LITHOGRAPHY

```matlab
%%%%%%%%%%%%%%%%%%%%%%%
%This Matlab script is used to simulate the Talbot images described in this
%thesis
%%%%%%%%%%%%%%%%%%%%%%%
function Fig4-5

tic
dx=1e-9;%pixel size
dy=dx;%pixel size
NN=6000;
CellSize=100e-9;
PitchLineSpace=13e-9;
Ncell=round(CellSize/dy); %%% how many pixels of one cell
NLine=round(PitchLineSpace/2/dx);%%%% number of pixels for 1 row of line
Nl=5; % number of lines in one cell
%%%%%%%%%%%%%%%%%%%%%%%%%%%%%%%%%%%%%%%%%%%%%%%%%%%%%%%%%%%%%%%%%%%%%

    Ai=zeros(NN,NN);              %   Ai=;

    Line=ones(NLine,round(.65*Ncell));
    Space=zeros(NLine,round(.65*Ncell));

    FirstPeriod=[Line;Space];
    [NPx,NPy]=size(FirstPeriod); %%%
    Cell=zeros(Ncell,Ncell);
    Cell(1:NPx*Nl,1:NPy)=repmat(FirstPeriod,Nl,1);

    Ai=repmat(Cell,round(NN/Ncell),round(NN/Ncell));

    figure(1)
    imagesc(abs(Ai(1:round(.1*NN),1:round(.1*NN))));
    axis square
%%%%%%%%%%%%%%%%%%%%%%%%%%%%%%%%%%%%%%%%%%%%%%%%%%%%%%%%%%%%%%%%%%%%%

[Nx,Ny]=size(Ai);

lambda=13.9e-9;

Field=Nx*dx;

p=CellSize;                               %%%% cell period    in m

z=2*(p)^2/lambda;                         %%%%%%%%%%%%%%%%%% dx*80is the period and
z=zT
zt=z                                      %%%%%%%%%%%%%%%%%% try different
z_t
d=3.*z%% 3rd talbot plane
NA=sin(atan(Field/(2*d)))
res=0.61*lambda/NA
```

89

```matlab
DOF=lambda/(NA^2)


norm=1/sqrt(Nx*Ny);
[k,l] = meshgrid(-(Nx-1)/2:1:(Nx-1)/2, -(Ny-1)/2:1:(Ny-1)/2);
kernel=exp(-1i*pi*(k.^2*dx^2+l.^2*dy^2)./(lambda*d));          %%%%%%%%%%%
Propagator


%kernelR=exp(1i*pi*(k.^2*dx^2+l.^2*dy^2)./(lambda*d));          %%%%%%%%%%
reverse propagator


OUTi=norm*fftshift(ifft2(fft2(Ai).*fft2(kernel)));                 %%%%%%%
convolution of Ai and propagator is the Fresnel diffraction


Temp=abs((OUTi.^2));
figure(2);
imagesc(Temp);
axis square
%
% figure(3)
% plot(Temp(2495:2515,2308))
% hold on
%
%
% Temp1=Temp(2495:2515,2308);
% plot(2:1+length(Temp1),Temp1)
% for i=1:length(Temp1)-1
%      Temp1(i)=Temp1(i)+Temp1(i+1);
% end
% plot(2:1+length(Temp1),Temp1)
% plot(0.95.*194.*ones(1,length(Temp1)))
% plot(0.9.*97.*ones(1,length(Temp1)))
%
%
% hold off
toc
```

```
%%%%%%%%%%%%%%%%%%%%%%
%This Matlab script is used to simulate the Talbot interference images
described in this %thesis
%%%%%%%%%%%%%%%%%%%%%%
function TalbotInterence2PlaneWavesFig5

%%%% this parameter worked only for DEG=5
%lambda=46.9e-9;
lambda=13.9e-9;
Scale=2*pi/lambda;

alphaDEG=32.32;
%delta_d=1e-6;
alpha=alphaDEG/180*pi;
theta=alpha;

k1y=-1*sin(theta)*Scale;
k1x=0;
k1z=-1*cos(theta)*Scale;

k2y=sin(theta)*Scale;
k2x=0;
k2z=-1*cos(theta)*Scale;

% %%%%% no polarization
e12=1;
e13=1;
e23=1;
% %%%%%

Nx=6000;
Ny=6000;

Pixel=1e-9;%%% pixel size
%PP=10e-6;
PP=100e-9;   %%% in real period size
Period=round(PP/Pixel);
%A=MaskTalbotSquare(Nx,Period);
A=MaskTalbotSquareCham(Nx,Period);
[Nx,Ny]=size(A);
[x,y] = meshgrid(-(Nx-1)/2:1:(Nx-1)/2, -(Ny-1)/2:1:(Ny-1)/2);

zt=2*PP^2/lambda;%% half talbot distance
%z=2*zt
%z=130e-6;
z=7*zt; %3rd talbot plane
%propagate A to working distance %%OUTi=TalbotProp(Ai,pixelSize,d,lambda)
A1=TalbotProp(A,Pixel,z,lambda);

%%%% this x need to be defined as the x axis of the mask plane
I0=0.5.*(A1.^2+A1.^2);
I=I0+e12.*A1.*A1.*cos((k2x-k1x).*(x.*Pixel)+(k2y-k1y).*y.*Pixel+(k2z-
k1z).*z.*Pixel);
I=abs(I)./max(max(abs(I)));
figure(3)
```

```matlab
imagesc(abs(I));
axis square


%%%%
%This function is the Fresnel propagator
%%%%
function OUTi=TalbotProp(Ai,pixelSize,d,lambda)
tic
%%%%%%%%%%%%%%%%%%%%%%%%%%%%%%%%%%%%%%%%%%%%%%%%%%%%%%%%%%%%%%%%%%%%%%
dx=pixelSize;%pixel size
dy=pixelSize;%pixel size
%%%%d is the image distance
%%%%%%%%%%%%%%%%%%%%%%%%%%%%%%%%%%%%%%%%%%%%%%%%%%%%%%%%%%%%%%%%%%%%%%%%


[Nx,Ny]=size(Ai);


%lambda=46.9e-9;                          %%% wavelength


Field=Nx*dx
M=Nx;
% z=2*(dx*pp)^2/lambda                     %%%%%%%%%%%%%%%%% z=zT
NA=sin(atan(Field/(2*d)))
res=0.61*lambda/NA
DOF=lambda/(NA^2)


norm=exp(1i*2*pi/lambda*d)/(1i*lambda*d);
[k,l] = meshgrid(-(Nx-1)/2:1:(Nx-1)/2, -(Ny-1)/2:1:(Ny-1)/2);
kernel=exp(-1i*pi*(k.^2*dx^2+l.^2*dy^2)./(lambda*d));        %%%%%%%%%%
Propagator


OUTi=norm*fftshift(ifft2(fft2(Ai).*fft2(kernel)));               %%%%%%
convolution of Ai and propagator is the Fresnel diffraction
% OUTi=OUTi.^2;
% OUTi=OUTi./(max(max(OUTi)));


figure(2);
imagesc(abs((OUTi(round(0.15*M):round(0.85*M),round(0.15*M):round(0.85*M)))))
; %%%% has .^2 already
%imagesc(abs(OUTi.^2));%%%%
colorbar('location','EastOutside')
axis square
%saveas(gcf,strcat('numFile=',num2str(numFile),'.pdf'))


toc
```

APPENDIX II: DETAILED MASK FABRICATION RECIPE AND EBL EXPERIMENT

TO DETERMINE ELECTRON DOSE

Mask fabrication recipe:

This recipe is to fabricate silicon membrane supported EUV mask. The thickness of the membrane was 100nm. Note that different thickness of silicon may lead to different dose because of the backscattering.

1. Spin coat HSQ on silicon membrane at 4000rpm for 90 seconds;
2. Expose the membrane IMMEDIATELY after spin-coating with optimized dose around $3000\mu C/cm^2$;
3. Develop the exposed membrane in NaOH/NaCl = 1%/4% wt% for 4mins. The solution is DI water. Right after the development, IMMEDIATELY RINSE the membrane with FLOWING DI water for 90 seconds;
4. Blow dries the developed membrane with UHP nitrogen from the side of the membrane, NEVER blow the nitrogen normal to the membrane.

For free-standing EUV mask based on 50nm silicon nitride membrane, a positive resist ZEP520 is used and the recipe is as following:

EBL part:

1. Spin coat HDMS on silicon membrane at 3000 rpm for 30 seconds;
2. Spin coat ZEP520a (1:1 dilution rate) on silicon membrane at 6000 rpm for 30 seconds, rendering a 300nm resist film;
3. Prebake the membrane at 180°C for 3 minutes;
4. Expose the membrane with optimized dose (around $300\mu C/cm^2$);
5. Develop the exposed membrane in Xylene for 90 seconds and soak in IPA afterwards for 90s;

RIE part:

1. Clean the RIE chamber using O2 plasma for 5 minutes: Pressure set 100mTorr, CF4 flow at 5 SCCM, O2 flow at 50 SCCM, RIE power 250W, Process time 300s;

2. Nitride etching: Pressure set 50mTorr, CF4 flow at 40 SCCM, O2 flow at 10 SCCM, RIE power 150W, Process time 50s;

Dose optimization is based on a "dose map" designed for certain pattern to eliminate the backscattering effect. Different resist has an estimated dose like HSQ is $3000\mu C/cm^2$ but ZEP520a is $300\mu C/cm^2$. Patterns with different size need to change this dose accordingly. For example, the original design for metasurfaces (square pillars with pitch=$410\times410nm^2$) is $500\times500\mu m^2$. A field with $50\times50\mu m^2$ size needs to be tested to save time yet still represent all the backscattering response from neighboring exposure. We exposed this field with same design but different size with 16 different doses and the results looks like following.

Design A   **Design B**   **Design C**

2000μC/cm²

2100μC/cm²

2200μC/cm²

2300μC/cm²
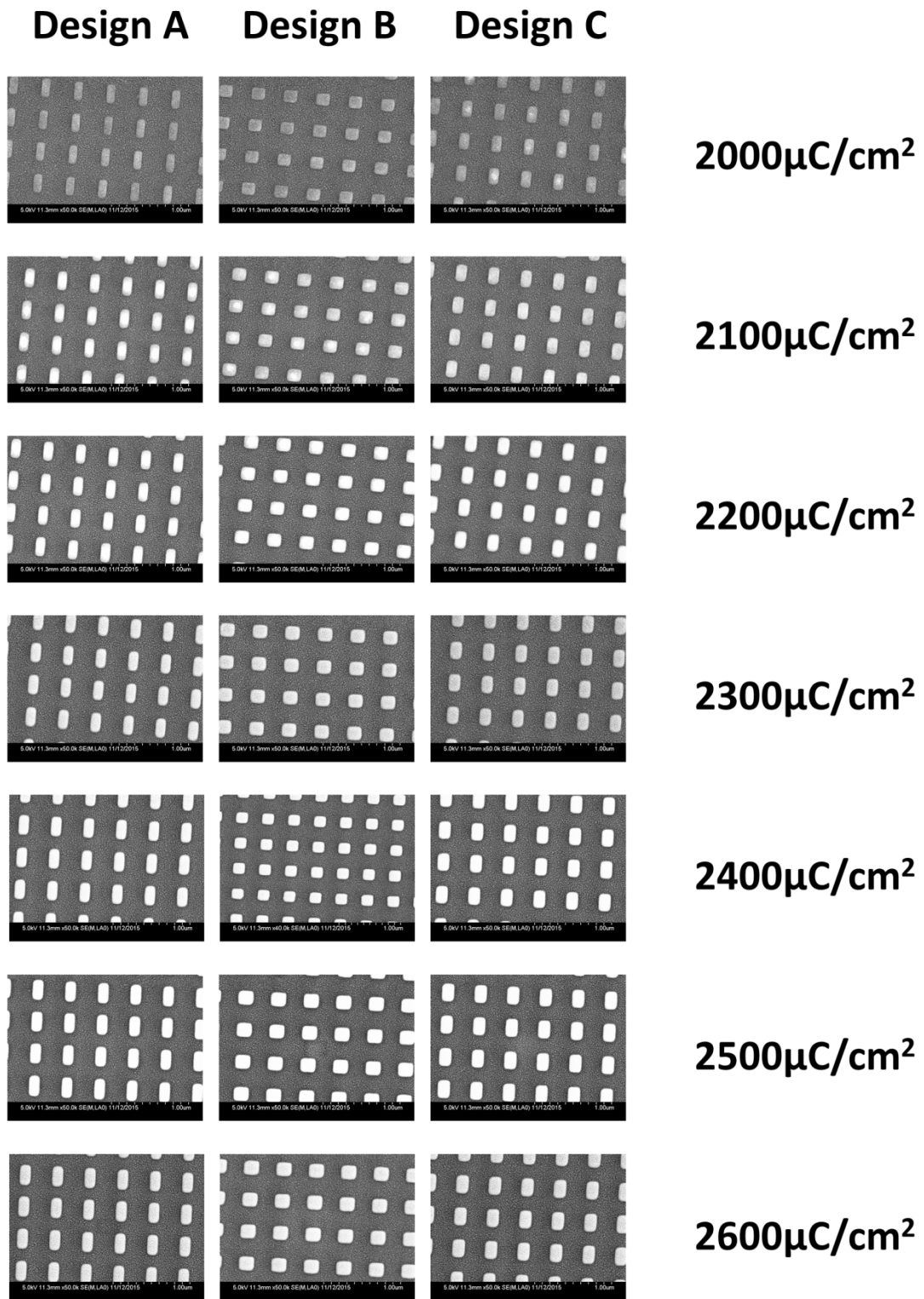
2400μC/cm²

2500μC/cm²

2600μC/cm²

Fig. 1: Dose map

Basically, we test the dose around the estimation until satisfactory resolution is achieved. A robust process will have a large dose process window without which the fabrication wouldn't be reliable. Once the optimized dose is set, in this case 2400µC/cm^2, it is used to expose multiple original designs.

APPENDIX III: OPERATION LIST FOR CAIBE

CAIBE system needs to be run in high vacuum. Before the argon flows into the system, it needs to be pumped down to low 10^{-6} Torr. When 6 SCCM Argon is being injected to the system, the pump requires a pumping speed large enough to maintain the system under 10^{-4} Torr. After the system has been pumped down to 10^{-6}, the argon supply line needs to be purged by 3 SCCM argon flows which are controlled accurately by a mass flow controller for at least 0.5 hour. With a comparative pure Argon circumstance, an increasing current is applied to the heater around the hollow cathode tip where argon flows through at 2.5 SCCM. After the heater current is enhanced to 7.25A for less than 2 minutes, a discharge should be built. If not, the Argon flow rate should be enhanced up to 6 SCCM until a discharge is well built. The heater current then should drop automatically to 3.75A. However, in different conditions, heater current will vary from 3.75A to 4.5A or even higher. In this case, Argon flow should be changed accordingly so that the heater current is stable. This is very important to enhance stability of the ions and the life-time of the hollow cathode. To decrease the amount of oxygen inside the system when the cathode tip is heated, samples are loaded at least 15 minutes before the power supply is turned on. In addition, the load-lock gate is opened 15 minute after the heater is cooled by Argon flow. The power supply has a build-in memory in which the program '0' stored the optimized voltage & current set-up for Ar plasma. When the discharge is built, the discharge voltage will decrease to around 60 to 70 Volts and the discharge current should be around the set up value 0.28A. After few minutes, the plasma will be steady inside the discharge chamber. Once the accelerating voltage is applied by pressing 'start the beam', the ion beam will be extracted to the etching chamber and etching process is initiated.

The samples are clamped to the holder mounted onto the transmission rod which is located on the low vacuum side of the system. With a closed gate-valve, the load-lock chamber is pumped down to 50 mTorr by a sorption pump. Then the gate valve can be opened and the sample is inserted to the temperature control unit which also has two spring screws to lock the holder tightly. The holder can then be released from the transmission rod by rotating 90 degree. The gate-valve should be closed after the transmission rod is moved back to the load-lock chamber. Before the sample is etched by the Ar plasma, a shelter blocks the ion beam for 15 seconds to stabilize the ion beam. The operation flow can be concluded as following:

1. Pump the main vacuum to 10^{-6} Torr;

   Make sure the Nitrogen tank (black cylinder) is not empty. Open its main valve, do not touch regulator (it has to be larger than 80 psi).

   Open the gate valve for pumping line by switching the switch;

   Plug in cable of mechanical pump then open its valve slowly;

   Check the vacuum of high vacuum chamber which should be <50 micron (around 25mins);

   Open the turbo pump by pressing start.

2. Purge the Argon gas line with 3 SCCM flow for 30mins. (There is a controller underneath the power supply box. During this time the vacuum should be under 10^{-4}); Make sure the valve for Ar is open.

3. Clamp the sample to the copper holder and mount them together to transmission rod;

   The transmission rod is not straight, meaning there is only one angle that it can be inserted. There is a value on the rod, to insert; it should be around 180 deg. To retract it should be around 270 deg

4. Pump the load-lock chamber to 50 Microns using the sorption pump; (With sample on holder inside the low VAC chamber)

   Liquid nitrogen is needed to soak the pump. Refill once after 5 mins. Open the valve to pump and close the valve before next step.

5. Open the gat-valve all the way;

6. Insert the transmission rod gently to the main chamber and lock it to the temperature control unit;

   The load lock system is not state of art. EXTREME caution is needed to insert the holder, if you force it too much. It will break and you will need to re-open the whole system to fix it. So, be as patient as you can.

7. Release the transmission rod and move it back to the load-lock chamber;

   Rotate 180 deg to around 90 deg, just try to find a proper angle to move it back.

8. Shut down the gate valve and leave the main chamber pumping for 10 more minutes to eliminate the oxygen introduced from the load-lock chamber;

9. Set the Argon flow controller at 5 SCCM for 15mins and then open the power supply by recalling program '0' (Recall->0->'enter'->'source');

10. Wait the heater current going up to 7.25A and 2 minutes later the discharge should be built;

11. If not, increase the argon flow until the discharge is built but the argon flow should not exceed 6 SCCM;

12. After the heater current decreasing to 3.75A and discharge voltage and current being stable, start the cryo cooling by open the Helium which is circulating around the liquid nitrogen tank. Start the beam with the shelter blocking it after the temperature is at -100°C. (Press the beam button to start beam)

13. After the beam is warmed up and stable (usually 15 seconds), open the shelter and start the etching process. Plug in the control box for moving the shutter backwards, unplug it and use hand to move it back.

14. When the etching is down, close the beam then close the source. Wait for 15 mins with Ar flow on. Close the shutter by unplug the control box and move the shutter by hand on the back side of the system. Close the helium flow.

15. Open the gate valve and re-insert the transmission rod at around 270deg.

    It is highly likely that you will have trouble inserting it back. Again, rotate the rod around there and try to be patient.

16. Once you insert the rod, rotate 90 to 180deg and pull the sample holder back gently. If it does stuck there, try different angle. DON'T FORCE IT

17. Close the gate valve for low vac chamber and then grab your sample holder in low vac chamber.

18. Close the gate valve for pump line. Close the turbo. Close valve of mechanical pump. Unplug the cable for mechanical pump.

19. Wait until the analog sensor on touch screen is 9.999 and then close the Ar flow.

Close the Nitrogen tank.